Acoustical Measurement of Velocity, Vorticity and Turbulence in the Arctic Boundary Layer Beneath Ice

by

Dimitris Menemenlis
B.Eng., McGill University, 1985
M.A.Sc., University of Waterloo, 1987

A Dissertation Submitted in Partial Fulfillment of the
Requirements for the Degree of

DOCTOR OF PHILOSOPHY

in the Department of Electrical and Computer Engineering

We accept this thesis as conforming
to the required standard

.....
Dr. D.M. Farmer, Supervisor (Electrical and Computer Engineering)

.....
Dr. R.L. Kirlin, Co-Supervisor (Electrical and Computer Engineering)

.....
Dr. A. Antoniou, Departmental Member (Electrical and Computer Engineering)

.....
Dr. R.W. Stewart, Outside Member (Physics and Astronomy)

.....
Dr. R.M. Clements, Outside Member (Physics and Astronomy)

.....
Dr. M.G. McPhee, External Examiner (McPhee Research Company)

University of Victoria

Supervisors: Dr. D.M. Farmer and Dr. R.L. Kirlin

Abstract

The concept of reciprocal acoustical travel-time measurements as a means of determining path-averaged currents is well established. We have designed an instrument to exploit this principle in studies of the boundary layer just beneath the arctic ice cover. Such measurements are of interest both because of the opportunity provided for comparison with the more commonly acquired point measurements and because of a particular configuration allowing determination of average vorticity, which cannot be achieved with the traditional approach; in addition, their unprecedented sensitivity allows detection of phenomena not observable with traditional sensors.

The acoustical instrument was deployed during the spring of 1989 in the sub-ice boundary layer of the Eastern Arctic in order to measure turbulence, path-averaged horizontal current, and relative vorticity. A triangular acoustic array of side 200 m was used to obtain reciprocal transmission measurements at 132 kHz, at 8, 10 and 20 m beneath an ice floe. Pseudo-random coding and real-time signal processing provided precise acoustic travel time and amplitude for each reciprocal path.

Mean current along each acoustic path is proportional to travel time difference between reciprocal transmissions. Horizontal velocity normal to the acoustic paths is measured using scintillation drift. The instrument measures horizontal circulation and average vorticity relative to the ice, at length scales characteristic of high frequency internal waves in the region. The rms noise level of the measurements is less than 0.1 mm/s for velocity measurements and 0.01 f for vorticity, averaged over one minute. Except near the mechanical resonance frequency of the moorings, the measurement accuracy is limited by multipath interference.

Path-averaged horizontal velocity is compared to point measurements and marked differences are observed due to local anomalies of the flow field. The integral measurement of current is particularly sensitive to the passage of internal waves that have wavelengths longer than the horizontal separation of the transducers. A comparison

of horizontal velocity at two depths in the boundary layer shows good coherence at internal wave frequencies and some attenuation as the ice is approached. Relative vorticity at internal wave length scales is dominated by horizontal shear caused by flow interaction with ice topography and not by planetary vorticity.

Reciprocal acoustical travel time measurements over paths of several hundred meters can be used to probe the statistical behaviour of turbulent velocity fine structure in the ocean. For homogenous isotropic flows, and for long measuring baselines, an analytic expression relating line-averaged and point measurements of velocity is derived. Anisotropic and inhomogeneous flows are also considered. Correction formulas for the spatial and temporal variability of advection velocity along the measuring baseline are obtained. Practical limitations are established, and experimental data from the arctic boundary layer beneath ice is compared with the theory. A new remote sensing technique for measuring turbulent kinetic energy dissipation rate is suggested.

Examiners:

.....

Dr. D.M. Farmer, Supervisor (Electrical and Computer Engineering)

.....

Dr. R.L. Kiglin, Co-Supervisor (Electrical and Computer Engineering)

.....

Dr. A. Antoniou, Departmental Member (Electrical and Computer Engineering)

.....

Dr. R.W. Stewart, Outside Member (Physics and Astronomy)

.....

Dr. R.M. Clements, Outside Member (Physics and Astronomy)

.....

Dr. M.G. McPhee, External Examiner (McPhee Research Company)

Contents

List of Tables

List of Figures

Acknowledgments

I thank Dr. David Farmer for the opportunity to work on a challenging and interesting project, and for his guidance, support and encouragement at every stage of my research. I thank Prof. R.W. Stewart for many helpful suggestions and enjoyable discussions. I thank Profs. A. Antoniou, R.M. Clements, L. Kirlin, and A. Zielinski, for serving on my supervisory committee and providing useful feedback.

Thanks are due to Paul Krauetner, P.C. Balla, Ron Teichrob and Jasco Research for developing the electronics; Syd Moorhouse, and Oceanetic Measurements for designing the moorings; Ron Teichrob, Dave Farmer, Mike Welch, Pat McKeown and Tom Lehman for help during deployment and recovery; Peter Czipott, Miles McPhee, Murray Levine, Laurie Padman and Robin Williams for helpful discussions and making their data available. I am grateful to Schlomo Pauker and two anonymous reviewers for their very constructive criticism of the instrumentation paper.

I am grateful to Miles McPhee for formulating the question answered by the reciprocal travel-time analysis paper. I thank Clayton Paulson for pointing out previous atmospheric work on line-averaging, J.C. Kaimal for a useful telephone conversation, R.W. Stewart and Rolf Lueck for constructive criticism, Ann Gargett and Greg Holloway for patiently answering my questions on axisymmetric turbulence.

Last, but not least, I would like to thank all my Ocean Acoustics friends and colleagues for stimulating discussions, copious help and support through the years, and for making life at the Institute of Ocean Sciences interesting and enjoyable. In

particular, I thank Len Zedel for the hikes and dives, Li Ding for many discussions pertaining to bachelor life, Daniela DiIorio and Yunbo Xie for the music, Craig McNeil and Svein Vagle for the pub nights, Mike Dempsey, Vadim Polonichko and Mark Trevorrow for the soccer, Johannes Gemmrich and Alan Adrian for the kayak trips, Craig Elder for the smoked salmon, Rex and Marilee Andrew for south-of-the-border travel advice, Will Sayers for offbeat coffee break conversations, Willi Weichselbaumer for real estate advice, Donald Booth for his outspoken and entertaining views, and Grace Kamitakahara and David King for being the most excellent neighbors.

This work was supported by U.S. Office of Naval Research grant N00014-88-J-1102 and the author was funded by scholarships from the Natural Sciences and Engineering Research Council and the Science Council of B.C.

TO MY PARENTS

"Man wants to know, and
when he ceases to do so,
he is no longer a man."

Fridtjof Nansen
(1861-1930)

Chapter 1

Introduction

As part of the Coordinated Eastern Arctic Experiment (CEAREX), we designed and deployed an acoustical instrument to measure path-averaged horizontal velocity, relative vorticity, and turbulence in the oceanic boundary layer beneath ice. Herein, we discuss the instrumentation and measuring techniques used, and the observations made during the spring of 1989, just beneath a drifting floe, 300 km northwest of the Svalbard Archipelago. A triangular array of acoustic transducers, 200 m on a side was deployed and precise acoustic amplitude and travel time data was collected within the first 20 m of the sea surface. Reciprocal acoustical travel time measurements and scintillation analysis were used to resolve path-averaged horizontal currents, the vertical component of vorticity relative to the ice, and spectral properties of the turbulent fine structure. Such measurements are of interest both because of the opportunity provided for comparison with the more commonly acquired point measurements, and because the array configuration permits the determination of average vorticity, which cannot be achieved with the traditional approach; in addition, their unprecedented sensitivity allows detection of phenomena not observable with traditional sensors. We relate our observations to fundamental boundary layer physics and wave dynamics.

1.1 Motivation

Oceanographic research using underwater acoustic systems, makes exacting demands on signal processing and storage technologies. This past decade has witnessed the advent of powerful and affordable digital signal processing microprocessors and the development of high-quality digital audio recording equipment. These technological breakthroughs are fascinating on their own merit; however, what is even more exciting is the possibility of using them to deepen our understanding of the physical world. To achieve this, the gap between engineering and the physical sciences must be bridged. We have used the above-mentioned tools to make path-averaged acoustical measurements in the boundary layer beneath the arctic pack ice. The motivation for these measurements is given below.

Large sections of the Arctic Ocean are covered either permanently or seasonally by sheets of floating ice. Sea-ice acts as a bridge between the atmosphere and the ocean and its presence influences many important environmental interactions such as momentum transfer, heat flux, absorption of radiant energy and biological production. The extent of the ice coverage is sensitive to climatic variations; at the same time it has a global impact on climate and the circulation of the oceans and the atmosphere. Sea-ice participates in a variety of feedback processes. As a positive feedback system, ice reflects short-wave solar radiation, cooling the surface and contributing to an expansion of the ice cover. As a negative feedback system, the cold surface builds a temperature inversion in the atmospheric boundary layer, directing more sensible heat towards the surface, and reduces the amount of long-wave radiation emitted by the ice [75].

Increased knowledge of the ice-ocean-atmosphere interfaces will lead to more judicious assumptions in global climatic models. This is a prerequisite for improved long-term climate prediction and for attacking important problems such as the effect of industrially released gases on global warming [50]. On a practical level, the seasonal advance and retreat of the marginal ice zone, restricts navigation through the polar regions and impedes oil and natural gas exploration activity.

An improved capability for predicting ice behaviour and movement contributes to safe navigation and exploration activities in polar regions.

In order to parameterize the interaction between the polar oceans and the atmosphere, it is necessary to study the small-scale processes that occur in a thin layer beneath the ice. The study of this turbulent boundary layer is complicated by the presence of large irregularities in the underside of the ice. Measurements in this layer have traditionally been carried out using instrumented clusters that record temperature, conductivity and three orthogonal components of current velocity [43], or with high-resolution vertical profilers. The drawback of these methods is that they are essentially local in character and may not reflect the average properties of the boundary layer. It is desirable to obtain path-averaged measurements of the boundary layer properties. Integral measurements can complement local observations and check their representativeness; they provide a natural bridge between individual profiling data, and the more general problem of parameterizing boundary layer properties faced by numerical modellers. The essence of our experiment is the comparison of the horizontally integrated boundary layer structure with detailed vertical profiles.

1.2 Current Measurements

The current measuring technologies typically used beneath sea-ice are described by Morison [51] and McPhee [43]. Moored and profiling mechanical current meters have been successfully used to measure turbulence and internal waves. Electromagnetic current meters, diode-laser-Doppler velocimeters and more recently acoustic Doppler current profilers have also been used. A common feature of all these measuring technologies is that they are inherently local in character. Because of irregularities in the underside of the ice, point measurements in the boundary layer are subject to local anomalies and fine structure and may not be representative of the mean flow field. Integral measurements of current provide a means of checking the validity of local observations.

The concept of reciprocal acoustical travel time measurements as a means of determining path-averaged currents is well established [83]. Small-scale acoustical current meters, based on reciprocal travel time measurements over a few centimeters, have been used to estimate the water drag coefficient of first-year ice [69]. Worcester *et al.* [84] extended the technique to the direct measurement of mesoscale ocean currents by using transceiver separations of several hundred kilometers. At those length scales, the problem is complicated by the existence of multiple acoustic paths and the effects of sound speed structure. Our measurements are made in the well-mixed layer adjacent to the floe, where the effects of sound speed variability are negligible. The horizontal separation of the transducers is 200 m and the pulse length allows resolution between the direct and ice-reflected paths for measurements made within a few meters of the lower surface of the ice. However, the shorter range requires travel time measurements that are a few orders of magnitude more precise than those described by Worcester *et al.* Because of its dimensions, the acoustic current meter is particularly sensitive to the passage of high frequency internal waves under the ice camp.

1.3 Scintillation Analysis

Horizontal velocity normal to the acoustic paths can be determined by measuring scintillation drift. Sound traveling through a medium having random fluctuations in refractive index suffers perturbations which cause amplitude and phase scintillations on a receiving plane. These scintillations can be used to study the sound speed fine structure and large scale motions of the intervening fluid [21]. The acoustic array in the Arctic is used to investigate the applicability of the scintillation technique to the study of the ice-water boundary layer.

A significant original contribution presented in this dissertation is the analysis of reciprocal travel-time scintillations in terms of the intervening velocity fine structure. The Arctic provides an ideal laboratory to test the theoretical ideas expounded in Chapter 5. First, the ice is a stable platform from which sensitive

instrumentation can be suspended to probe the oceanic boundary layer. Second, due to negligible sound speed fine structure, the path-averaged measurements of velocity fine structure using reciprocal travel time scintillation analysis can be directly compared to the more traditional forward scatter analysis.

1.4 Relative Vorticity

Müller *et al.* [52] pointed out the importance of the potential vorticity mode of motion which must coexist with internal gravity waves at small scales. Because relative vorticity and horizontal divergence are difficult to measure, the vortical mode of motion has traditionally been ignored. Müller *et al.* [53] used a triangular current meter array to estimate potential vorticity at internal gravity wave length scales in the ocean. They calculated relative vorticity and horizontal divergence, not from a continuous line integral but from measurements at three discrete locations. This causes significant sampling errors. Rossby [67] suggested a better method for measuring relative vorticity. He pointed out that the difference in travel times of acoustic signals traveling in opposite directions around a closed ring of transceivers provides a direct measurement of the enclosed average relative vorticity. Longuet-Higgins [40] showed that a ring of four instruments will determine the scalar vorticity and its horizontal gradient, while a ring of five instruments can also determine the Laplacian of the vorticity field. Winters and Rouseff [82] proposed a filtered backprojection method for the tomographic reconstruction of vorticity in a moving fluid with variable index of refraction. Ko *et al.* [32] demonstrated the feasibility of measuring mesoscale ocean vorticity from acoustic measurements. This thesis reports the use of this technique to measure vorticity at internal gravity wave length scales in the boundary layer just a few meters beneath the arctic ice cover.

1.5 Thesis Outline

Chapter 2 is a review of statistical tools used to describe random fields, of basic boundary layer physics with emphasis on the oceanic boundary layer beneath ice, and of internal wave dynamics. A brief overview of the Coordinated Eastern Arctic Experiment and of the oceanography ice camp is also presented. This is a review chapter and does not contain any original contributions, except for the bathymetric transect of Figure 2.5, which was one of our responsibilities at the oceanography ice camp.

Chapter 3 is a description of the instrumentation, data processing and measuring techniques that was used to study the boundary layer beneath ice in the Arctic. Although, the acoustic system was developed by Jasco Research, under contract to the Institute of Ocean Sciences, I had the opportunity to be involved with every stage of the project. Specifically, I was responsible for acoustic system simulation and specifications. I participated in the design, manufacture and testing of the electronics. I wrote most system software, including real-time decoding algorithms for the sonars, and communications, testing, monitoring, data analysis and display software. I also designed and helped assemble the moorings, and planned and prepared for the arctic experiment.

Chapter 4 is an overview of our observations, and an analysis of the factors that limit the accuracy of the path-averaged measurements. Except as otherwise noted, I am responsible for all the material included in Chapter 4. I participated in the CEAREX oceanography ice camp, helped during the deployment and recovery of the ice camp, was responsible for the deployment, operation and recovery of the acoustic system, and carried out all data analysis discussed in Chapter 4.

A new measurement technique for the acoustical remote sensing of velocity fine structure, based on reciprocal travel time scintillation analysis is described in Chapter 5. This chapter contains the most significant original contribution of the thesis. Existing theory, regarding the statistical description of turbulence, has been extended to interpret reciprocal travel time scintillations in terms of the

intervening velocity fine structure.

Amplitude scintillation analysis of the data is carried out in Chapter 6; energy dissipation rate is estimated from amplitude scintillations and compared with an estimate from reciprocal travel time measurements. No part of the theory presented in this chapter is new. However, the measurements are unique: for the first time it is possible to estimate acoustically the contribution of velocity and sound speed fine structure to forward scatter scintillations.

In Chapter 7, we exploit the path-averaged nature of the current measurements to detect surface gravity waves, which could not be detected by conventional current meters at the ice camp. This is an interesting exercise which demonstrates the sensitivity of the acoustical current meter, and confirms the ubiquitousness of low frequency swell, away from coastal regions in the world's oceans.

Internal waves, propagating in stratified water beneath the ice camp, are discussed in Chapter 8. The sensitivity and path-averaged nature of the acoustic measurements are used to observe internal waves that are below the resolution of conventional instrumentation. Simultaneous observations at two depths are compared. The passage of an energetic wave packet is reported. The description of the energetic wave packet includes material from a joint publication [13]; in Chapter 8, I emphasize and expand upon my contribution to the paper.

Chapter 2

Background

Since the drift of the Fram in 1893–6, it has been known that ice floes are not stationary, but drift under the influence of wind, oceanic currents, internal ice stress and the rotation of the earth. During the expedition, Nansen [57] observed that the ice consistently veered 20° to 40° to the right of the surface wind and surmised that the deviation resulted from the Coriolis force. These observations led to the development of Ekman's theory on sheared fluids in a rotating reference frame. With minor modifications, to account for a thin region of intense shear near the ice-ocean interface, Ekman's theory is still in use today; it is discussed in Section 2.2 in the context of momentum transfer from the atmosphere to the ocean.

Nansen also made the first scientific observations of the generation and propagation of internal waves. During his passage across the Barents Sea, he noticed that the progress of his ship, the Fram, was considerably impeded when sailing through a thin layer of fresh water overlying saltier water. Ekman confirmed theoretically that the passage of the ship was generating interfacial waves and that the momentum of the ship was reduced by the transfer of its momentum to the waves which it generated. Internal waves are further discussed in Section 2.3.

From August 1988 to May 1989, the Coordinated Eastern Arctic Experiment (CEAREX) was staged in the Arctic to obtain a better understanding of the oceanography and acoustic transmission properties of the Arctic Ocean and ad-

joining seas. Sponsored by the U.S. Office of Naval Research, CEAREX involved participants from the USA, Canada, Norway and the UK. The measurements described herein were obtained at the CEAREX oceanography ice camp. An overview of the experiment is given in Section 2.4.

2.1 Statistical Description of Random Fields

Before discussing turbulence and waves, it is appropriate to introduce the concept of random fields, and the statistical functions used to characterize these fields. The physical parameters of the water column—temperature, salinity, pressure, current velocity, *etc.*—and ice cover—tilt, strain, thickness, *etc.*—of the Arctic Ocean vary in time and space, and depend on one another and on external effects. For example, turbulence and waves generate measurable fluctuations of temperature, pressure, velocity, and other parameters. In most cases, detailed measurement of all pertinent physical properties of the medium is not practical. For convenience, or out of necessity, the parameters of interest are treated as random fields and are described by their average characteristics.

The description of random fields is based on ensemble averaging of certain quantities over a large number of flow realizations. In practice, ensemble averages can often be replaced by time (or space) averages, which are more readily available. This substitution is possible for flows that are stationary and ergodic. Stationarity implies that the statistical properties of the flow do not change with time (or space—a spatially homogeneous flow is said to be stationary in space). Under most experimental conditions, stationary fields are also ergodic [5].

The basic statistical properties used for describing stationary random fields in this thesis are

1. the mean,
2. the variance,
3. the autocorrelation function,

4. the autospectral density function,

5. the cross-correlation function,

6. the cross-spectral density function,

7. the frequency response function,

8. and the coherence function.

The first four items describe a single random process, while the last four measure properties shared by two different stationary random processes.

2.1.1 Correlation Functions

Consider two stationary random functions of time, $x(t)$ and $y(t)$. The mean value of $x(t)$ is

$$\mu_x = \langle x(t) \rangle \approx \overline{x(t)} = \frac{1}{T} \int_0^T x(t)\, dt, \tag{2.1}$$

where the angle brackets indicate ensemble averaging and the overbar indicates time averaging. For an ergodic process, the true mean value can be obtained by letting the averaging period T approach infinity. In practice, T is finite, and we can only estimate μ_x. The variance of $x(t)$ is

$$\sigma_x^2 = \langle [x(t) - \mu_x]^2 \rangle, \tag{2.2}$$

the average of the square of the deviation from the mean value. The standard deviation σ_x is the positive square root of the variance, and is equal to the root mean square (rms) value if the mean μ_x is zero. A generalization of the concept of variance is the covariance function

$$C_{xy}(\tau) = \langle [x(t) - \mu_x][y(t+\tau) - \mu_y] \rangle, \tag{2.3}$$

where the delay τ can be either positive or negative. The correlation coefficient function is defined as

$$\rho_{xy}(\tau) = \frac{C_{xy}(\tau)}{\sigma_x \sigma_y}, \tag{2.4}$$

and satisfies $-1 \leq \rho_{xy}(\tau) \leq 1$, for all τ.

The cross-correlation function between $x(t)$ and $y(t)$ is

$$R_{xy}(\tau) = \langle x(t)y(t+\tau) \rangle. \tag{2.5}$$

From the stationary hypothesis, it follows that

$$R_{xy}(-\tau) = R_{yx}(\tau). \tag{2.6}$$

For random functions that have zero mean, $\mu_x = \mu_y = 0$, $R_{xy}(\tau)$ and $C_{xy}(\tau)$ can be interchanged as we have done in Section 6.2. The autocorrelation function of $x(t)$,

$$R_x(\tau) = \langle x(t)x(t+\tau) \rangle, \tag{2.7}$$

is a special case of $R_{xy}(\tau)$ when $x(t) = y(t)$. Note that for $\tau = 0$, the autocorrelation function is equal to the mean square value of $x(t)$,

$$R_x(0) = \langle x^2(t) \rangle. \tag{2.8}$$

Spatial, instead of time-lagged correlation functions can also be defined. For example, in Section 5.2.1, Equation (5.5), we introduce the spatial correlation tensor $R_{ij}(\mathbf{r})$ to describe a homogeneous turbulent velocity field.

Equations (2.5) and (2.7) describe correlation functions for stationary random functions, which by definition contain infinite total energy but finite average power. For signals whose total energy is finite, a somewhat different definition of correlation must be used:

$$\mathcal{R}_{xy}(\tau) = \int_{-\infty}^{\infty} x(t)y(t+\tau)\, dt. \tag{2.9}$$

This is the type of correlation function discussed in Section 3.2.

2.1.2 Spectral Functions

The cross-spectral density function

$$F_{xy}(f) = \frac{1}{T}\langle X_T^*(f) Y_T(f)\rangle, \tag{2.10}$$

is defined in terms of the finite Fourier transforms,

$$X_T(f) = \int_0^T x(t)\exp(-i2\pi f t)\,dt \tag{2.11}$$

and $Y_T(f)$, of the data records, $x(t)$ and $y(t)$; the asterisk denotes a complex conjugate. $F_{xy}(f)$ is a measure of properties shared by $x(t)$ and $y(t)$ in the frequency domain. For stationary random data, the cross-spectral density function,

$$F_{xy}(f) = \int_{-\infty}^{\infty} R_{xy}(\tau)\exp(-i2\pi f\tau)\,d\tau, \tag{2.12}$$

is the Fourier transform of the cross-correlation function $R_{xy}(\tau)$ (2.5), so that

$$R_{xy}(\tau) = \int_{-\infty}^{\infty} F_{xy}(f)\exp(i2\pi f\tau)\,df. \tag{2.13}$$

Notice that at $\tau = 0$,

$$R_{xy}(0) = \int_{-\infty}^{\infty} F_{xy}(f)\,df, \tag{2.14}$$

and from the symmetry property of stationary correlation functions (2.6), it follows that

$$F_{xy}(-f) = F_{xy}^*(f) = F_{yx}(f). \tag{2.15}$$

$F_{xy}(f)$ is defined for $-\infty < f < \infty$, and is mostly used for theoretical work as we have done in Chapters 5 and 6 while discussing scintillation theory. For

experimental work, it is more convenient to use the one-sided density function,

$$G_{xy}(f) = \begin{cases} 2F_{xy}(f) & \text{for } 0 \leq f < \infty \\ 0 & \text{otherwise} \end{cases}, \tag{2.16}$$

as we have done in Chapters 4, 7 and 8.

The autospectral density functions, $F_x(f)$ and $G_x(f)$, are special cases of $F_{xy}(f)$ and $G_{xy}(f)$ for $x(t) = y(t)$. They are also called power spectral density functions, or simply power spectra, and they measure the rate of change of mean square value of $x(t)$ with frequency. From (2.8) and (2.14), it follows that the total area under the autospectral density function over all frequencies is the mean square value of the record. The partial area from f_1 to f_2 under $G_x(f)$ represents the mean square value of $x(t)$ associated with that frequency range.

In practice, spectral density functions are evaluated using Fast Fourier Transform (FFT) algorithms [65]. In computing spectral density functions throughout this thesis, we carry out the following steps [5].

1. We divide the available data record into several contiguous segments (with 50% overlap to reduce the variance increase caused by tapering).

2. We detrend each segment to avoid the distortion that can be caused by a large low-frequency bias.

3. Each segment is tapered using a cosine squared (also called Hanning) window to suppress side-lobe leakage.

4. We compute the FFT of each segment.

5. We adjust the scale factor of the FFT by $\sqrt{8/3}$ to compensate for Hanning tapering.

6. We compute the spectral density function using (2.10) for a two-sided estimate or (2.16) for a one-sided estimate.

7. The 95% confidence interval is estimated by calculating the variance of the unaveraged spectral estimates under the assumption of a normal distribution.

Autospectral and cross-spectral density functions can be used to compute the theoretical linear frequency response function, and the coherence function between records as discussed below.

The frequency response function of a constant-parameter, single-input/single-output linear system is

$$H(f) = \int_{-\infty}^{\infty} h(\tau) \exp(-i2\pi f\tau)\, d\tau, \tag{2.17}$$

the Fourier transform of the unit impulse response function $h(\tau)$ which describes the system. In complex polar notation, the frequency response function can be written

$$H(f) = |H(f)| \exp[-i\phi(t)], \tag{2.18}$$

where $|H(f)|$ is the gain factor and $\phi(t)$ is the phase factor of the system. Under ideal conditions, the output,

$$y(t) = h(t) * x(t) = \int_{0}^{\infty} h(\tau)x(t-\tau)\, d\tau, \tag{2.19}$$

is given by the convolution of the input, $x(t)$, and the unit impulse response function $h(t)$. In the frequency domain, (2.19) can be written as

$$Y(f) = H(f)X(f), \tag{2.20}$$

where $Y(f)$, $H(f)$ and $X(f)$ are the Fourier transforms of $y(t)$, $h(t)$ and $x(t)$, respectively. It can be shown that the input/output cross-correlation function [5],

$$R_{xy}(\tau) = h(\tau) * R_x(\tau), \tag{2.21}$$

is the convolution of the impulse function and the autocorrelation function of the input signal. Taking the Fourier transform of (2.21), we obtain

$$F_{xy}(f) = H(f)F_x(f). \tag{2.22}$$

Equations (2.21) and (2.22) are used in Section 3.2.4 and Appendix A to derive a theoretical expression for the shape of the correlation peak. For linear systems, $H(f)$ can be estimated using deterministic or stationary random data, since its properties are independent of the nature of data passing through the system. Equations (2.20) and (2.22) suggest two methods of estimating the frequency response function,

$$H(f) = \frac{Y(f)}{X(f)} = \frac{F_{xy}(f)}{F_x(f)}, \tag{2.23}$$

between two data records $x(t)$ and $y(t)$.

The coherence (also called coherency squared) function,

$$\gamma_{xy}^2(f) = \frac{|F_{xy}(f)|^2}{F_x(f)F_y(f)}, \tag{2.24}$$

of two data records, $x(t)$ and $y(t)$, is the ratio of the square of the absolute value of the cross-spectral density function to the product of the autospectral density functions of the two records. For all f, $\gamma_{xy}^2(f)$ satisfies $0 \leq \gamma_{xy}^2(f) \leq 1$. The coherence function is a measure of the extent to which $x(t)$ and $y(t)$ can be assumed to be related by a linear input/output frequency response function.

2.1.3 Nonstationary data

The correlation and spectral functions discussed in Sections 2.1.1 and 2.1.2 are restricted largely to the measurement and analysis of stationary random data. Much of the random data of interest in practice is nonstationary when viewed as a whole. Although no general methodology for analyzing the properties of all

types of nonstationary data exists, some special techniques have been developed that can be applied to limited classes of nonstationary data [5]. A subset of these techniques will be introduced in this section.

One common practice when analyzing data that is nonstationary as a whole is to consider the random field as piecewise stationary. This idea is used in Section 5.2.2 for describing properties of inhomogeneous turbulence.

Another useful formalism for the analysis of nonstationary data is to define correlation and spectral functions that can vary with the time and location of the measurement. For example, the correlation functions defined by (6.3) and (6.14) in Section 6.2 depend not only on time lag τ and separation $\mathbf{r}$, but also on time t and location $\mathbf{x}$.

The final approach to be considered here is the decomposition of the data into mean and fluctuating quantities. This technique is extensively used in turbulence studies where it is known as Reynolds' decomposition. It involves writing a certain property of the fluid,

$$U = \overline{U} + u, \tag{2.25}$$

in terms of a mean value, $\overline{U}$, and a fluctuating component, u. Once this has been done, $\overline{U}$ is viewed as a deterministic quantity and u is a random variable described by its statistical characteristics. The equations of motion are then used to develop an understanding of the evolution of $\overline{U}$ and the statistics of u. For this reason, the averaging scheme used must satisfy the following requirements [63].

1. The averages must be differentiable up to any order required by the equations of motion.

2. The averaging process must satisfy the Reynolds' postulates that

   (a) all fluctuation quantities must average to zero,

   (b) the correlation between fluctuations and average quantities must vanish,

(c) and the averaging process applied to an average quantity must reproduce the same average.

The only averaging operation that satisfies all the above requirements is the ensemble average, but in practice time or space averages have to be used. Moving averages, and linear regression fits to nonoverlapping portions of a time series, are the two most common methods of taking time averages in turbulence studies. Strictly speaking, these two methods do not satisfy all the requirements listed above unless $\overline{U}$ and u are separated by a large spectral gap [63]. Unfortunately, such a spectral gap is rarely observed in the atmosphere or the ocean, and it seems impossible to distinguish rigorously between wave motion and turbulence [72]. For this reason, caution must be exercised in the choice of the averaging method, and in the interpretation of the average and fluctuating quantities.

2.2 Oceanic Boundary Layer in the Arctic

By comparison to the open ocean, the oceanic boundary layer in the Arctic is a quiet place. The ice cover inhibits surface wave action and the direct exchange of heat and mass with the atmosphere. The ice also has a profound effect on the manner in which momentum is transferred from the atmosphere to the ocean. Mechanical energy is transferred from the atmosphere to the ice, which in turn acts on the ocean. R.W. Stewart (1993, personal communication) has suggested that as a result of the low drag coefficient of surface waves [71], and depending on the roughness of the ice, the ice may actually enhance momentum transfer between the atmosphere and the ocean.

In the Arctic Ocean, the mean currents are generally on the order of 2 to 3 cm/s and the rms ice velocity is on the order of 7 cm/s [51]. As a result, the currents near the surface are dominated by boundary-layer motion. The typical current velocity profile under the ice includes three more or less separate components.

1. A thin layer (typically 2–5 m) of intense shear adjacent to the ice, where the

velocity profile relative to the ice is logarithmic and unidirectional, is called the surface layer by analogy to terminology in the atmospheric boundary layer. This region is further discussed in Section 2.2.2.

2. A region farther from the interface, where the relative velocity vector turns noticeably with depth in a decreasing spiral, is known as the Ekman layer. The spiral results from the balancing between the Coriolis and friction forces. Its depth (typically 40 m to 80 m) is defined to extend to where the current velocity has veered 180° and fallen to 4% of the surface value.

3. Finally, there is a geostrophic current associated with the slope of the sea surface and not dependent on recent, local wind. This current results from a balance between the Coriolis and pressure forces.

The first two layers form the mixing layer; turbulent mixing driven by shear and buoyancy forces homogenizes the temperature and salinity structure. It is worthwhile to note that although there have been few good observations of the predicted spiral in the open ocean and the atmosphere [70], the conditions in the arctic boundary layer are such that true spirals are often observed under ice, provided the currents are averaged long enough so that inertial effects are not dominant [44].

An important factor in determining ice velocity relative to the underlying ocean is the topographic relief of the ice bottom. The hydraulic roughness manifests itself both in small scale roughness responsible for generating turbulent skin friction and as a larger scale distribution of pressure ridge keels which exert a form drag analogous to mountain drag in the atmosphere.

In an ice-covered ocean, the near-surface waters are held very near the freezing point. At these temperatures, the density is controlled mainly by changes in salinity. For this reason, the density structure depends mostly on salt concentration in contrast to most other regions in the ocean where density is controlled by temperature. In the summer, the thickness of the ice cover is reduced by melt-

ing water beneath the floe. Thereby, the salinity of the surface waters decreases. This increased stratification inhibits turbulent mixing and the mixed-layer depth is reduced.

During the winter, surface cooling causes freezing of sea water and formation of new ice. The freezing process rejects salt and increases the salinity of the water adjacent to the ice. This creates a buoyancy imbalance that enhances the turbulent mixing of the boundary layer. Sinking salty water from the turbulent region encounters a region of increased salinity below the mixed layer; its vertical velocity is retarded and eventually reversed. In the process, however, it usually mixes with some of the warmer water beneath the boundary layer and brings it up to be incorporated into the turbulent region. This entrainment results in the steady increase of the mixed layer and in an upward heat flux through the boundary layer that eventually balances out the heat lost through the ice to the atmosphere and inhibits further ice growth.

As further discussed in Section 6.3.1, temperature and salinity fluctuations in the arctic oceanic boundary layer are relatively small. The practical consequence of this is the requirement of highly sensitive instrumentation to measure the sound speed fluctuations of the medium.

2.2.1 Basic Equations

In this section we state the equations used to model the behaviour of the boundary layer. It is often assumed that the mixed layer is horizontally homogeneous [46]. Therefore, the conservation of momentum equation for a turbulent flow can be written as

$$\frac{\partial \overline{\mathbf{V}}}{\partial t} + f\mathbf{k} \times \overline{\mathbf{V}} + \frac{1}{\rho}\nabla P - g\mathbf{k} + \frac{\partial}{\partial z}(w\mathbf{v}) = 0, \tag{2.26}$$

where $\overline{\mathbf{V}}$ and $\mathbf{v}$ are the mean value and fluctuations of horizontal velocity, and boldface print indicates a vector quantity. This is a modified version of Navier-Stoke's equation with simplifications due to the horizontal homogeneity of the

medium (*i.e.* the partial derivatives with respect to x and y are negligible compared to the other terms of the equation), the assumption that vertical velocity has zero mean, and the addition of Coriolis and Reynolds' terms. The viscous term is omitted since it is negligible compared with friction caused by turbulence (high Reynolds' number). Each term of (2.26) is described below.

1. The first term is the average horizontal acceleration of the fluid.
2. The Coriolis term accounts for the effect of the earth's rotation; k is a unit vector along the vertical coordinate axis z, $f = 2\Omega \sin \Phi$, where Ω is the angular speed of rotation of the earth about its axis, and Φ is the geographic latitude.
3. Although the fluid is assumed horizontally homogeneous, a large-scale horizontal pressure gradient $\nabla_{\|} P$ is allowed to account for sea surface slope. The vertical pressure gradient balances gravity; ρ is the fluid density.
4. The fourth term is the gravitational acceleration g at the surface of the earth.
5. The last term is the vertical gradient of Reynolds' stress where w is the vertical velocity component.

The solution of Equation 2.26 is difficult because of the nonlinearity of the last term. To a first approximation, the effect of the turbulent fluctuations on the mean flow can be considered analogous to the effect of molecular motion as developed in the kinetic theory of gases. Reynolds' stress can therefore be written

$$\tau = -\langle w\mathbf{v} \rangle \approx K_z \frac{\partial \overline{\mathbf{V}}}{\partial z} \tag{2.27}$$

in terms of an eddy viscosity coefficient K_z. This is a simple example of a closure procedure.

We can also write conservation equations for heat

$$\frac{\partial \overline{T}}{\partial t} + \frac{\partial}{\partial z} \langle wT' \rangle = \frac{Q_T}{\rho c_p} \tag{2.28}$$

and salinity

$$\frac{\partial \overline{S}}{\partial t} + \frac{\partial}{\partial z}\langle wS' \rangle = Q_S \tag{2.29}$$

where $\overline{T}$ and T' are the mean and turbulent fluctuations of temperature, Q_T is a source term for heat in fluid with heat capacity c_p, $\overline{S}$ and S' are the mean and turbulent fluctuations of salinity, and Q_S is a source term for salinity. As for the momentum equation, we can define eddy conductivity K_T and eddy diffusion K_S for salt so that

$$-\langle wT' \rangle \approx K_T \frac{\partial \overline{T}}{\partial z} \tag{2.30}$$

and

$$-\langle wS' \rangle \approx K_S \frac{\partial \overline{S}}{\partial z}. \tag{2.31}$$

Finally, the approximate equation of state for seawater is

$$\frac{\Delta \rho}{\rho} = -\beta_T \Delta_T + \beta_S \Delta_S \tag{2.32}$$

where $\beta_S \approx 8.1 \times 10^{-4}$ in polar waters and β_T is a function of temperature, salinity and pressure. McPhee [46] discusses several methods used to find approximate solutions to the above equations in the arctic boundary layer.

2.2.2 Surface Layer

Under steady state conditions, there often exists a region near the ice where the Reynolds' stress (2.27) of the fluid does not appreciably change magnitude,

$$\tau(z) \approx \tau_o, \tag{2.33}$$

or direction with depth z. If in addition to constant stress, the buoyancy fluxes caused by freezing or melting of the ice are negligible, then, on dimensional grounds,

the mean velocity gradient is [71]

$$\frac{\partial \overline{U}(z)}{\partial z} = \frac{u_*}{\kappa z}, \tag{2.34}$$

where u_* is the friction velocity associated with stress by $\tau_o = \rho u_*^2$, ρ is seawater density, and $\kappa \approx 0.4$ is Von Kármán's constant. This region is commonly called the surface layer and comprises roughly one tenth of the mixing layer under ice [44]. In this region, the rate of turbulent kinetic energy production by the working of the stress on the mean gradient is equal to the dissipation rate,

$$\tau_o \frac{\partial \overline{U}(z)}{\partial z} = \epsilon(z) = \frac{\rho u_*^3}{\kappa z}, \tag{2.35}$$

and integrating (2.34), we find that the mean velocity profile varies logarithmically with distance from the boundary,

$$\overline{U}(z) = \frac{u_*}{\kappa} \ln(z/z_o), \tag{2.36}$$

where z_o is a length scale known as the roughness length. It is common to relate the turbulent stress near the surface,

$$\tau_o = \rho C_D(z) \overline{U}^2(z), \tag{2.37}$$

to the mean ice-relative velocity $\overline{U}(z)$ at depth z, by the quadratic drag coefficient $C_D(z)$. In the surface layer, the drag coefficient,

$$C_D(z) = \frac{u_*^2}{\overline{U}^2(z)} = \left[\frac{1}{\kappa} \ln(z/z_o)\right]^{-2}, \tag{2.38}$$

is the square of the ratio of friction velocity to mean ice-relative velocity. A surface layer with similar characteristics is also observed in the atmospheric boundary layer above the ice. In Section 6.5.4, we use the approximations introduced here to infer stress, drag coefficient and roughness length above and below the ice.

2.2.3 Vorticity Equation

In order to study relative vorticity, we must relax the condition of horizontal homogeneity. The equation for conservation of momentum becomes

$$\frac{\partial \mathbf{V}}{\partial t} + \mathbf{V} \cdot \nabla_{\mathrm{H}} \mathbf{V} + f\mathbf{k} \times \mathbf{V} + \frac{1}{\rho} \nabla_{\mathrm{H}} P + \mathbf{F} = 0 \tag{2.39}$$

where $\mathbf{F}$ represents the contribution from the turbulent friction terms and we have eliminated the vertical pressure gradient with the gravity term. The relative vorticity is defined as the z-component of the curl of the horizontal velocity vector.

$$\zeta_z = (\nabla \times \mathbf{V})_z. \tag{2.40}$$

Taking the curl of Equation 2.39, we obtain

$$\left(\frac{\partial}{\partial t} + \mathbf{V} \cdot \nabla_{\mathrm{H}}\right)(\zeta_z + f) + (\zeta_z + f)\nabla \cdot \mathbf{V} + \nabla \times \mathbf{F} = 0. \tag{2.41}$$

The quantity $(\zeta_z + f)$, the sum of the relative and planetary vorticities, is called the absolute vorticity. Equation 2.41 shows that if a fluid is vorticity-free, it remains so unless vorticity is diffused in by the friction term either from a boundary, or from some other region of the fluid that does contain vorticity. The second term of the equation is recognized as a measure of the tendency of the horizontal flow to diverge ($\nabla \cdot \mathbf{V} > 0$) or converge ($\nabla \cdot \mathbf{V} < 0$). Convergence is associated with a stretching of the vortex lines and an increase in vorticity. Conversely, divergence is associated with a decrease in vorticity. In the arctic boundary layer, vorticity will be caused by the under-ice topography and by changes in the forcing function, i.e. the motion of the floe.

2.3 Internal Waves

Internal gravity waves are ubiquitous to the stratified waters of the world's oceans [35]. They are important in transporting momentum and energy both horizontally

and vertically. The wave field is remarkably constant in space and time, permitting the formulation of a "universal" statistical description [25, 26], yet the processes that generate and dissipate these waves are not well understood. However, internal waves in the Arctic Ocean appear to be more variable than waves in other oceans [38, 37] and hence may allow study of specific mechanisms of wave growth, propagation, and decay [80].

Deep in the ocean, internal waves generate large displacements of water. Vertical displacements at the surface are orders of magnitude smaller and masked by noise from turbulence and wind waves on open seas. In most internal wave models, such surface displacements are ignored and a rigid-lid boundary condition is invoked in which the vertical displacement of the sea surface is set to zero [64]. The ice cover of the Arctic Ocean suppresses surface wave noise and enables direct measurement of vertical displacements of the surface forced by internal waves using tilt sensors deployed on the ice. Internal waves also cause large horizontal displacements of the mixed layer in the inertial to buoyancy frequency range. Ice tilt and mixed layer horizontal velocity measurements of internal waves are further discussed in Chapter 8.

2.4 Coordinated Eastern Arctic Experiment

The area investigated during CEAREX, as well as an overview of operations are shown in Fig. 2.1. In September 1988, the chartered Norwegian research vessel Polarbjørn was escorted by an icebreaker to the position shown in Fig. 2.1 in the central Arctic and allowed to freeze in and drift with the pack ice until December, when it broke free to the east of Svalbard. During this drift phase, oceanographic, acoustic, and ice physics experiments were performed.

For a three-week period from mid-January 1989, Polarbjørn was used for an oceanographic experiment on the Svalbard shelf to the west of Svalbard. This phase of CEAREX is known as the 'Whaler's Bay Ops' after an area to the north

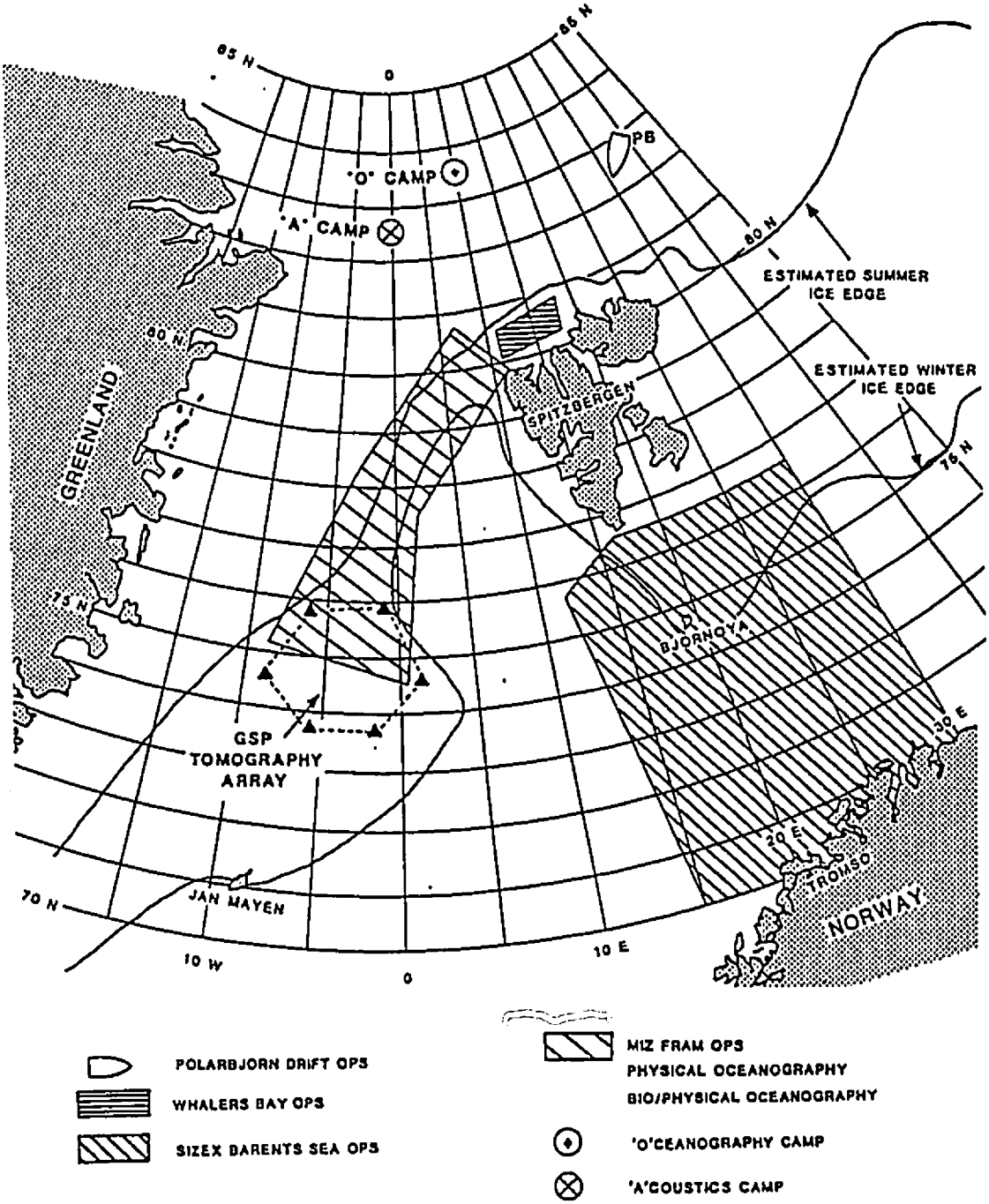

Figure 2.1: CEAREX overview [1].

of Svalbard where the experiment was originally to have taken place (Fig. 2.1). However, unexpected ice conditions in that region necessitated the change in plan. From February 9 to the end of April, the ship acted as the platform for the SIZEX (Seasonal Ice Zone Experiment) and MIZ (Marginal Ice Zone) phases of the experiment in the Barents and East Greenland seas (Fig. 2.1).

In mid-March, the Acoustics Camp (A Camp) and the Oceanography Camp (O Camp) were established on continuous pack ice north of Svalbard (Fig. 2.1). Both camps drifted toward Fram Strait and were evacuated at the end of April. Work at A Camp consisted of acoustic experiments, while most of the work at O Camp was concerned with physical oceanographic experiments.

The Greenland Sea Project tomography array experiment (Fig. 2.1), which took place simultaneously, was to determine the physical structure of the volume of ocean enclosed by the array of acoustic transducers, using the technique of acoustic tomography developed by Munk and Wunsch [55, 56].

2.4.1 Oceanography Ice Camp

The oceanographic objective of the CEAREX O Camp was to measure the processes responsible for the exchange of heat, mass, and momentum between the Arctic Ocean and the atmosphere. The camp was established on March 18, 1989, 300 km northwest of Spitsbergen, and drifted with the pack ice for six weeks (Fig. 2.2).

Most experiments at the ice camp involved lowering instruments through holes which were melted in the ice, on average 2.5 m thick, using steam. These remained open under heated tents which also housed the investigators and their instrumentation. Most investigators were oceanographers interested in measuring tidal currents, and meso- to small-scale processes taking place beneath the sea ice [1]. The measurements confirmed that the Yermak Plateau (Fig. 2.2) is a region of greatly enhanced diurnal tidal currents that are related to plateau topography [62]. These enhanced tides are thought to be responsible for the production of the

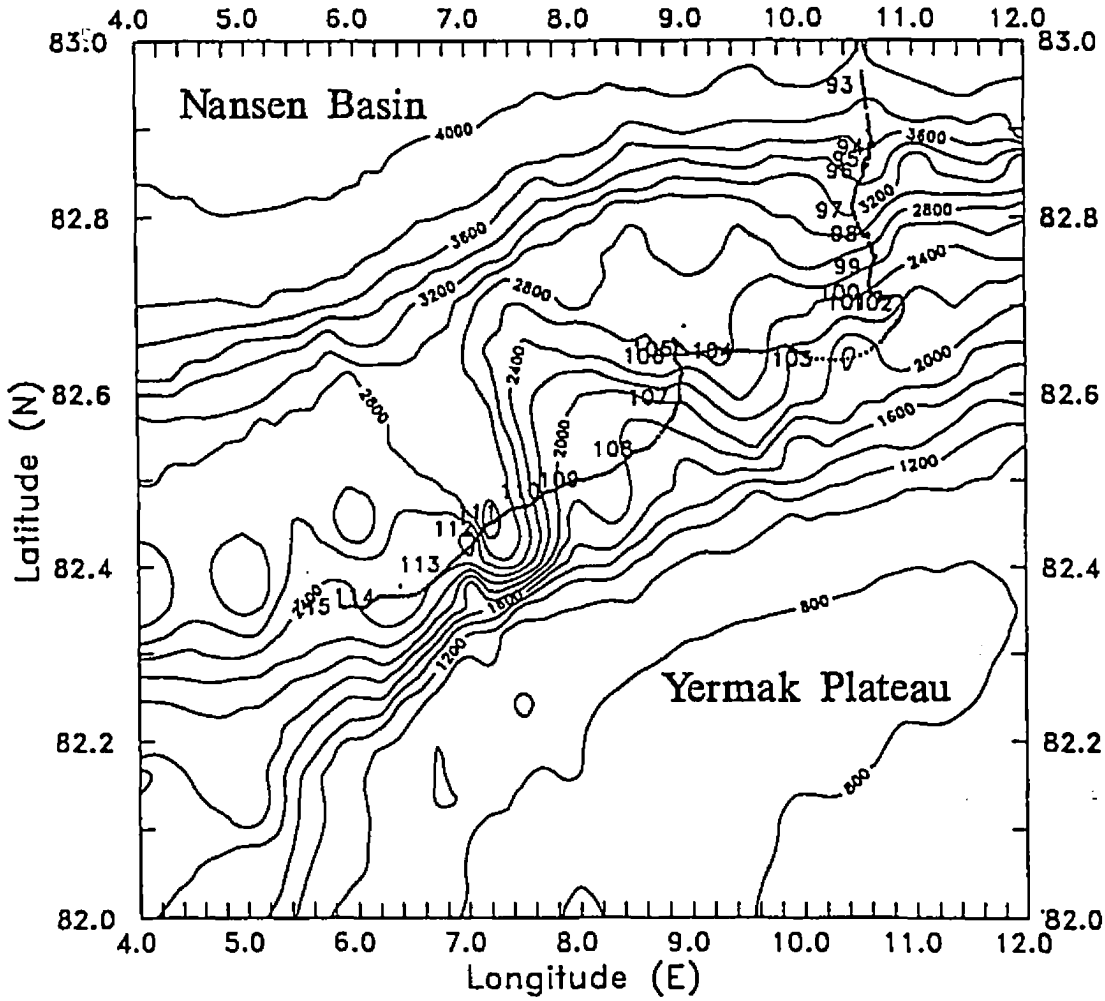

Figure 2.2: Drift track of CEAREX O Camp from April 3 (day 93) to April 25 (day 115), 1989. Depth contours are in meters. Time along drift track is in day of year [60].

high-frequency internal wave packets discussed in Section 8.3. Mesoscale features included 'warm' eddies several kilometers in diameter, which are thought to pinch off from the warmer northward-flowing West Spitsbergen current. Smaller scale features include microstructure and fine structure, in scales ranging from centimeters to tens of meters, which are produced by turbulent and diffusive processes [61, 45]. Of particular interest to many of the scientists were internal waves and their interactions with sea ice [13, 80].

These various processes were measured using the instruments sketched in Fig. 2.3. Two Acoustic Doppler Current Profilers (ADCP) measured vertical profiles of current velocity, using sound. A yo-yo Conductivity, Temperature and Depth (CTD) sensor cycled rapidly down to depths of 600 m to give good temporal and vertical resolution of the internal wave field. A helicopter CTD survey was performed at remote locations in the area surrounding the camp, to give a large-scale picture of temperature and salinity fields in the ocean. A vertical string of current meters, thermistors, conductivity cells and pressure sensors was deployed to obtain point measurements of current velocity, temperature, conductivity and pressure. A vertically-profiling microstructure recorder, a higher resolution ADCP, and movable instrumented frames recorded small-scale variations in the water column. An untethered autonomous vehicle measured horizontal variations in salinity and temperature fields near the camp. An ice sounder was deployed in several locations under the ice to map the topography of the ice from below, from which the ice thickness was inferred (Fig. 2.4).

Our contribution to the measurement program of the oceanography ice camp included the measurement of ocean depth using a 10 kHz echo sounder (Fig. 2.5), and the deployment of a triangular array of acoustic transducers to measure acoustic scintillations, horizontal velocity, and vorticity relative to the ice. The characteristics of the acoustic array, and of the measurements made with it in the boundary layer beneath ice at the CEAREX O Camp are the subject of this dissertation.

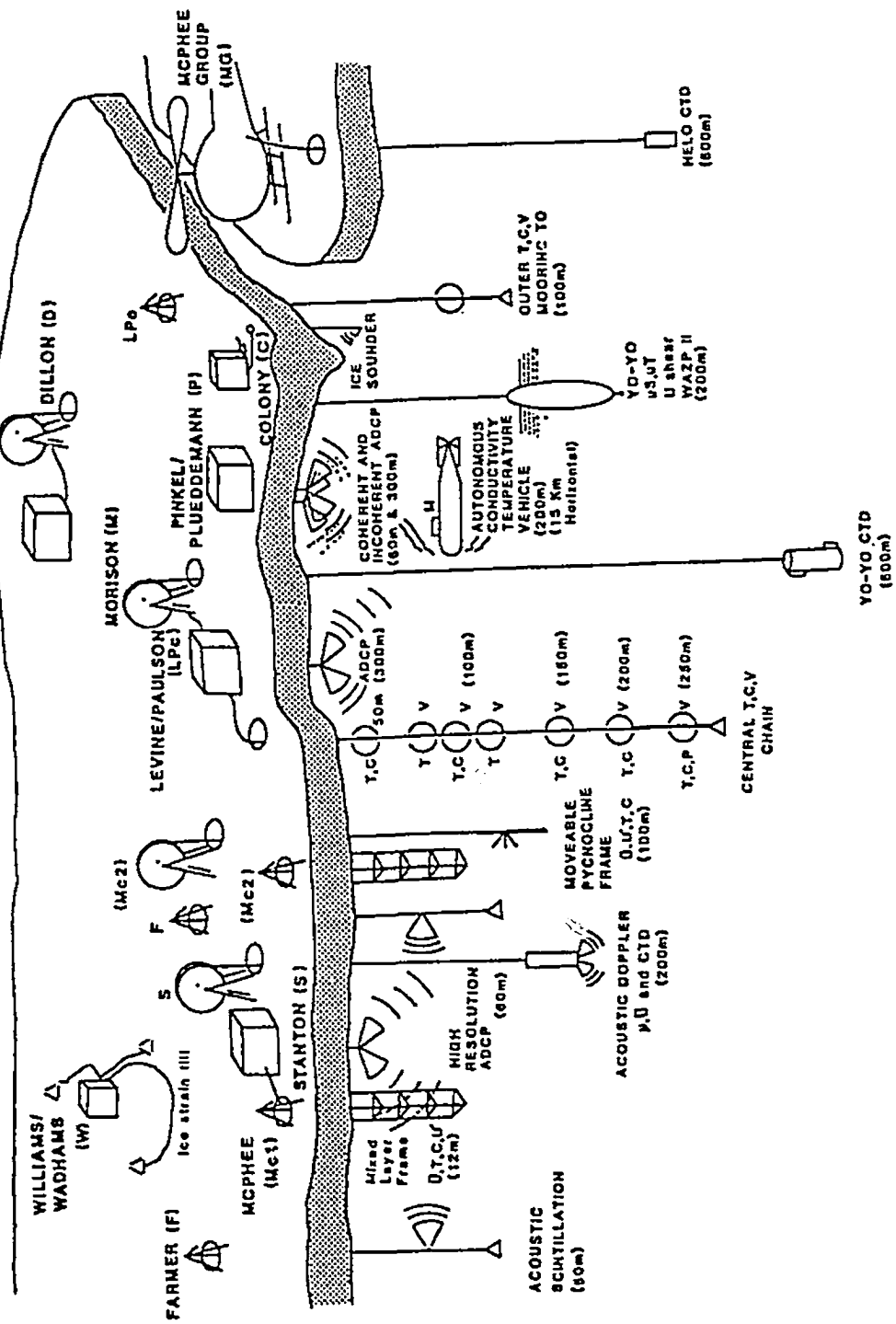

Figure 2.3: Scientific activities at O Camp [1].

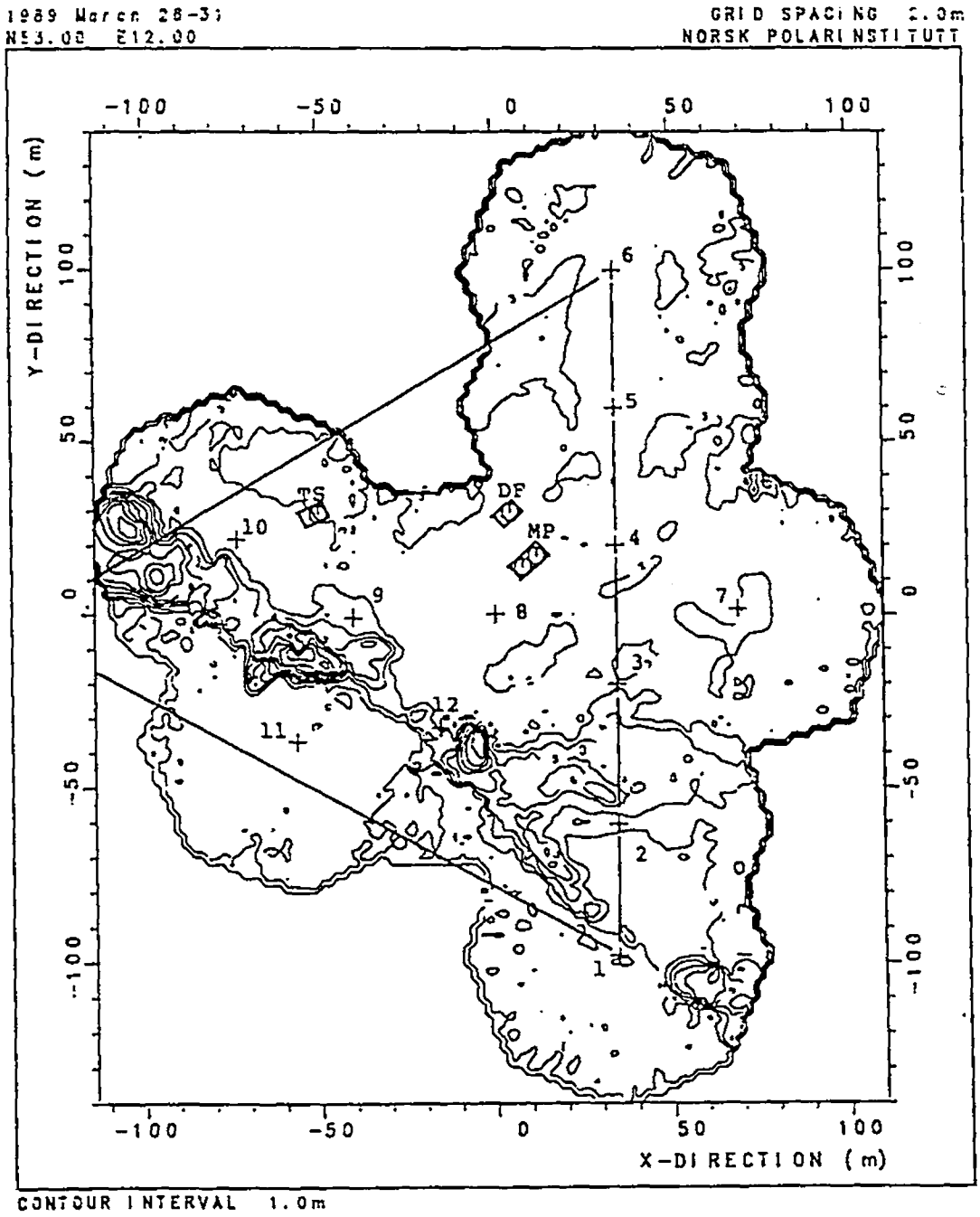

Figure 2.4: Bottom topography of the ice. Contour intervals are 1 m. The heights are vertical distance from the ice bottom to the sea level. The location of the triangular acoustic array is marked on the figure [11].

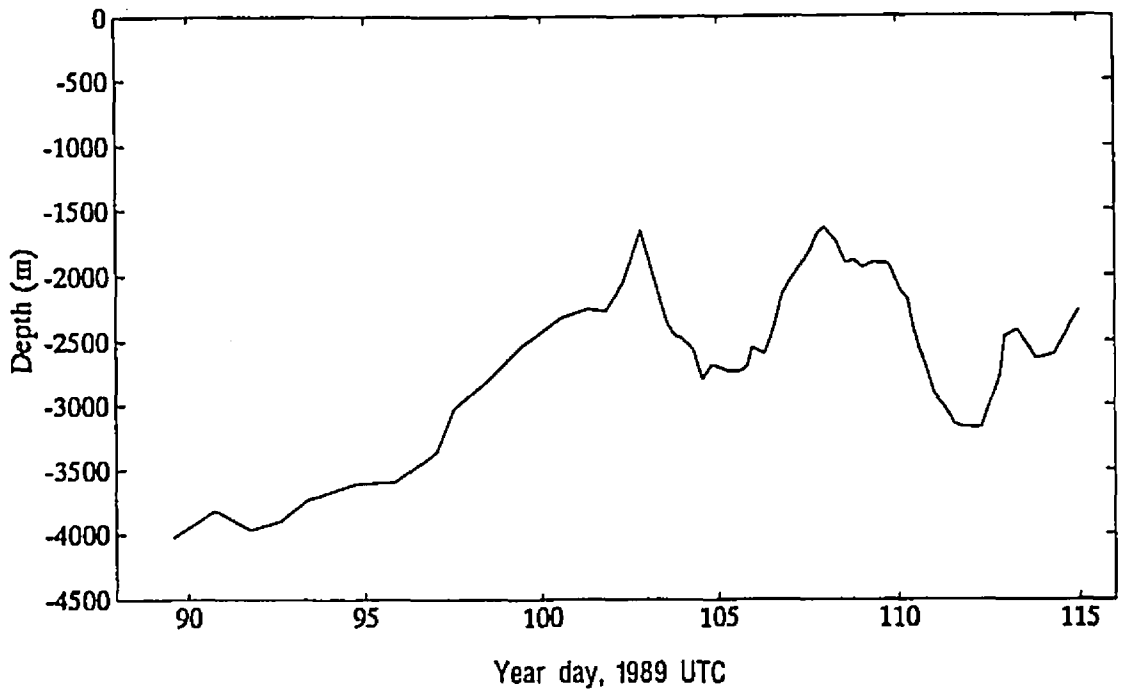

Figure 2.5: Transect of water depth along the drift track of the CEAREX O Camp, from March 30 (day 89) to April 25 (day 115), 1989.

Chapter 3

Description of the Acoustical System

The acoustic system consisted of six underwater units grouped in three clusters located at the corners of a horizontal triangle of side 200 m (Fig. 3.1). At each corner, sonars were deployed at two separate depths beneath the ice. The depth of each triangular array could be manually adjusted between 8 and 100 m. The underwater units were connected to surface electronics contained in a centrally located instrument hut through multiconductor cables. At regular intervals, each sonar emitted a coded acoustic signal which was received, digitized and decoded in real-time by the other units. The accompanying electronics allowed precise measurement and recording of acoustic amplitude and travel time. The simultaneous reciprocal travel time measurement at frequent intervals along each side of the triangular array provided the basic data set from which velocity and average vorticity were subsequently determined.

The quantity of digital information generated by the system posed a formidable processing and storage challenge. The raw data consisted of twenty-four 16-bit channels sampled at 44 kHz. In order to reduce the required recording bandwidth, decoding of the acoustic signal and data reduction was carried out in real time for each sonar. Serial data streams from the sonars were then dispatched to the surface where they were interleaved and stored on video cassette recorder tapes

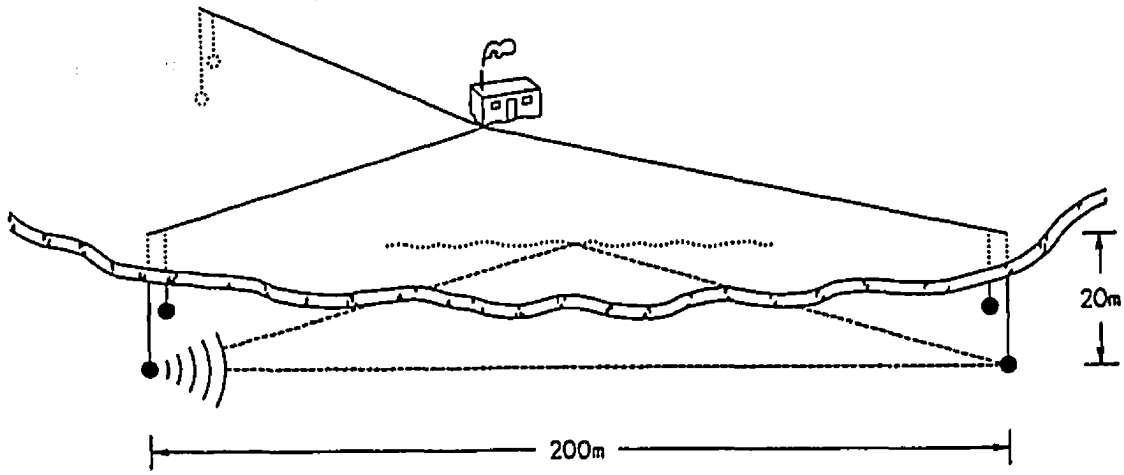

Figure 3.1: Schematic representation of the acoustical system. Underwater units were deployed at two depths at the corners of a horizontal triangle. Velocity and average vorticity are obtained from reciprocal travel time measurements along each side of the array. The direct and ice-reflected acoustic ray paths are depicted for a pair of transmit-receive sonars.

using digital audio technology.

3.1 Instrumentation

3.1.1 Deployment

The six underwater units were deployed at two separate depths at the vertices of an equilateral triangle with sides of length 201, 205 and 211 m; the acoustic array was laid out beneath the floe so as to span both multiyear and young ice, thus providing contrasting turbulence regimes (Fig. 3.2).

Each underwater unit consisted of two sonars mounted on a steel bar and suspended from the ice (Fig. 3.3). The use of paired sensors was intended both to explore the possibility of scintillation analysis and also to provide redundancy. Adjustment of sonar depths was achieved by energizing 1 kW heating wires embedded in slotted PVC tubes surrounding the cables where they passed through the ice. The heating wires melted the water inside the tubes thus freeing the cables for depth adjustment.

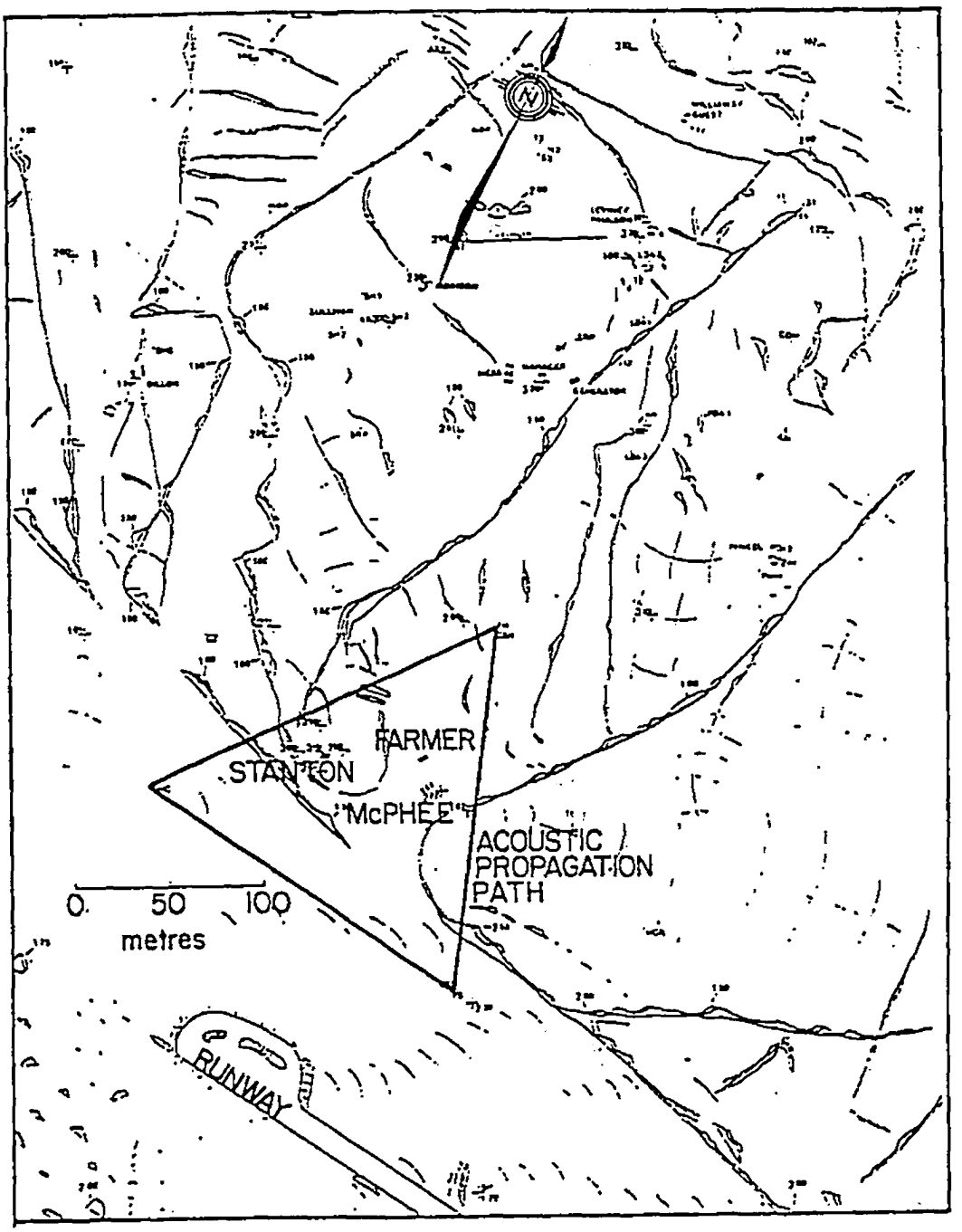

Figure 3.2: Aerial view of CEAREX oceanography ice camp. The camp was located on multiyear ice as indicated by the large number of pressure ridges. The underwater units of the acoustic system were deployed at the corners of the triangle drawn on the diagram. The array is seen to span both first year and multiyear ice [81].

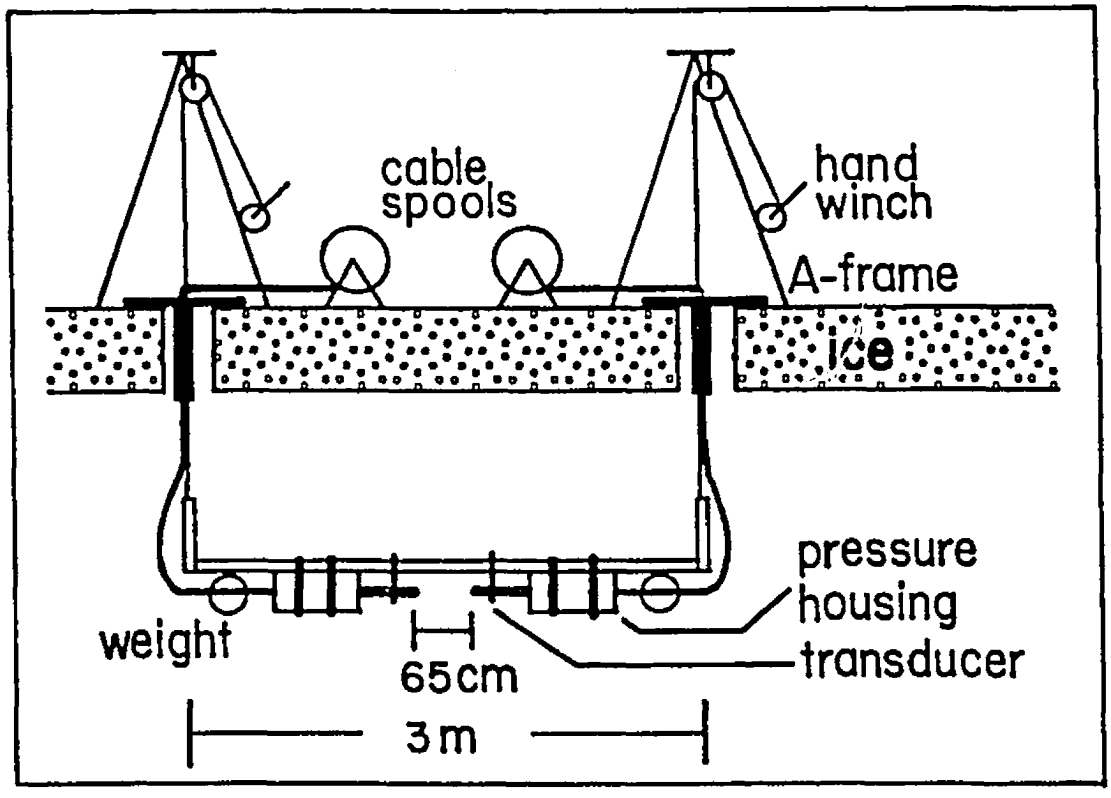

Figure 3.3: Sketch of an underwater unit. Each unit comprised two transducers with accompanying electronics mounted on a steel bar which was suspended horizontally under the ice. The two adjacent transducers were used to measure scintillation drift and obtain horizontal velocity normal to the acoustic paths.

3.1.2 Surface Electronics

The surface modules were responsible for the generation of the analog transmission signal, the timing and control of the acoustic system, and the storage and monitoring of the digital data collected by the sonars (Fig. 3.4). The timing and control unit supplied all system clocks. It derived the clock reference from a pulse code modulation encoder, divided it as required and distributed it to the transmit-signal generator and the sonars. This unit also controlled transmit timing and sequencing. The transmit-signal generator produced the pseudo-random code for transmission. The junction box acted as a traffic controller for signals between the sonars and the rest of the instrumentation; on one side it received wiring from

a) transmit

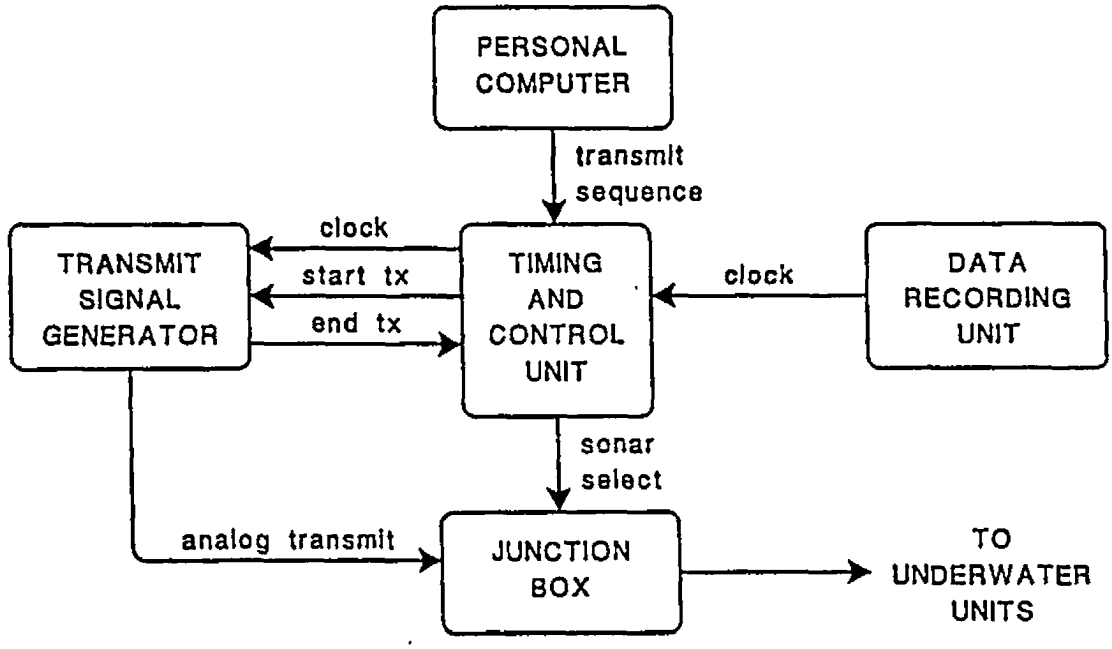

Figure 3.4: Block diagram of the surface electronics. The surface modules are contained in a centrally located instrument hut and are responsible for the generation of the analog transmission signal, timing and control of the acoustic system, and storage and monitoring of the digital data collected by the sonars. The information and data flow between the units is illustrated during (a) transmission and (b) reception of acoustic signals.

the surface electronics, while on the other there were connectors which constituted the starting point of the underwater cables. The data recording unit received processed digital data from the underwater units and stored the data on video tapes using a pulse code modulation encoder. A personal computer was used to specify the transmission sequence, control the sonars, and validate the collected data.

3.1.3 Transmit

Transmission was initiated by downloading a transmission sequence from the personal computer to the timing and control unit (Fig. 3.4a). The transmission sequence most commonly used consisted of firing the transducers located at one corner of the array in quick succession, then waiting 200 ms for all direct and

b) receive

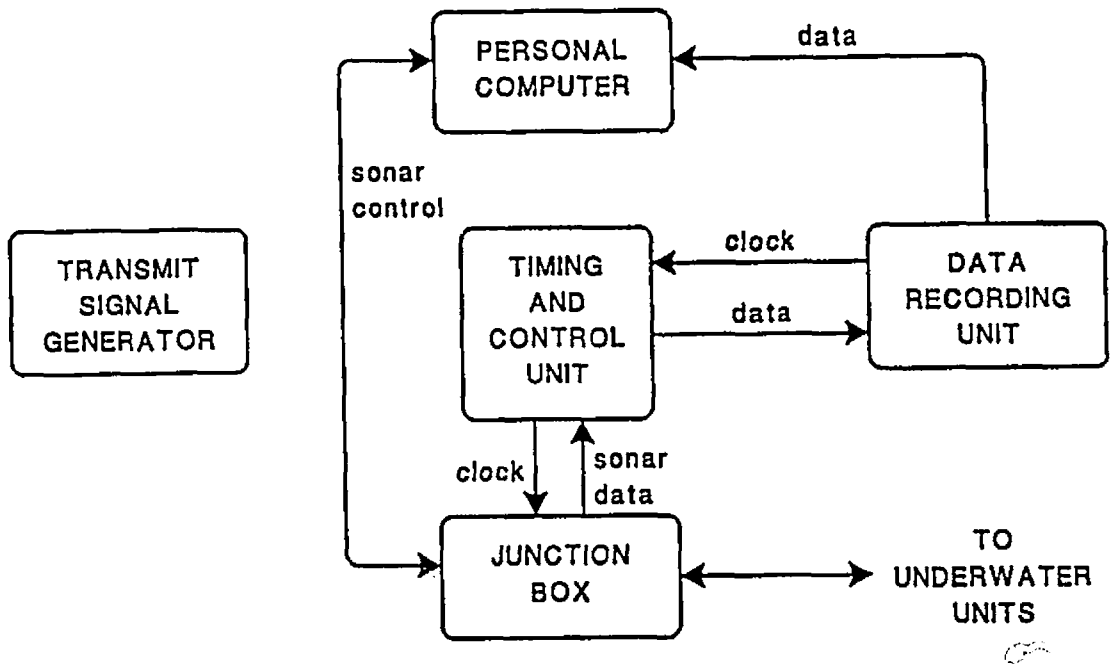

Figure 3.4: *(Continued)*

reflected paths to be received, and finally resetting all sonars before firing the next cluster of transducers. The entire cycle through all the transducers required 910 ms. Following each transmission, the sonars were reset so as to avoid effects of electronic interference on the clock signal.

Once the transmission sequence was downloaded, the timing and control unit took over and the personal computer was available for other tasks. At the appropriate instant, the timing and control unit instructed the transmit-signal generator to start a transmission. The transmit-signal generator generated the analog-transmit signal. An arbitrary waveform of up to 32768 samples was stored in erasable programmable read only memory and played back under clock control. The signal then passed through a digital to analog converter and bandpass filter. One linear power amplifier was used for transmission. When the transmission was complete, the transmit-signal generator informed the timing and control unit, and waited for the next instruction. The junction box contained relays which channeled the

output of the power amplifier to each transducer in succession as directed by the timing and control unit.

3.1.4 Sonars

Each sonar was designed to transmit, receive, digitize and decode pseudo-random, phase encoded acoustic signals using omnidirectional transducers that operated at a nominal frequency of 132 kHz (Fig. 3.5). The transmit/receive switch was of a simple design employing a dissipating resistor and a diode clamp at the input of the preamplifier. Pressure housings were located adjacent to each transducer. Each housing contained data acquisition, signal processing, and communications electronics. Data acquisition and digitizing was carried out with two 16-bit analog to digital converters that performed in-phase and quadrature sampling up to a maximum sampling rate of 50 kHz. During operation, a programmable gain amplifier was set to accommodate the acoustic signal level. The digitized data was decoded in real time by a vector signal processor that cross-correlated the received signal with a template of the code. A separate microprocessor served as host to the signal processor, communicated with the surface electronics and controlled the operation of the data acquisition board. In addition, this microprocessor formatted the decoded data and sent a reduced data set to the surface for storage.

3.1.5 Receive

The sonar data from all underwater units arrived at the surface on serial lines and were combined into a single data stream by the timing and control unit (Fig. 3.4b). The digital data was passed on to the recording unit at a sustained rate of 176.4 kB/s. This unit was made up of a date and time encoder, a pulse code modulation encoder, and video cassette recorders. The date and time encoder inserted timing information directly into the digital stream. In addition, timing information was continuously recorded on the audio channels of the video tapes. The pulse code modulation encoder was a consumer electronics device which converted a video

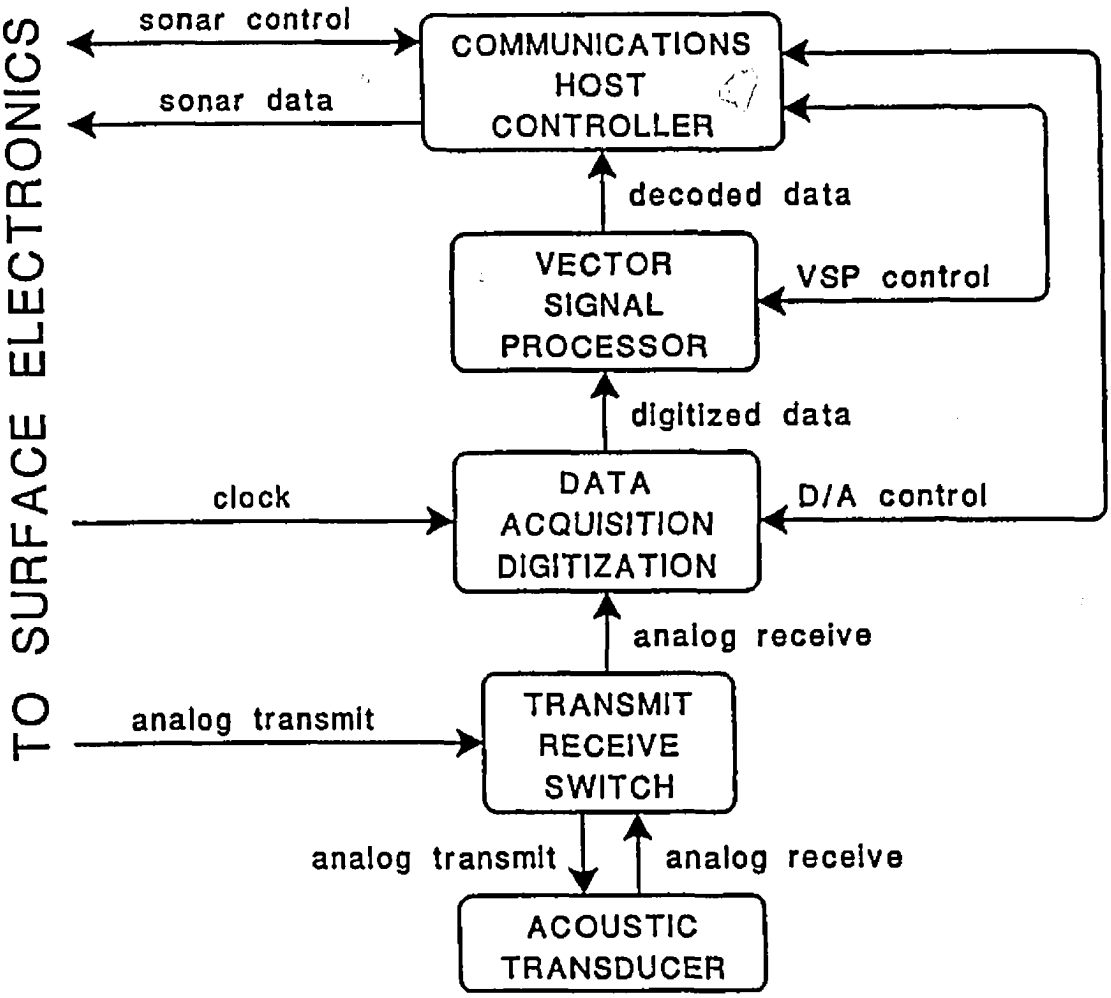

Figure 3.5: Block diagram of the underwater units. Each sonar can transmit, receive, digitize and decode pseudo-random, phase encoded acoustic signals.

cassette recorder into a high fidelity digital audio recorder. We have modified the pulse code modulator by bypassing its internal analog to digital converter so that it may accept digital instead of analog data. The video output was fed to two video cassette recorders allowing sixteen hours of autonomous operation. Each video tape had a total storage capacity of up to 5 GB (8 hours), and was very cost-effective (a fraction of a penny per MB). A personal computer was used to monitor data quality and to control the mode of operation of the sonars.

3.2 Processing

3.2.1 Encoding

The ice-ocean interface is a good reflector of sound. In order to ensure separation of the refracted and ice-reflected acoustic paths (Fig. 3.1), continuous wave transmission is not possible. Acoustic pulses must be used with width,

$$\tau_p < \frac{\sqrt{\ell^2 + 4d^2} - \ell}{2c} \approx \frac{d^2}{c\ell}, \tag{3.1}$$

restricted by range ℓ, depth z, and sound speed c. For example, a 90 μs pulse permits a 200 m range, 5 m beneath the underside of the ice. A rule of thumb which has been used in radar work and related fields [8] is that the successful resolution of a bandpass pulse requires a system bandwidth β satisfying the inequality

$$\beta > \frac{1}{\tau_p} > \frac{c\ell}{d^2}. \tag{3.2}$$

The transmission signals were encoded both to reduce interference from other acoustic instruments deployed at the ice camp, and to improve the precision of the signal amplitude and travel time measurements, given the severe constraint on pulse width established by (3.1).

The coded signal consists of a binary modulation of the 132.3 kHz carrier by a 127-bit pseudo-random code which is a maximal linear sequence [16]. The binary transitions are keyed as 180° phase shifts of the carrier. Each bit is 12 carrier cycles long and has a period of 90.7 μs. The complete sequence lasts 11.5 ms. Table 3.1 summarizes the code and digitizing parameters. A copy of the signal, sampled at 1.06 MHz and digitally prefiltered with a 22 kHz bandpass filter, is stored inside the transmit-signal generator. The 22 kHz bandwidth corresponds to the main lobe of the $[(\sin x)/x]^2$ sequence spectrum, contains 90% of the power in the overall signal, and comfortably satisfies (3.2).

Parameter	*Value*
Carrier frequency f_a (kHz)	132.3
Acoustic signal bandwidth β (kHz)	22
Phase shift used for coding (°)	180
Digital sampling rate f_s (kHz)	44.1
Bit period τ_p (μs)	90.7
Carrier cycles per bit	12
Digital samples per bit	4
Sequence length T (ms)	11.5
Sequence length (bits)	127
Delay between inphase and quadrature sample (μs)	1.89

Table 3.1: Coded sequence and digitizing parameters.

The autocorrelation of a maximal linear sequence, obtained from a n-bit shift register, exhibits a triangular peak at zero lag, of height $2^n - 1$ and duration $2\tau_p$, where τ_p is the width of each bit. On each side of this peak, there are correlation sidelobes of length $(2^n - 2)\tau_p$. Fig. 3.6 displays the autocorrelation function of the pseudo-random sequence used by the acoustic system. In multipath environments, the correlation sidelobes of a reflection may interfere with the peak of the direct path. The amount of interference depends on relative amplitude and delay between each path as a function of time. Under certain conditions, this interference establishes an upper bound on the signal-to-noise ratio of the system which cannot be exceeded even if the transmission power is increased. Depending on the experimental configuration and the multipath environment, the effects of sidelobe interference may be eliminated or minimized by changing the length of the code or adding guard sequences. It is also possible to remove the interference after the measurements are made. The correction is based on the known shape of the sidelobes, the linearity of the correlation operator and the relative amplitude and location of each acoustic arrival.

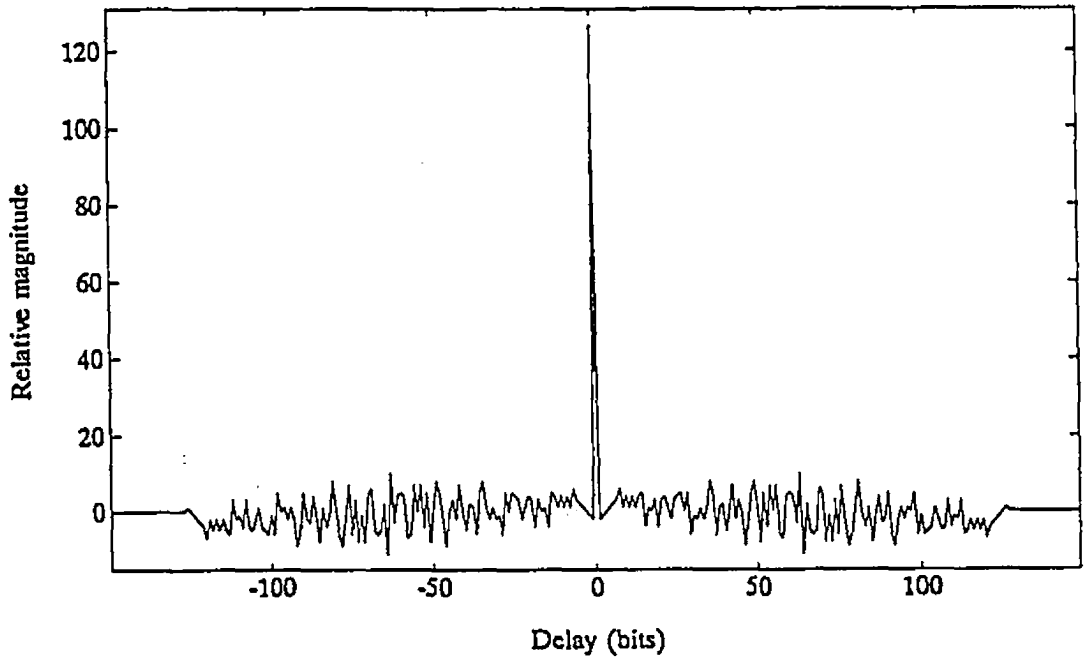

Figure 3.6: Autocorrelation of the pseudo-random sequence used by the acoustic system. The code is generated using a 7-bit shift register. The autocorrelation function exhibits a triangular peak at zero lag, of height $2^7 - 1$ and duration $2\tau_p$, where τ_p is the width of each bit. On each side of this peak, there are correlation sidelobes with peak amplitude smaller than $\sqrt{2^7 - 1}$ and duration $(2^7 - 2)\tau_p$.

3.2.2 Sampling and Decoding

The sampling scheme recovers the in-phase $s_i(t)$ and quadrature $s_q(t)$ components of the acoustic signal relative to the carrier. In-phase samples are collected once every third carrier cycle at $f_s = f_a/3 = 44.1$ kHz, *i.e.* four times per code bit. There is a $(4f_a)^{-1} = 1.89$ μs delay between each in-phase and the corresponding quadrature sample. This digitizing scheme effectively mixes down a 44.1 kHz bandpass signal centered at $f_a = 132.3$ kHz to a 22 kHz lowpass equivalent. This bandwidth is twice that of the acoustic signal, therefore the code information is preserved. The amplitude $A(t)$ and phase $\phi(t)$ of the signal may be recovered from

$$A(t) = \sqrt{s_i^2(t) + s_q^2(t)} \tag{3.3}$$

and

$$\phi(t) = \arctan \frac{s_q(t)}{s_i(t)}, \tag{3.4}$$

as a function of time t.

During normal operation, real-time decoding of the digitized acoustic signals is accomplished at each sonar by the vector signal processor. An unfiltered copy of the code, sampled at 44.1 kHz, is used as a decoding template, and short guard sequences are appended on either side. In-phase and quadrature samples are continuously correlated with this template. The *overlap-save* method [65] is used for performing fast correlation in the frequency domain. The signal processor also computes magnitude squared and lowpass filtered time-series. Synchronization between transmission and reception is achieved by using a common clock. The process gain G is a function of bandwidth β and the total length of the sequence T:

$$G = 10 \log \beta T = 24 \text{ dB}. \tag{3.5}$$

Finally, it must be noted that the quadrature sampling scheme increases the signal-to-noise ratio by an additional 3 dB over and above the process gain defined by (3.5).

3.2.3 Reduction, Storage and Monitoring

The communications processor, contained in each sonar, is programmed to initialize, test and monitor the data acquisition electronics and the vector signal processor, and to communicate with the surface. Under normal operation, it locates four peaks in each block of data. For each set of 512 complex 16-bit samples, 85 data words are produced which preserve most of the useful information contained in the decoded signal. This results in a data reduction rate of twelve to one thereby decreasing the required storage bandwidth.

The reduced data from all the sonars are multiplexed into a single data stream at the surface and stored on video tapes. A personal computer is used to monitor

data quality. During data collection, short samples are written on to disk and subsequently analyzed to verify correct operation of the acoustic system. When the system is not actively monitored by the operator, a background program is used to continuously sample the data and to correct irregularities and malfunctions.

3.2.4 Correlation Peak Interpolation

During post processing, the data is processed in two steps. First, each tape is read at the same rate at which it was written using a pulse code modulation encoder and personal computer. For specified acoustic paths, the location and amplitude of the correlation peaks are obtained using the scheme described in this section. In a typical run, the program will read a 5 GB (8 hour) tape, create a 20 MB file containing information about two dozen acoustic paths, and store this information on erasable optical disk cartridges. A second computational pass is required to convert these data files into time series of amplitude, travel time, path-averaged velocity and relative vorticity as discussed in the next section.

Peak location and amplitude must be interpolated from five data points surrounding the top of each peak. The phase of the acoustic arrival relative to that of the transmitted signal is then used as a vernier scale to improve the estimate of location to within a fraction of a carrier cycle. There is an inherent 360° ambiguity in the measurement of phase using (3.4). Therefore, the interpolation scheme must estimate peak location within half a carrier cycle using data points that are spaced three carrier cycles apart (Table 3.1). The problem is further complicated by the presence of noise and the necessity of implementing the algorithm on data being read at a sustained rate of 176.4 kB/s.

As discussed earlier, the correlation peak exhibits a triangular shape that has a width equivalent to two code bits, or in this case eight data points. The simplest solution for the interpolation problem is a triangular fit through the five recorded data points surrounding each peak. The limited system bandwidth smoothes the peak, so that this approach does not provide the required accuracy.

As discussed in Section 2.1.2, the cross-correlation between input x and output y of a system may be expressed as (2.21)

$$\mathcal{R}_{xy}(\tau) = h(\tau) * \mathcal{R}_x(\tau), \tag{3.6}$$

the convolution of the impulse response $h(\tau)$ with the autocorrelation function of the input signal $\mathcal{R}_x(\tau)$ as a function of delay $\tau = t - t_o$, where t_o is the location of the peak. To a good approximation, the acoustic system is characterized by a band limited frequency response,

$$\mathcal{H}(f) = \begin{cases} 1 & \text{if } -\tau_p^{-1} \leq f \leq \tau_p^{-1} \\ 0 & \text{otherwise} \end{cases}, \tag{3.7}$$

where $\mathcal{H}(f)$ is the Fourier transform of $h(\tau)$. The coded sequence has a triangular autocorrelation function

$$\mathcal{R}_x(\tau) = \begin{cases} A(1 + \tau/\tau_p) & \text{for } -\tau_p \leq \tau < 0 \\ A(1 - \tau/\tau_p) & \text{for } 0 \leq \tau \leq \tau_p \\ 0 & \text{otherwise} \end{cases}. \tag{3.8}$$

We solve this set of equations to obtain an expression for the shape of the cross-correlation peak,

$$\mathcal{R}_{xy}(t) = A \sum_{n=0}^{\infty} a_n \left(\frac{t - t_o}{\tau_p} \right)^{2n}, \tag{3.9}$$

a polynomial with coefficients a_n. The amplitude A and location t_o are determined from the five recorded data points surrounding the correlation peak using a nonlinear curve fitting algorithm (Appendix A). This second approach gives optimal accuracy, but could not be implemented at the required data rate using the available hardware.

In between these two extremes, there exist a number of other approaches representing a compromise between accuracy and computational complexity. We used linear least squares to fit the five data points to a quadratic,

$$\mathcal{R}_{xy}(t) = A_q \left[1 - \left(\frac{t - t_o}{B} \right)^2 \right], \tag{3.10}$$

where $2B$ is the width of the peak at its base, A_q the amplitude and t_o the location (Appendix A).

3.2.5 Velocity and Vorticity Evaluation

The second computational pass converts data files into time series of amplitude, travel time, path-averaged velocity and relative vorticity. Velocity is obtained using reciprocal travel time difference. The travel time from point $P1$ to $P2$ is

$$t_{12} = \frac{\ell_{12}}{\tilde{c}_{12} + \tilde{u}_{12}}, \tag{3.11}$$

where $\tilde{c}_{12}$ and $\tilde{u}_{12}$ are the path-averaged sound speed and fluid velocity respectively, along the ray joining $P1$ with $P2$, and ℓ_{12} is the range. Assuming that $\tilde{c}_{12}$, $\tilde{u}_{12}$ and ℓ_{12} remain momentarily unchanged, the travel time in the reciprocal direction is

$$t_{21} = \frac{\ell_{12}}{\tilde{c}_{12} - \tilde{u}_{12}}, \tag{3.12}$$

and the travel time difference is

$$\Delta t_{12} = t_{21} - t_{12} = \frac{2\,\tilde{u}_{12}\,\ell_{12}}{(\tilde{c}_{12})^2 - (\tilde{u}_{12})^2} \approx \frac{2\,\tilde{u}_{12}\,\ell_{12}}{(\tilde{c}_{12})^2}, \tag{3.13}$$

since $u \ll c$. The sum of the reciprocal travel times $\Sigma t_{12} = t_{12} + t_{21}$ is used to eliminate either ℓ_{12} or c_{12} from (3.13) and solve for the path-averaged velocity,

$$\tilde{u}_{12} = \frac{\Delta t_{12}}{\Sigma t_{12}}\,\tilde{c}_{12} \approx \frac{2\Delta t_{12}}{(\Sigma t_{12})^2}\,\ell_{12}. \tag{3.14}$$

Vorticity is obtained using the method proposed by Rossby [67]. The line integral of fluid motion between points $P1$ and $P2$ can, under the assumptions made above, be written as

$$\int_{P1}^{P2} \mathrm{u} \cdot \mathrm{ds} = \tilde{u}_{12}\,\ell_{12} = \frac{(\tilde{c}_{12})^2}{2}\,\Delta t_{12}, \tag{3.15}$$

where u is the velocity vector and s is a unit vector along the acoustic propagation path. Therefore, the circulation around triangle $P1\,P2\,P3$ is

$$\begin{aligned}\Gamma &= \oint \mathbf{u}\cdot d\mathbf{s} = \tilde{u}_{12}\,\ell_{12} + \tilde{u}_{23}\,\ell_{23} + \tilde{u}_{31}\,\ell_{31} \\ &= \frac{(\tilde{c}_{12})^2}{2}\Delta t_{12} + \frac{(\tilde{c}_{23})^2}{2}\Delta t_{23} + \frac{(\tilde{c}_{31})^2}{2}\Delta t_{31}. \qquad (3.16)\end{aligned}$$

From Stoke's theorem, the circulation is equivalent to the surface integral of the normal component of vorticity. If the triangle lies on a horizontal plane, the circulation is

$$\oint \mathbf{u}\cdot d\mathbf{s} = \iint (\nabla\times\mathbf{u})_z\,dx\,dy = \zeta_z A_T, \qquad (3.17)$$

the product of the average vertical component of relative vorticity ζ_z, with the area of the triangle A_T. Assuming that $\tilde{c}_{12}\approx\tilde{c}_{23}\approx\tilde{c}_{31}\approx\tilde{c}$, (3.16) and (3.17) yield

$$\zeta_z \approx \frac{\tilde{c}^2}{2A_T}(\Delta t_{12}+\Delta t_{23}+\Delta t_{31}). \qquad (3.18)$$

A consequence of the above equation is that for a desired resolution in vorticity, the travel time difference must be measured with a precision that is inversely proportional to the square of the dimension of the acoustic array.

Chapter 4

Observations

4.1 Field Trip Summary

We deployed the acoustic system at the CEAREX oceanography ice camp during March and April 1989. The six underwater units were deployed at two separate depths at the vertices of an equilateral triangle with sides of length 201, 205 and 211 m. The acoustic array was laid out beneath the floe so as to span both multiyear and young ice, thus providing contrasting turbulence regimes (Fig. 3.2). Each underwater unit comprised two transducers and accompanying electronics mounted on a heavy iron bar laid out horizontally beneath the ice. The nominal separation between the paired transducers was 65 cm (Fig. 3.3). Multiconductor cables were laid out to connect the sonars with surface instrumentation contained in a centrally located hut.

The deployment of the first six sonars at a depth of 20.4 m beneath the sea surface (18 m from the ice bottom) was completed on March 29. Data collected in this configuration was monitored and analyzed during the next three days in order to ensure proper operation of the apparatus. Although, the analysis and physical interpretation of the data could not be done in the field, a personal computer with a custom interface card was used to monitor and validate the data during operation of the acoustic instrumentation.

The next six sonars were deployed 10.4 m beneath the surface (8 m from the

ice bottom) on April 2, 3 and 4 respectively. On April 14 and 15, three pairs of transducers were raised to 8 m and the other three lowered to 85 m in order to study processes near the top and the bottom of the mixed layer. The 85 m data will not be discussed in this thesis because travel time measurements at that depth are not reliable due to instrumentation problems during the experiment. Specifically, the sonar clock signals were contaminated by electrical crosstalk during transmission. To get around this problem, we have relied on the phase of the acoustic arrivals to track changes in travel time. This works reasonably well for the shallow moorings because the distance between transmitting and receiving hydrophones did not usually vary by more than half a wavelength between two consecutive transmissions. This was not the case for the 85 m depth acoustic data, for which it was not possible to resolve the 360° phase ambiguity.

The sonars and the transducers were recovered on April 22 and 23. During the period from March 27 to April 23, nearly 350 GB of data were recorded on 71 VCR tapes.

4.2 Noise Analysis

In this section, we establish the sensitivity of the instrument both for phase and amplitude measurements. First a theoretical lower bound for the ambient noise level is established. Then the acoustic power projected into the water and received by the hydrophones is estimated. Finally, the signal to noise performance of the instrument and its effect on phase and amplitude measurements is discussed.

4.2.1 Thermal Noise

High frequency ambient noise beneath arctic floes is due to thermal tension cracking of the ice and to strong winds. These processes produce a noise spectrum which decays rapidly for frequencies above 6 kHz [17]. A theoretical limit in the detection of underwater acoustic signals at higher frequencies is imposed by thermal noise. Mellen [18] derived the thermal noise spectrum from classical statistical mechanics.

The mean square noise pressure $\langle P^2 \rangle$ in a frequency band β is

$$\langle P^2 \rangle = \int_{f_c-\beta/2}^{f_c+\beta/2} KT\rho c \frac{4\pi f^2}{c^2}\, df \tag{4.1}$$

where f is the frequency, K is Boltzmann's constant, T is the absolute temperature, ρ is the density and c is the speed of sound. Given

$$\begin{aligned} f_c &= 132.3 \text{ kHz} \\ T &= -1.83\ ^\circ\text{C} = 271.32\ ^\circ\text{K} \\ K &= 1.3806 \times 10^{-23} \text{ J/}^\circ\text{K} \\ \rho &= 1028.2 \text{ kg/m}^3 \\ c &= 1439.8 \text{ m/s} \\ \beta &= 22 \text{ kHz} \end{aligned}$$

we obtain a thermal noise level $L_n = 71$ dB//μPa.

4.2.2 Transmitted and Received Power

Due to severe crosstalk problems between the transmitting and receiving electronics, we were forced to limit the transmitted acoustic power to very small values during the experiment. Typically, the magnitude of the transmitted analog signal was measured to be 5 V at the surface. Taking into account cable losses and the matching transformer and inductor we estimate the voltage at the input of the transducers to have been 8 V. The transmitting response of the transducers at 132 kHz is roughly 140 dB//μPa/V @ 1 m. Therefore, the transmitted power was 158 dB//μPa @ 1 m (only 50 mW). The spreading loss $20 \log \ell$, where $\ell = 200$ m is the length of the sonic path, was 46 dB. For the oceanographic conditions prevalent at the time of the measurements, the attenuation coefficient is 41 dB/km. The acoustic power at reception is typically 104 dB//μPa. The receiving response of the transducers at 132 kHz is of order -165 dB//V/μPa and the programmable gain amplifier on the digitization boards was typically set at 56 dB, to obtain a signal amplitude of order 0.5 V at the input of the analog-to-digital converter. These values are tabulated in Table 4.1.

Parameter	Value
Surface transmit voltage (V)	5
Transducer transmit voltage (V)	8
Transmitting response (dB//μPa/V @ 1 m)	140
Transmit power (dB//μPa)	158
Transmit power (mW)	50
Sound speed c (m/s)	1440
Acoustic wavelength λ_a (cm)	1.09
Receiver separation r (cm)	65
Acoustic path length ℓ (m)	201
Spreading loss (dB)	46
Attenuation coefficient (dB/km)	41
Receive power (dB//μPa)	104
Receiving response (dB//V/μPa)	-165
PGA gain (dB)	56
A/D signal level (V)	0.5
Thermal noise level L_n (dB//μPa)	71
System noise level (dB//μPa)	103
Total signal processing gain (dB)	27
Signal to noise ratio SNR (dB)	28
Root mean square phase noise (°)	2.3
Root mean square noise σ_t (ns)	48

Table 4.1: Noise and acoustic parameters for typical transmit-receive sonar pair.

4.2.3 Signal to Noise Ratio

Typical signal-to-noise-ratio for a transmit-receive pair of transducers was measured to be of order 28 dB during the experiment. This corresponds to an rms phase noise of 2.3°. Since the signal level is known, we deduce that the operating noise at the receiving sonar is equivalent to 103 dB//μPa of ambient sound. This value is consistent with measurements made in the lab prior to the experiment and is 32 dB greater than the predicted thermal noise level calculated in Section 4.2.1. Therefore, sonar components and their interaction impose a limit on acoustic detection and not ambient sound. The transmit (Tx) and receive (Rx) characteristics of each sonar vary, resulting in different signal-to-noise-ratio (SNR)

Tx	Rx	SNR (dB)	σ_t (ns)	σ_v (mm/s)
2	7	17	167	1.8
7	2	27	53	
2	12	13	263	2.8
12	2	28	48	
10	7	20	118	1.6
7	10	22	94	
10	12	13	255	2.8
12	10	22	92	
2	6	20	114	1.3
6	2	26	60	
10	6	26	60	1.0
6	10	23	82	
7	6	27	54	1.4
6	7	20	125	
12	6	26	58	3.2
6	12	12	304	

Table 4.2: Signal to noise ratio and rms noise at the 20-m depth.

for each combination. The measured SNR for each Tx-Rx pair are tabulated in Table 4.2.

4.2.4 Velocity and Vorticity Noise Level

The instrument noise for each transducer is independent from noise at other locations; therefore, the variance of the noise for travel-time difference is equal to the sum of the mean squared noise of the two reciprocal transmissions. Using this assumption and (3.14), it is possible to estimate the rms noise for velocity measurements, σ_v; the results of these calculations are tabulated in Table 4.2. It is also possible to estimate the rms vorticity noise using (3.18) with $A_T = 18327$ m^2. For example, the rms noise for relative vorticity calculated around transducers 2, 6 and 7 is 1.5×10^{-5} s^{-1}, approximately 10% of the planetary vorticity $f = 1.45\times10^{-4}$ s^{-1} at latitude 83°N. By averaging over several samples, the rms noise level can be re-

duced.

4.3 Sources of Error

4.3.1 Temporal Variability

For the derivation of (3.14) and (3.18), it was assumed that sound speed and flow field, along the acoustic propagation paths, do not change during the time required for reciprocal transmission. Although this assumption is only an approximation, we find that in the turbulent boundary layer beneath the ice camp, the effect of spatial and temporal variance on measurement accuracy, was small compared to other sources of error.

4.3.2 Error Due to Shear

In the presence of shear, an error is caused by lack of reciprocity of the acoustic paths. This effect causes the familiar "carrying" of sound by surface wind. If the wind blows from the source towards the listener, the surface friction establishes a shear which bends the acoustic rays downward, thus forming a sound channel; the effect is particularly noticeable over a smooth surface such as calm water where there is little scattering as the sound bounces off the water. However, a wind blowing against the propagation direction deflects the rays upward and the sound is "lost". It can be shown that for vertical shear σ, range ℓ and sound speed c, the sum of the reciprocal travel times is decreased by $\sigma^2\ell^3/24c^3$, and the maximum separation between the reciprocal rays is $\sigma\ell^2/4c$ (Appendix B). For $\sigma = 10^{-3}$ s^{-1}, $\ell = 200$ m and $c = 1440$ m/s, the error in the total travel time (≈ 112 ps) and the maximum separation between the reciprocal acoustic paths (≈ 7 mm) are insignificant.

4.3.3 Alignment of the Array

A significant error may be caused by vertical shear if the array is not horizontal. Consider a shear induced horizontal vorticity component

$$\zeta_x = \frac{\partial w}{\partial y} - \frac{\partial v}{\partial z} \tag{4.2}$$

in an orthogonal coordinate system $x\,y\,z$. In a rotated coordinate system $x'\,y'\,z'$, there is an apparent vertical vorticity component

$$\zeta_{z'} = -\zeta_x \sin\theta \tag{4.3}$$

where θ is the angle between axis z and z'. For example, a typical vertical shear $\partial v/\partial z = 10^{-3}\ \mathrm{s}^{-1}$ will cause an apparent vertical vorticity $\zeta_{z'} = 10^{-6}\ \mathrm{s}^{-1}$, less than 1% of the planetary vorticity, for an inclination $\theta = 3'30''$. This angle is equivalent to a 20 cm depth misalignment of the array over 200 m. The uncertainty in the depth of the moorings during deployment was less than ± 2 cm. Depth misalignment may also have occurred during the experiment because of the swinging motion of the moorings. The amplitude of the relative mooring motion at 20 m depth was less than 20 cm. This corresponds to a worst case relative change in depth of 1 mm. Therefore, the expected error due to misalignment of the acoustic elements is less than 0.1% of the planetary vorticity.

4.3.4 Multipath Interference

The accuracy of the acoustic measurements is limited by interference from the multipath environment. During the experiment we found that the acoustic signal reflected by the ice was of comparable strength to the direct path. Under the smooth ice of the newly refrozen lead, the reflected path was at times 20 to 30% stronger than the direct path. The smoothly varying surface of the underside of the ice, can under certain circumstances behave like a large concave mirror that focuses acoustic energy. Mooring motions bring the transducers in and out of

acoustic focus relative to each other. As discussed in Section 3.2.1, interference from the correlation sidelobes of the ice-reflected acoustic arrivals establish an upper bound on the signal to noise ratio that can be achieved by the acoustic system.

4.3.5 Mooring Motion

Mooring motions during the measurement time frame introduce an error, δt, in reciprocal travel time difference. The magnitude of this error as a function of angular frequency, $\omega = 2\pi f$, is bounded by

$$\delta t(\omega) \leq \frac{\omega M(\omega) \tau_{tr}}{c}, \tag{4.4}$$

where $M(\omega)$ is the amplitude of the relative mooring motion and τ_{tr} is the delay between transmission and reception of a reciprocal pair of pulses. From (4.4), it follows that the error introduced by mooring motion has zero average and is limited to the high frequency end of the spectrum. For this reason, the moorings were designed so as to minimize strumming and high frequency oscillations.

4.4 Travel Time

Acoustic travel time between transducers is measured to within a small fraction of the carrier period ($\tau_a = 7.56\ \mu$s) by first interpolating the location of the transmit and receive peaks to resolve the phase ambiguity and subsequently using phase to provide high resolution measurements. An unfiltered twenty minute time series of travel time between two transducers located at a depth of 8 m is shown in Fig. 4.1. The average value of 146.83 ms indicates a mean separation of 211 m. The oscillations are principally caused by relative mooring motion resulting in displacements of up to 4 cm in this short data section.

The autospectral density function of acoustic travel time for an eight hour time-series, which includes the section of data of Fig. 4.1, is shown in Fig. 4.2. At high

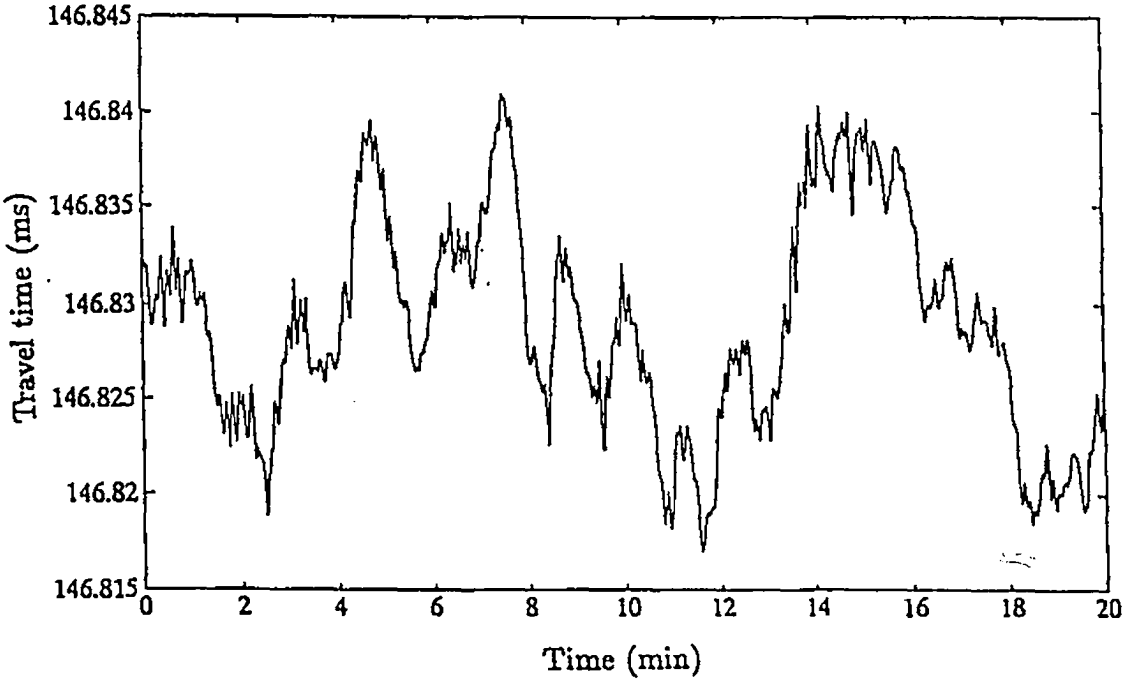

Figure 4.1: Acoustic travel time between two transducers at the 8.4-m depth, separated by 211 m in a direction of 344° T, for data collected in the boundary layer on April 18, 1989. The oscillations are a result of relative mooring motion and correspond to displacements of up to 4 cm.

frequency, there is a white noise floor at a level of 7×10^{-3} $\mu s^2/Hz$. We attribute this noise floor to multipath interference with line-of-sight reception. For decreasing frequency, the spectral density sharply rises to 1.5 $\mu s^2/Hz$ at $\omega_r/2\pi = 0.133$ Hz which is the mechanical resonance frequency of the 8-m moorings. At still lower frequency, the spectrum increases more gradually.

Relative mooring motion can be determined by analyzing the travel time of acoustic pulses. To a first approximation, each mooring behaves as a damped pendulum oscillator with a forcing term introduced by currents beneath the ice. For small displacements, and linear damping, the horizontal motion of a forced pendulum, is controlled by,

$$\frac{d^2x}{dt^2} + 2\gamma\frac{dx}{dt} + \omega_o^2 x = \frac{F(\omega_f)}{m}\cos\omega_f t, \tag{4.5}$$

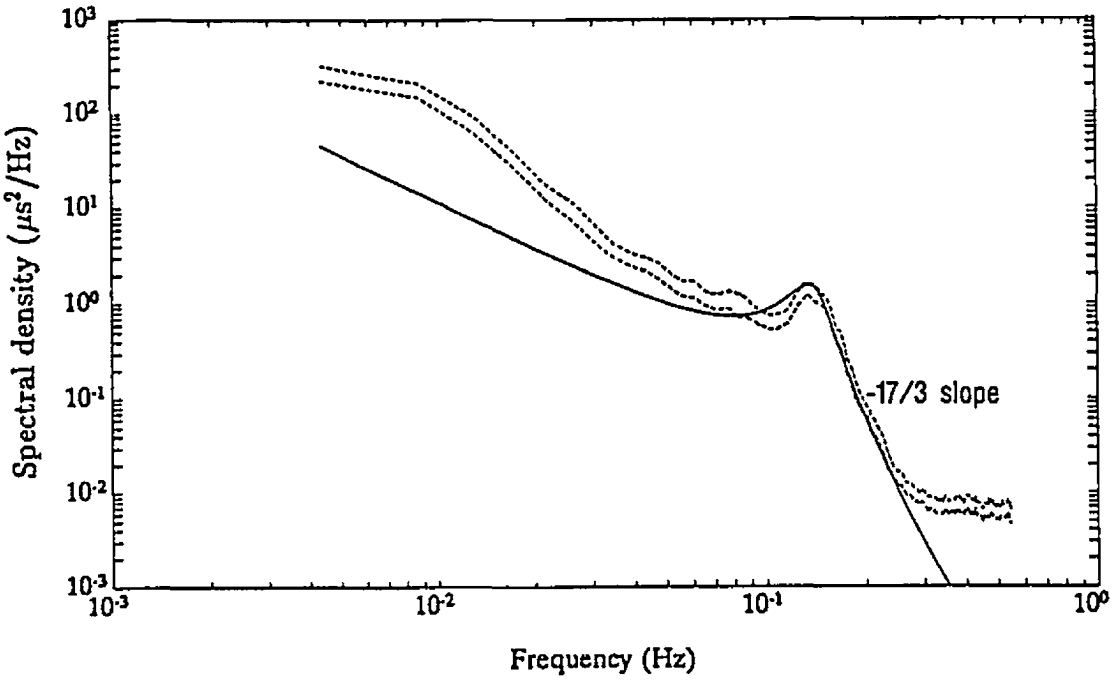

Figure 4.2: Autospectral density function of acoustic travel time at the 8.4-m depth. The data consist of an eight hour time series sampled at 1.1 Hz on April 18, 1989. The dashed lines enclose the 95% confidence interval of the spectrum. The solid line is a theoretical prediction of mooring motion.

where γ is the damping constant, $\omega_o = (g/z)^{1/2}$ is the natural angular frequency, z the deployment depth below the bottom of the ice, m the mass, ω_f the forcing frequency, and $F(\omega_f)$ the forcing term [2]. The flow field provides forcing, and the system oscillates with amplitude

$$M(\omega_f) = \frac{F(\omega_f)/m}{\sqrt{(\omega_f^2 - \omega_o^2)^2 + 4\gamma^2\omega_f^2}}, \tag{4.6}$$

which is equal to $F(\omega_f)/m\omega_o^2$ at low frequencies, has a local maximum at the mechanical resonance frequency $w_r = \sqrt{\omega_o^2 - 2\gamma^2}$, and varies as $F(\omega_f)/m\omega_f^2$ at high frequencies.

In addition to simple swinging, the moorings have a rotational mode of oscillation (Fig. 3.3). The natural frequency of rotation decreases down to a minimum of

$\omega_o = (g/z)^{1/2}$, as the weights are moved towards the edges of the suspended steel bars. We neglect this mode of oscillation for two reasons. First, the transducers are centered on the iron bar; therefore, their position relative to other moorings depends primarily on swinging rather than rotation. Second, most of the weight is concentrated at the edges of the steel bars; therefore, the natural swinging and rotational frequency are almost equal and their spectral signatures on one-way travel time are indistinguishable.

We assume that the mooring motions of the transmitting and receiving transducers are statistically independent, which is certainly true at sufficiently high frequency. Therefore, the spectral contributions to travel time from the motion of the two moorings add up algebraically. The solid line in Fig. 4.2 is a theoretical prediction of the spectrum, obtained using (4.6) and a Kolmogorov inertial subrange (Section 5.2.1) forcing term $F^2(\omega_f) = F_o^2 \omega_f^{-5/3}$. The natural frequency of oscillation ω_o, and the forcing constant F_o are chosen to optimize the fit between data and theory at high frequency. The model successfully predicts the steep $-17/3$ spectral slope at high frequency and the presence of a local maximum in the spectrum due to mechanical resonance of the moorings.

At low frequency, the inertial subrange approximation does not hold and we expect a spectral slope that is less steep than -5/3. Instead, the model underestimates the spectral intensity. In addition, the natural frequency used to fit the model to the data, $\omega_o/2\pi = 0.14$ Hz, is lower than $(g/z)^{1/2} = 0.17$ Hz, the expected frequency based on deployment depth. We attribute these discrepancies to the nonlinear dependence between the forcing and damping terms, and the flow field.

4.5 Path-Averaged Current

4.5.1 Accuracy

Path-averaged current measurements are based on travel time difference of reciprocal acoustic propagation. Therefore, the accuracy of the current measurement is ultimately limited by the precision with which travel time can be measured in both directions. Another factor limiting the accuracy of the measurements is relative mooring motion as discussed in Section 4.3.5.

Fig. 4.3 displays the autospectral density function of path-averaged velocity measurements obtained at 8 m depth for the same eight hour period as Fig. 4.3. At high frequency, there is a white noise floor at a level of 5×10^{-3} $(\mathrm{cm/s})^2/\mathrm{Hz}$, which corresponds to the combined noise floor of the two reciprocal travel time measurements. Near the mechanical resonance frequency of the moorings, the error introduced by relative motion during a reciprocal transmission dominates the velocity measurements. The autospectral density of the error due to mooring motion is estimated using (4.4) and drawn as a solid line on the figure. Clearly, the peak in the spectral density at 0.133 Hz is caused by relative mooring motion. For frequencies lower than 0.07 Hz, the error caused by mooring motion drops below the spectral level of path-averaged currents.

An alternative analysis of mooring motion effects is based on the coherence function between one-way travel time and velocity, shown in Fig. 4.4. The coherence of the two signals is high in the neighborhood of mechanical resonance; at frequencies below 0.07 Hz, low coherence confirms that mooring motion is not an important factor. All velocity and vorticity data is lowpass filtered to remove the error due to mooring motion. Assuming Gaussian white noise with a spectral density of 5×10^{-3} $(\mathrm{cm/s})^2/\mathrm{Hz}$, equivalent to that observed at high frequency, the rms noise level is less than 0.1 mm/s at a filtered sampling rate of once per minute.

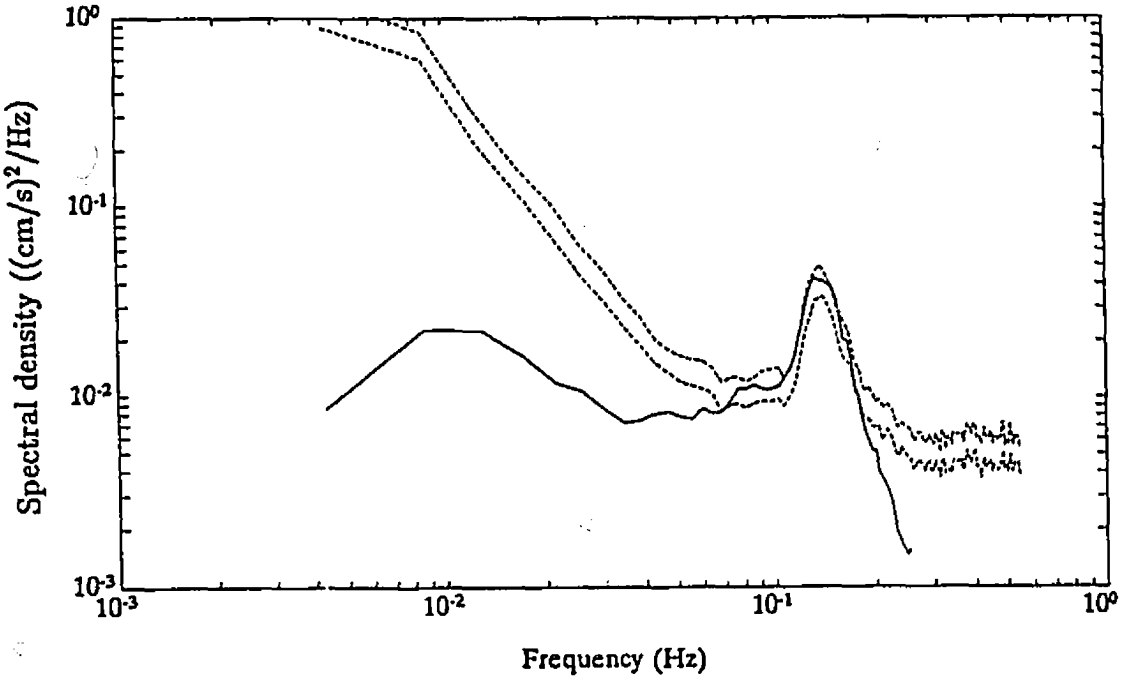

Figure 4.3: Autospectral density function of path-averaged velocity measurements at the 8.4-m depth, for the same eight hour period as Fig. 4.2. The dashed lines enclose the 95% confidence interval of the spectrum. The solid line is an estimate of error due to relative mooring motion during a reciprocal transmission.

4.5.2 Spatial Filtering

Each acoustic path acts as a path-averaging spatial filter which damps small scale fluctuations and focuses on low wavenumbers. The path-averaged velocity along baseline ℓ is

$$\tilde{\mathrm{u}}(\mathrm{x},t) = \frac{1}{\ell}\int_{-\ell/2}^{\ell/2} \mathrm{u}(\mathrm{x}+\mathrm{s},t)\,ds, \tag{4.7}$$

where $\mathbf{s}$ is a vector parallel to ℓ with magnitude s. For events coherent along the acoustic propagation path, the spatial-filter response of the path-averaging current meter is

$$H(\mathrm{k},\ell) = \frac{\tilde{\mathrm{u}}(\mathrm{k},t)}{\mathrm{u}(\mathrm{k},t)} = \frac{\sin(\mathrm{k}\cdot\ell/2)}{\mathrm{k}\cdot\ell/2}, \tag{4.8}$$

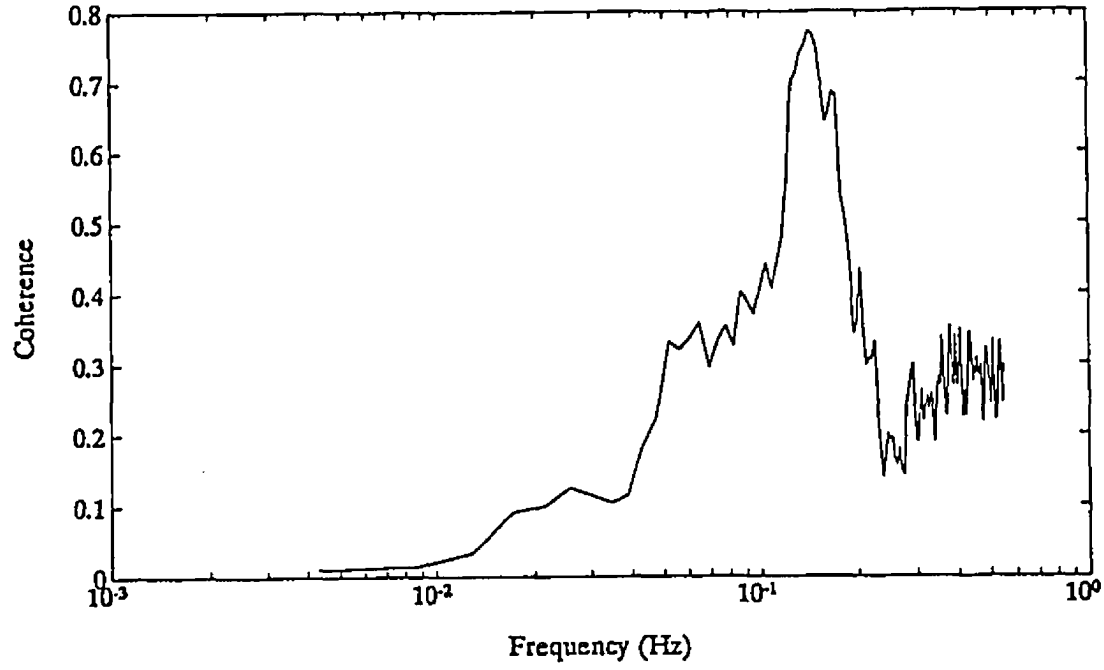

Figure 4.4: Coherence function between one-way travel time and velocity at 8.4-m depth, for the same eight hour period as that of Fig. 4.2.

where $\tilde{\mathrm{u}}(\mathrm{k}, t)$ and $\mathrm{u}(\mathrm{k}, t)$ are the spatial Fourier transforms of $\tilde{\mathrm{u}}(\mathrm{x}, t)$ and $\mathrm{u}(\mathrm{x}, t)$, respectively, that is

$$\mathrm{u}(\mathrm{x}) = \int_{-\infty}^{\infty} \exp(i\mathrm{k} \cdot \mathrm{x})\mathrm{u}(\mathrm{k})\, d\mathrm{k}, \tag{4.9}$$

and

$$\mathrm{u}(\mathrm{k}) = \frac{1}{(2\pi)^3} \int_{-\infty}^{\infty} \exp(-i\mathrm{k} \cdot \mathrm{x})\mathrm{u}(\mathrm{x})\, d\mathrm{x}. \tag{4.10}$$

The length of the measuring baseline during the arctic experiment was $\ell = 200$ m, therefore the acoustical current meter was a lowpass spatial filter with cutoff wavelength $\lambda_o = 450$ m and zero phase shift in the passband.

4.5.3 Directional Filtering

Each acoustic path also acts as a directional filter with preference given to velocity fluctuations parallel to the measuring baseline. Consider a flow field

$$\mathbf{U}(\mathbf{x},t) = \overline{\mathbf{U}} + \mathbf{u}(\mathbf{x},t), \tag{4.11}$$

where $\overline{\mathbf{U}}$ is the mean ice-relative velocity vector, and $\mathbf{u}(\mathbf{x},t)$ represents fluctuations about the mean. The velocity measured by the acoustical current meter is

$$\tilde{U}_\ell(\mathbf{x},t) = [\overline{\mathbf{U}} + \tilde{\mathbf{u}}(\mathbf{x},t)] \cdot \boldsymbol{\ell}/\ell, \tag{4.12}$$

where $\tilde{\mathbf{u}}(\mathbf{x},t)$ is as defined by (4.7), and $\boldsymbol{\ell}/\ell$ is a unit vector parallel to the measuring baseline.

4.5.4 Doppler Shift

The motion of the instrument relative to the medium that supports the disturbance introduces a Doppler-frequency shift in the measurement. Consider the sinusoidal disturbance

$$\mathbf{u}(\mathbf{y},t) = \mathbf{u}_o \cos(\mathbf{k}\cdot\mathbf{y} - \omega t), \tag{4.13}$$

riding the ice-relative mean velocity vector $\overline{\mathbf{U}}$. Here, $\mathbf{y}$ is a Cartesian coordinate system moving with velocity $\overline{\mathbf{U}}$ relative to the ice, $\mathbf{u}_o$ is the vector amplitude of the wave, $\mathbf{k}$ is the wave vector with magnitude $k = 2\pi/\lambda$, and $\omega = 2\pi f$ is the radial frequency of the wave. The velocity measured by an instrument deployed from the ice is

$$\mathbf{U}(\mathbf{x},t) = \overline{\mathbf{U}} + \mathbf{u}_o \cos[\mathbf{k}\cdot\mathbf{x} - (\omega + \mathbf{k}\cdot\overline{\mathbf{U}})t], \tag{4.14}$$

where $\mathbf{x}$ is a Cartesian coordinate system fixed with respect to the measuring platform and $\mathbf{k}\cdot\overline{\mathbf{U}}$ is the Doppler-frequency shift. This frequency shift is negligible when

$$\frac{\mathbf{k}\cdot\overline{\mathbf{U}}}{k} \ll \frac{\omega}{k}, \tag{4.15}$$

i.e. when the mean ice-relative velocity parallel to the wave vector is negligible compared to the phase speed of the wave.

4.5.5 Comparison with Point Measurements

McPhee [45] reports that 7 m below the ice, the significant turbulent eddies for heat and momentum transfer in the boundary layer have typical horizontal extent of order 10-20 m. Therefore, the acoustic current meter averages over several eddies with each sample and attenuates velocity fluctuations due to turbulence. Fig. 4.5 compares path-averaged current measurements with point measurements made by M. G. McPhee (1990, personal communication), using a mechanical current meter located in the middle of the acoustic array. The solid line represents velocity data from the acoustic path oriented 344° T, low pass filtered at 0.5 min^{-1}. The dots are one minute averages from the mechanical current meter. The scatter of the point measurements is a result of the high spatial resolution of the mechanical current meter, which has a sampling wavelength of 20 cm [43], and the turbulent nature of the ice-water boundary layer. For periods greater than 20 min, the frequency response function between the two types of measurement has constant phase factor ($\approx 0°$), and the coherence function is relatively high (> 0.5).

Each side of the acoustic array preferentially detects internal waves whose wavevectors are aligned with the axis of acoustic propagation. Kinetic energy from internal waves that are not aligned with the acoustic path is attenuated and aliased to lower frequencies. A rough theoretical estimate of the transfer function between point and line-averaged measurements is obtained by assuming the mean flow is negligible compared to the dispersion velocity of internal waves and that the internal waves propagate parallel to the acoustic path.

The solid line in Fig. 4.6 is the observed gain factor of the frequency response function between path-averaged and point measurements. The dotted line represents a theoretical prediction based on the spatial resolution of the acoustic array

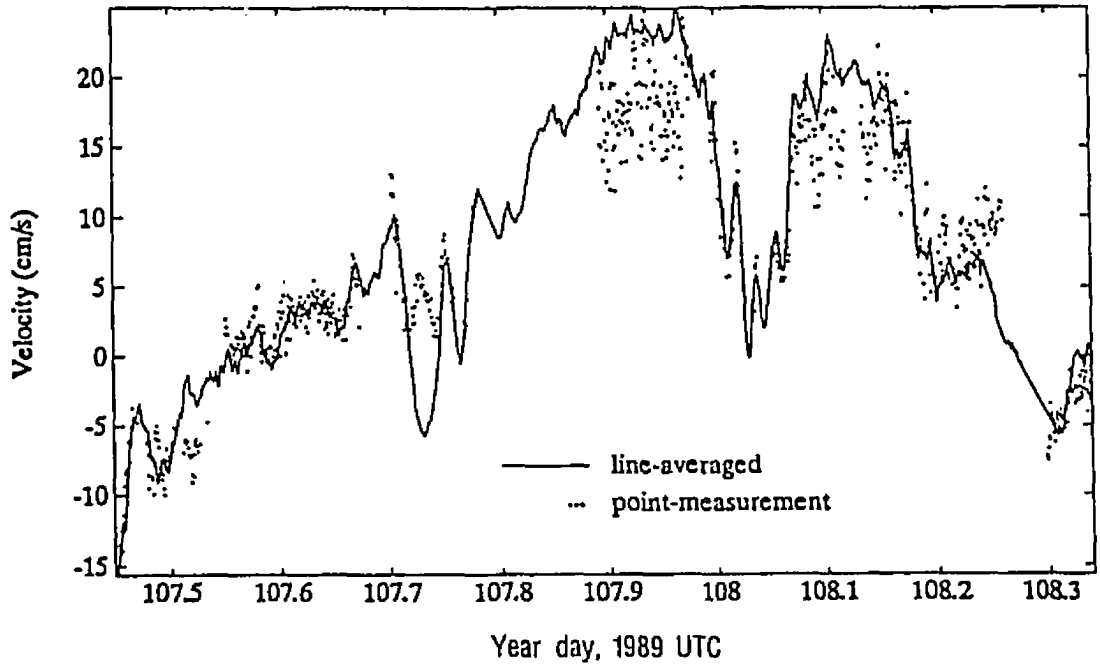

Figure 4.5: Comparison between path-averaged and point current measurements. The solid line is a velocity time series obtained with the acoustic current meter at the 8.4-m depth, 344° T, on April 17 and 18 (day 107 and 108), 1989. A 0.0083 Hz lowpass filter has been applied to the data. The dots are one minute averages from a mechanical current meter which has a spatial resolution of 20 cm; the current meter was located in the center of the acoustic array at a depth of 10.4 m.

given by (4.8) and a two layer fluid internal wave dispersion relation,

$$\omega^2 = \left(\frac{\rho_2 - \rho_1}{\rho_2 + \rho_1}\right) gk, \tag{4.16}$$

where $\rho_1 = 1027.47$ kg/m^3, and $\rho_2 = 1027.87$ kg/m^3 are the mean water densities above and below the pycnocline as measured during the experiment [61]. Both the measured and the calculated transfer function show strong attenuation for periods shorter than 20 min. The 2 dB difference between the acoustic current measurements and the fixed point measurements at low frequency results from the less than perfect coherence between the two time series. We attribute this discrepancy to local flow anomalies caused by irregularities in the underside of the ice. At high wavenumbers, equation (4.8) does not hold because we cannot assume

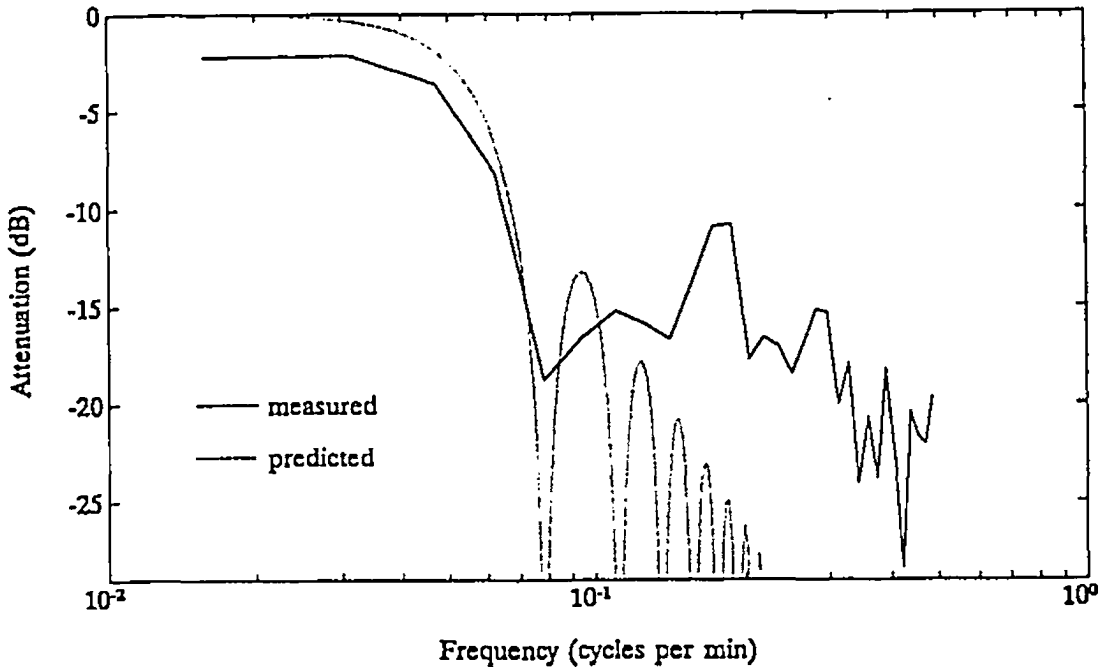

Figure 4.6: Gain factor of frequency response function between the path-averaged and point measurements of Fig. 4.5. The dotted line is a theoretical prediction based on the spatial resolution of the acoustic array and a two layer fluid internal wave dispersion relation.

coherence along the entire acoustic path, as is further discussed in Chapter 5.

4.6 Vorticity

The vertical component of relative vorticity at internal wave length scales is difficult to measure with conventional instrumentation, and we are not aware of other successful attempts to measure this parameter in the boundary layer beneath ice. As discussed earlier, the average vorticity inside the triangle spanned by the acoustic array is readily obtained from reciprocal travel time measurements. Based on the accuracy of current measurements, the rms noise of the vorticity signal averaged over one minute is less than 1% of the planetary vorticity. Examples of vorticity time series and spectral density functions can be found on Figs. 8.5, 8.6d and 8.9 in Chapter 8.

Chapter 5

Reciprocal Travel-Time Scintillation Analysis

5.1 Introduction

In Chapter 4, we determined that the power spectrum of the integrated velocity measurements is dominated by multipath interference and mooring motion for periods shorter than 20 s. For periods longer than 20 min, the passage of internal waves in stratified water underlying the mixed layer dominates the spectrum as discussed in Section 4.5.5, and again in Chapter 8. The aim of the present chapter is to explain the observed high frequency velocity fluctuations which are neither the result of internal waves nor of measurement error, and which were tentatively attributed to the advection and evolution of turbulent velocity fine structure. Existing theory needs to be extended before it is useful in this context. It will be shown that line-averaged velocity measurements can provide statistical information about the velocity fine structure of the intervening fluid, even when the measuring baseline is many times longer than the size of the turbulent eddies.

Turbulence in the ocean is usually measured with instruments that have a high degree of spatial resolution and can therefore sense individual turbulent eddies. But, for most oceanographic studies, the statistical description of a fluid is more important than information about the behaviour of each eddy sensed by the instrument. Of course, Taylor's frozen field hypothesis (Section 5.2.4) can be used to

obtain streamwise correlation functions from high resolution point measurements. The problem is that point measurements may be unduly influenced by local inhomogeneities of the flow and are not always representative of the true areal average.

An alternative strategy involves integral measurements obtained along a baseline that is long compared with the size of the turbulent eddies. This scheme forfeits the observation of individual eddies in favour of a more representative statistical description of the turbulent fluid. A convenient way of obtaining integral measurements of random fields in the ocean is to use acoustic remote sensing techniques. For example, forward scattered sound provides the basis for probing the fine structure along the acoustic path. Sound traveling through a medium having random fluctuations in refractive index suffers perturbations which cause amplitude and phase scintillations on a receiving plane. The interpretation of these scintillations in terms of the structure of the intervening fluid has been the subject of considerable theoretical [23] and experimental effort [21].

Reciprocal acoustical travel time measurement is another remote sensing method which can provide integral measurements of random fields in the ocean. This technique can be used to separate the effects of ocean currents on acoustic propagation from the effects of sound speed structure, and successful measurements have been made along sonic paths ranging from a few centimeters to several hundred kilometers. Ultrasonic current meters based on the principle of reciprocal transmission have often been used to study turbulence in the ocean [34, 69]. However, the sonic pathlengths were always of the same order of magnitude as the smallest turbulent scales to be resolved. Reciprocal acoustic transmission can also be used to study the statistical behaviour of the internal wave field [54], to monitor mesoscale ocean currents [84] and to measure relative vorticity [32]. However, to the best of our knowledge, the technique has never been applied at intermediate pathlengths, *i.e.* hundreds of meters, to probe the velocity fine structure of the intervening fluid. The potential of such measurements remains largely unexplored both theoretically and experimentally.

Kaimal *et al.* [31] discussed the problem of line-averaging in the context of extending the useful range of sonic anemometers in the atmosphere to scales shorter than the acoustic paths. They derived transfer functions that relate measured and ideal one-dimensional power spectra. Here, we add to existing theory in the following ways. Measuring baselines that are several orders of magnitude longer than the typical transducer separation of sonic anemometers, *i.e.* hundreds of meters as opposed to tens of centimeters, are considered. Kaimal *et al.* derived expressions that link horizontal power spectra obtained from two non-parallel sonic paths to the ideal streamwise and cross-stream spectral densities. This is adequate for short and closely spaced sonic paths. A different approach is required for the long pathlengths considered in this paper. The spectral transfer function derived here requires a single acoustic path and is valid for arbitrary angles between the baseline and the mean flow. The asymptotic behaviour of the spectral transfer function is investigated for long measuring baselines; an analytic expression is derived and compared to the numerical solution. In addition to the homogeneous isotropic case considered by Kaimal *et al.* the analysis here is extended to anisotropic and inhomogeneous flows. First, the spectral transfer function for axially symmetric turbulence is derived. Next, it is shown that for sufficiently long measuring baselines, spectral transfer functions are inversely proportional to a dimensionless wavenumber. Finally, the condition of homogeneity is relaxed by considering measurements that span several regions of locally homogeneous turbulence.

Taylor's frozen field hypothesis is often used to relate measured time spectra to spatial correlations. This hypothesis is valid provided the temporal evolution of turbulent fine structure at a fixed location is negligible relative to fluctuations caused by advection of the flow. Wernik *et al.* [79] studied the effects of non frozen turbulent media on one-way propagation experiments. Here, the applicability of the frozen field hypothesis to reciprocal travel time measurements is examined. First, some criteria for applying Taylor's hypothesis to shear flows are established. Then, correction formulas for the spatial and temporal variability of advection

velocity along the measuring baseline are derived. Refractive index variability and turbulent shear along the path cause scattering of the acoustic energy. The effect of this scattering on the accuracy of the measurements is considered. Finally, some experimental data obtained in the arctic boundary layer beneath ice is compared with the theory.

5.2 Theory

5.2.1 Basic Definitions and Assumptions

The statistical description of turbulence is discussed extensively in the literature [30, 42, 4]. Here, we are merely concerned with introducing the concepts and notation necessary to our discussion. Additional background material regarding the statistical description of random fields can also be found in Section 2.1.

We consider the random velocity field $\mathbf{u}(\mathbf{x}, t)$, that has zero mean and is stationary in $\mathbf{x}$ (homogeneous) and t. This field is advected along the x_1-axis of a Cartesian coordinate system, by the mean velocity vector, $\overline{\mathbf{U}}$, so that

$$\mathbf{U}(\mathbf{x}, t) = \overline{\mathbf{U}} + \mathbf{u}(\mathbf{x}, t), \tag{5.1}$$

where the overbar denotes time-averaging. A more complete discussion of this type of decomposition is given in Section 2.1.3. We follow the usual convention of representing vectors in boldface, their magnitude in italics and the individual components by using subscripts. For example, the vector $\mathbf{x}$ has magnitude x and components x_i where $i = 1, 2, 3$.

Fourier-Stieltjes integrals

One would like to have a spectral representation for the random function $\mathbf{u}$, but homogeneity implies that

$$\int_{-\infty}^{\infty} |u_i(\mathbf{x})|\, d\mathbf{x} = \infty, \tag{5.2}$$

i.e. Dirichlet's condition is not satisfied, and no valid Fourier transform exists. To avoid this difficulty, stochastic Fourier-Stieltjes integrals are used to represent the turbulent velocity field,

$$u_i(\mathbf{x},t) = \int_{-\infty}^{\infty} \exp(i\mathbf{k}\cdot\mathbf{x})\, dZ_i(\mathbf{k},t), \tag{5.3}$$

where k is the vector wavenumber. The $Z_i(\mathbf{k},t)$ are random functions with orthogonal increments,

$$\overline{dZ_i(\mathbf{k},t)\, dZ_j^*(\mathbf{k}',t)} = \begin{cases} 0, & \mathbf{k}\neq\mathbf{k}' \\ \varphi_{ij}(\mathbf{k})\, d\mathbf{k}, & \mathbf{k}=\mathbf{k}' \end{cases}, \tag{5.4}$$

where the asterisk indicates complex conjugate and $\varphi_{ij}(\mathbf{k})$ is the spectral density tensor. The correlation tensor, $R_{ij}(\mathbf{r})$, is related to the spectral density tensor by

$$R_{ij}(\mathbf{r}) = \overline{u_i(\mathbf{x},t)u_j(\mathbf{x}+\mathbf{r},t)} = \int_{-\infty}^{\infty} \exp(i\mathbf{k}\cdot\mathbf{r})\varphi_{ij}(\mathbf{k})\, d\mathbf{k} \tag{5.5}$$

and

$$\varphi_{ij}(\mathbf{k}) = \frac{1}{(2\pi)^3}\int_{-\infty}^{\infty} \exp(-i\mathbf{k}\cdot\mathbf{r})R_{ij}(\mathbf{r})\, d\mathbf{r}. \tag{5.6}$$

Three-Dimensional Spectral Density

The three-dimensional spectral density $E(k)$ is the power associated with a particular scale of motion, λ, and is obtained by integrating $\varphi_{ij}(\mathbf{k})$ over a spherical shell of radius $k = 2\pi/\lambda$,

$$E(k) = \frac{1}{2}\oiint_{k_ik_i=k^2} \varphi_{ii}(\mathbf{k})\, ds, \tag{5.7}$$

so that

$$\int_0^{\infty} E(k)\, dk = \frac{1}{2}\int_{-\infty} \varphi_{ii}(\mathbf{k})\, d\mathbf{k} = \frac{1}{2}R_{ii}(0) = \frac{1}{2}\overline{u_iu_i}, \tag{5.8}$$

where the repeated indices imply summation over i.

Practical Measurements

In practice, $R_{ij}(\mathrm{r})$, $\varphi_{ij}(\mathrm{k})$, and $E(k)$, are difficult to observe directly. Actual measurements, and the use of Taylor's frozen field hypothesis yield streamwise correlation functions,

$$R_{ij}(r_1) = \overline{u_i(\mathrm{x},t)u_j(\mathrm{x}+r_1,t)} = \int_{-\infty}^{\infty} \exp(ik_1 r_1) F_{ij}(k_1)\, dk_1 \tag{5.9}$$

and the one-dimensional spectral density tensor

$$F_{ij}(k_1) = \frac{1}{2\pi} \int_{-\infty}^{\infty} \exp(-ik_1 r_1) R_{ij}(r_1)\, dr_1 = \iint_{-\infty}^{\infty} \varphi_{ij}(\mathrm{k})\, dk_2\, dk_3, \tag{5.10}$$

so that

$$\int_0^{\infty} F_{ij}(k_1)\, dk_1 = \frac{1}{2} \int_{-\infty}^{\infty} \varphi_{ij}(\mathrm{k})\, d\mathrm{k} = \frac{1}{2} R_{ij}(0) = \frac{1}{2} \overline{u_i u_j}. \tag{5.11}$$

The definition of $F_{ij}(k_1)$ is not uniform in the literature. The form above corresponds to the two-sided spectral density discussed in Section 2.1.2, and is commonly used for theoretical work [4, 42, 31]. For experimental work [27, 30, 24], $F_{ij}(k_1)$ is often defined without the factor 1/2 of (5.11), and corresponds to the one-sided spectral density function discussed in Section 2.1.2.

Power Law Form of the Spectrum

In the wavenumber range of interest, we will assume that $E(k)$ has a power law dependence on k,

$$E(k) = Ck^{-p}. \tag{5.12}$$

Isotropic Turbulence

For isotropic turbulence,

$$\overline{u_i u_j} = \overline{u_1^2}\delta_{ij}, \tag{5.13}$$

and the spectral density tensor is related to the three-dimensional spectrum by

$$\varphi_{ij}(\mathrm{k}) = \frac{E(k)}{4\pi k^4}(k^2\delta_{ij} - k_i k_j). \tag{5.14}$$

Kolmogorov Inertial Subrange

Kolmogorov postulated that for stationary turbulence at sufficiently high Reynolds' number there exists a range of wavenumbers, between energy containing and dissipation ranges, in which the turbulence is locally isotropic and the three-dimensional spectral density, $E(k)$, depends only upon wavenumber k and the dissipation rate ϵ. Dimensional arguments lead to the conclusion that in this inertial subrange

$$E(k) = A\epsilon^{2/3}k^{-5/3}. \tag{5.15}$$

Empirical evidence suggests an approximate value for the Kolmogorov constant of $A \approx 1.5$ [30]. Although most turbulence is not isotropic [72], (5.15) is a useful approximation for estimating energy dissipation (Section 5.3.4).

5.2.2 Line-Averaging

Consider velocity measurements integrated along baseline ℓ. Without loss of generality, we assume that this baseline lies in the x_1-x_2 plane at angle θ from the mean velocity vector which is aligned with the x_1-axis. For convenience, we define

$$u_\theta = u_1 \cos\theta + u_2 \sin\theta, \tag{5.16}$$

the velocity fluctuations parallel to the measuring baseline, with corresponding correlation function,

$$R_\theta(\mathrm{r}) = \overline{u_\theta(\mathrm{x}, t)u_\theta(\mathrm{x}+\mathrm{r}, t)}, \tag{5.17}$$

spectral density,

$$\varphi_\theta(\mathrm{k}) = \varphi_{11}(\mathrm{k})\cos^2\theta + [\varphi_{12}(\mathrm{k}) + \varphi_{21}(\mathrm{k})]\cos\theta\sin\theta + \varphi_{22}(\mathrm{k})\sin^2\theta, \qquad (5.18)$$

and one-dimensional spectrum,

$$F_\theta(k_1) = \iint_{-\infty}^{\infty} \varphi_\theta(\mathrm{k})\, dk_2\, dk_3. \qquad (5.19)$$

Assuming isotropy and a power law dependence for the three-dimensional spectral density as per 5.12, (5.19) can be solved analytically to yield

$$F_\theta(k_1) = Ck_1^{-p}\,\frac{\cos^2\theta + p\sin^2\theta + 1}{2p(p+2)}. \qquad (5.20)$$

Under this formalism, the streamwise spectrum is

$$F_{11}(k_1) = F_\theta(k_1)|_{\theta=0^\circ} = Ck_1^{-p}\,\frac{1}{p(p+2)}, \qquad (5.21)$$

and the cross-stream spectrum is

$$F_{22}(k_1) = F_\theta(k_1)|_{\theta=90^\circ} = Ck_1^{-p}\,\frac{p+1}{2p(p+2)}. \qquad (5.22)$$

Clearly, the one-dimensional spectrum functions have a power law form for any region in which $E(k)$ has a power law form. In an inertial subrange, the streamwise spectrum,

$$F_{11}(k_1) = \frac{9}{55}A\epsilon^{2/3}k_1^{-5/3}, \qquad (5.23)$$

is obtained using (5.15), and the cross-stream to streamwise spectral ratio is

$$\frac{F_{22}(k_1)}{F_{11}(k_1)} = \frac{p+1}{2} = \frac{4}{3}. \qquad (5.24)$$

This last relation is often used in empirical work to test for the existence of an inertial subrange [24]. The velocity fluctuations observed by the line-averaging instrument are

$$\tilde{u}_\theta(\mathbf{x},t) = \frac{1}{\ell}\int_{-\ell/2}^{\ell/2} u_\theta(\mathbf{x}+\mathbf{s},t)\,ds. \tag{5.25}$$

Using (5.3) to solve the path-integral,

$$\tilde{u}_i(\mathbf{x},t) = \int_{-\infty}^{\infty} \exp(i\mathbf{k}\cdot\mathbf{x})\,\frac{\sin(\mathbf{k}\cdot\boldsymbol{\ell}/2)}{\mathbf{k}\cdot\boldsymbol{\ell}/2}\,dZ_i(\mathbf{k},t), \tag{5.26}$$

one obtains an expression for the one-dimensional spectrum of the integrated velocity measurements,

$$\tilde{F}_\theta(k_1) = \iint_{-\infty}^{\infty} \frac{\sin^2(\mathbf{k}\cdot\boldsymbol{\ell}/2)}{(\mathbf{k}\cdot\boldsymbol{\ell}/2)^2}\,\varphi_\theta(\mathbf{k})\,dk_2\,dk_3. \tag{5.27}$$

5.2.3 Spectral Transfer Ratio

To investigate the relationship between line-averaged and ideal one-dimensional spectra, the transfer ratio

$$T(k_1\ell,\theta,p) = \frac{\tilde{F}_\theta(k_1)}{F_\theta(k_1)} \tag{5.28}$$

is defined; it indicates spectral attenuation due to line-averaging as a function of wavenumber, pathlength, orientation of the measuring baseline relative to the mean velocity vector, and spectral slope. Conventional path-averaging current meters have short measuring baselines compared to the scales of interest, $k_1\ell \to 0$, so that line-averaged measurements approximate point measurements, $T(k_1\ell,\theta,p) = 1$. The acoustic pathlength during our arctic experiment was long compared to the scales associated with velocity fine structure.

A response function for the path-averaging filter characteristic of the acoustical instrument was derived in Section 4.5.2. For flow components with coherent phase

along the entire measuring baseline, the instrument behaves as a lowpass spatial filter with cutoff wavelength $\lambda_0 \approx 450$ m and zero phase shift in the passband. According to (4.8), the high wavenumber region of the integrated spectrum is attenuated by a factor of $(1/k\ell)^2$ or more relative to the true spectrum. This attenuation would make the measurement of the integrated spectrum difficult if not impossible at high wavenumbers.

For short wavelengths compared to the separation of the acoustical transducers, one can no longer assume that the phase of the flow components remains coherent along the measuring baseline. For this reason, the line-averaging process destroys phase information at high wavenumbers. Nevertheless, it remains possible to relate the spectrum of the integrated velocity measurements to the true spectrum as will be discussed in this section. It will be shown that $T(k_1\ell, \theta, p)$ is inversely proportional to $k_1\ell$ and not $(k_1\ell)^2$ as is the case for coherent disturbances spanning the measuring baseline; this makes the measurement of the integrated spectrum at high wavenumbers possible.

Asymptotic Approximation

When the scales being measured are of the same order of magnitude as the length of the measuring baseline, $k_1\ell \sim 2\pi$, numerical integration is required to solve for the spectral transfer ratio. Kaimal [31] solved (5.28) numerically for an inertial subrange and for $\theta = 90°$. Here, we consider long measuring baselines compared to the scales of interest; an analytic solution can be obtained because of the asymptotic behaviour of the path-integral (5.27):

$$\int_{-\infty}^{\infty} \frac{\sin^2(\mathrm{k}\cdot\ell/2)}{(\mathrm{k}\cdot\ell/2)^2}\,\varphi_\theta(\mathrm{k})\,dk_2 = \frac{2\pi}{\ell\sin\theta}\,\varphi_\theta(k_1, -k_1\cot\theta, k_3), \qquad (5.29)$$

for $k_1\ell\sin\theta \gg 4\pi$. In effect, for large ℓ, the left hand side of (5.29) is a convolution in k_2-space between an impulse function and the spectral density $\varphi_\theta(\mathrm{k})$ (Appendix C).

Homogeneous Isotropic Turbulence

For homogeneous isotropic turbulence, the asymptotic form of the one-dimensional line-averaged spectrum is

$$\tilde{F}_\theta(k_1) = \frac{C k_1^{-p}}{k_1 \ell} \frac{K(p) \sin^p \theta}{p}, \tag{5.30}$$

and the spectral transfer ratio is

$$T_i(k_1 \ell, \theta, p) = \frac{S_i(\theta, p)}{k_1 \ell}, \tag{5.31}$$

for $k_1 \ell \sin \theta \gg 4\pi$, where the subscript i of T_i and S_i indicates isotropy,

$$S_i(\theta, p) = \frac{2(p+2) K(p) \sin^p \theta}{\cos^2 \theta + p \sin^2 \theta + 1}, \tag{5.32}$$

$$K(p) = \frac{\Gamma(1/2)\Gamma(p/2 + 1/2)}{\Gamma(p/2)}, \tag{5.33}$$

and $\Gamma(x)$ is the gamma function. For an inertial subrange, $p = 5/3$, and $K(5/3) \approx 1.4$. In Fig. 5.1, the analytic expression for $T_i(k_1 \ell, 90°, 5/3)$ is compared with the exact numerical solution. As expected, (5.31) is not valid when the baseline is short compared with the wavelength of the turbulent eddies being sensed. However, when $k_1 \ell > 8\pi$, there is good correspondence between the asymptotic and the exact solution; the fractional error is less than 7%. Equation (5.31) implies that line-averaged measurements are inversely proportional to the dimensionless wavenumber $k_1 \ell$, a result that is generalized to anisotropic flows later in this section.

Another useful ratio relates $\tilde{F}_\theta(k_1)$, the line-averaged one-dimensional spectrum, to $F_{11}(k_1)$, the streamwise spectrum, that is

$$T_s(k_1 \ell, \theta, p) = \frac{\tilde{F}_\theta(k_1)}{F_{11}(k_1)} = \frac{S_s(\theta, p)}{k_1 \ell}, \tag{5.34}$$

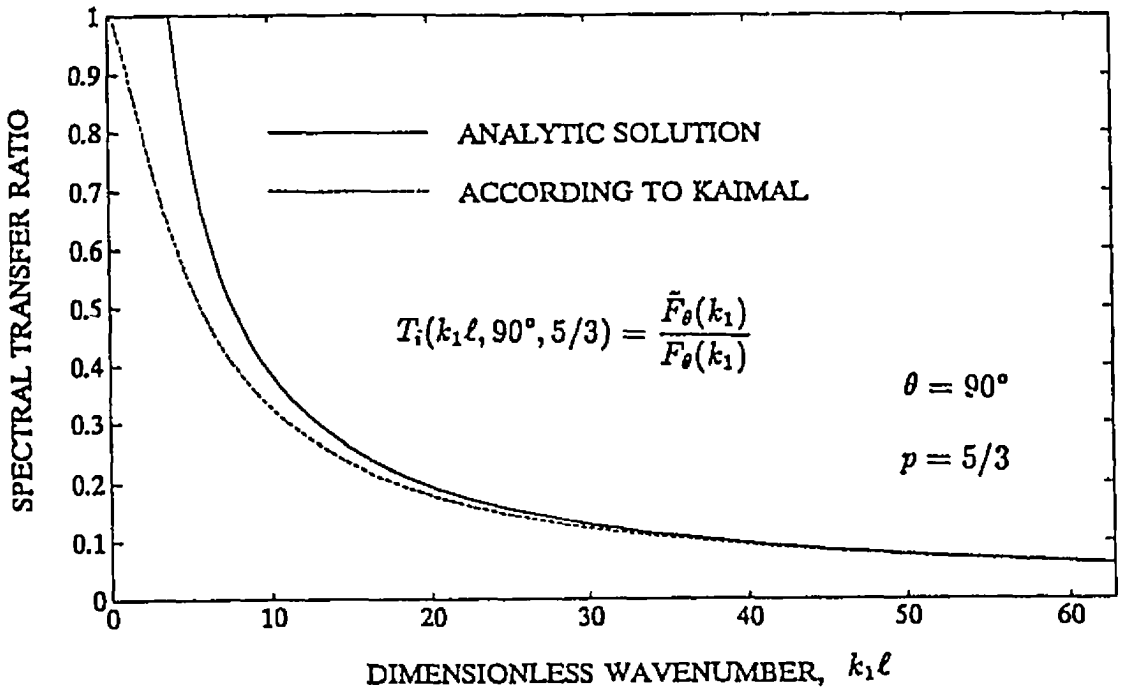

Figure 5.1: Ratio between line-averaged and true one-dimensional kinetic energy spectra as a function of the dimensionless wavenumber parameter $k_1\ell$ for isotropic turbulence. A numerical solution is compared with the analytic expression derived for high wavenumbers.

where

$$S_z(\theta, p) = (p+2)K(p)\sin^p\theta. \tag{5.35}$$

Fig. 5.2 displays the dependence of the spectral transfer ratios, $T_i(k_1\ell, \theta, p)$ and $T_s(k_1\ell, \theta, p)$, on θ. We observe that the line-averaged measurements are most sensitive to turbulent fine structure when the measuring baseline is perpendicular to the vector mean current. When θ is small, some of the assumptions required by the theory fail. For example, it becomes harder to satisfy $k_1\ell\sin\theta \gg 4\pi$. In Section 5.2.4, we also show that Taylor's frozen field hypothesis is unlikely to hold at small θ for long measuring baselines.

Axisymmetric Turbulence

The expressions developed so far are valid for homogeneous and isotropic turbulence. We now relax the assumptions of isotropy and homogeneity in stages to

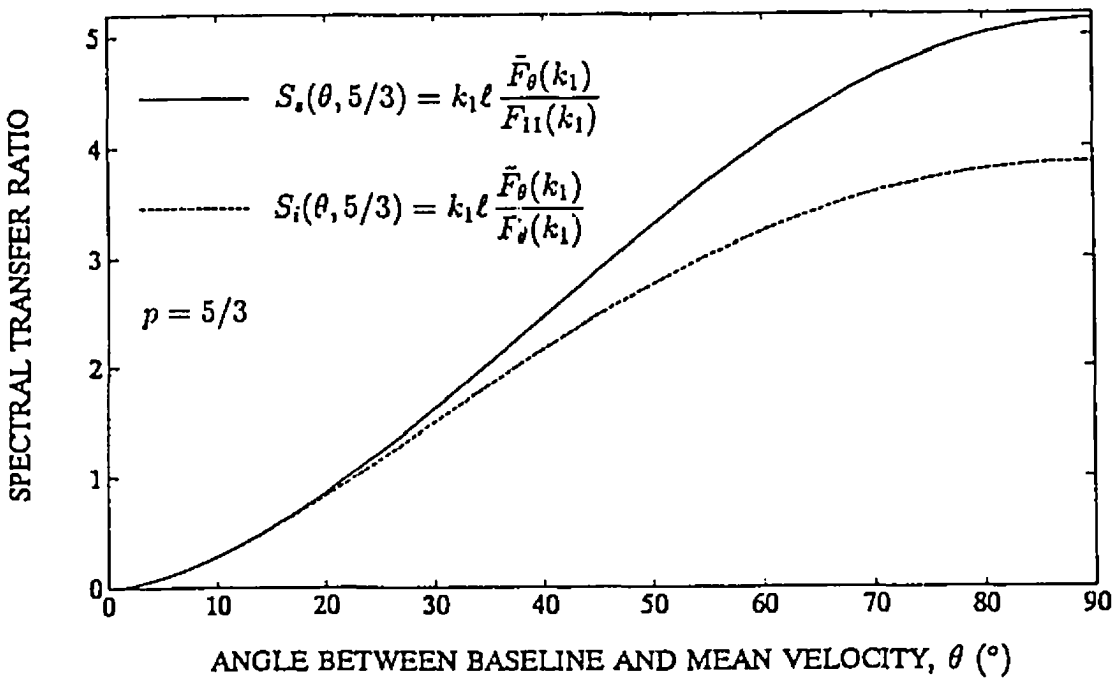

Figure 5.2: Spectral transfer ratio dependence on the angle between the measuring baseline and the mean velocity vector. The sensitivity of the measurements is greatest when $\theta = 90°$.

obtain results that are progressively more general. A type of turbulence which is next to isotropic in order of simplicity, but which is more commonly occurring in practice is axisymmetric turbulence. Instead of spherical symmetry, or isotropy, axisymmetric turbulence possesses symmetry about a preferred direction, n. Axisymmetry requires that the mean value of any function of the velocities and their derivatives be invariant for rotations about n [3]. The proximity of a rigid boundary, such as floating ice, favors horizontal motion. McPhee [45] reports that heat and momentum flux under ice is typically caused by turbulent eddies that are of order 10-20 m in horizontal extent and a few meters in vertical extent. Therefore, in a given wavenumber range, the flow is more likely to be axisymmetric about the vertical axis rather than isotropic.

Herring [29] introduced a useful formalism for describing axisymmetric turbulence. The spectral density tensor is expressed in terms of two scalars, ψ(k) and

$\psi'(\mathrm{k})$, the first of which represents the modal kinetic energy transverse to n, and the second the modal energy perpendicular to both k and n. That is

$$\varphi_{ij}(\mathrm{k}) = \psi(\mathrm{k})e_i(\mathrm{k})e_j(\mathrm{k}) + \psi'(\mathrm{k})e'_i(\mathrm{k})e'_j(\mathrm{k}), \tag{5.36}$$

where

$$\mathrm{e}(\mathrm{k}) = \frac{\mathrm{k} \times \mathrm{n}}{|\mathrm{k} \times \mathrm{n}|}, \tag{5.37}$$

$$\mathrm{e}'(\mathrm{k}) = \frac{\mathrm{k} \times \mathrm{e}(\mathrm{k})}{|\mathrm{k} \times \mathrm{e}(\mathrm{k})|}, \tag{5.38}$$

and $\psi(\mathrm{k})$, $\psi'(\mathrm{k})$ are axisymmetric scalars. In terms of this formalism, the simplest possible characterization of axisymmetric turbulence has

$$\psi(\mathrm{k}) = \frac{(1-a)E(k)}{2\pi k^2}, \tag{5.39}$$

and

$$\psi'(\mathrm{k}) = \frac{aE(k)}{2\pi k^2}, \tag{5.40}$$

where a is a parameter characterizing anisotropy and $0 \leq a \leq 1$ [68]. Equation (5.36) can also be written

$$\varphi_{ij}(\mathrm{k}) = [\psi(\mathrm{k}) - \psi'(\mathrm{k})]e_i(\mathrm{k})e_j(\mathrm{k}) + \psi'(\mathrm{k})(\delta_{ij} - k_i k_j/k^2); \tag{5.41}$$

therefore $a = 1/2$ implies isotropy. Taking n to be the vertical unit vector and assuming the energy spectrum has a power law dependence on the wavenumber as per (5.12), we obtain the one-dimensional spectra,

$$F_\theta(k_1) = \frac{Ck_1^{-p}}{p(p+1)(p+2)}[(b+ap)\cos^2\theta + (a+bp)\sin^2\theta], \tag{5.42}$$

and

$$F_{33}(k_1) = aCk_1^{-p}\frac{p+1}{p(p+2)}, \tag{5.43}$$

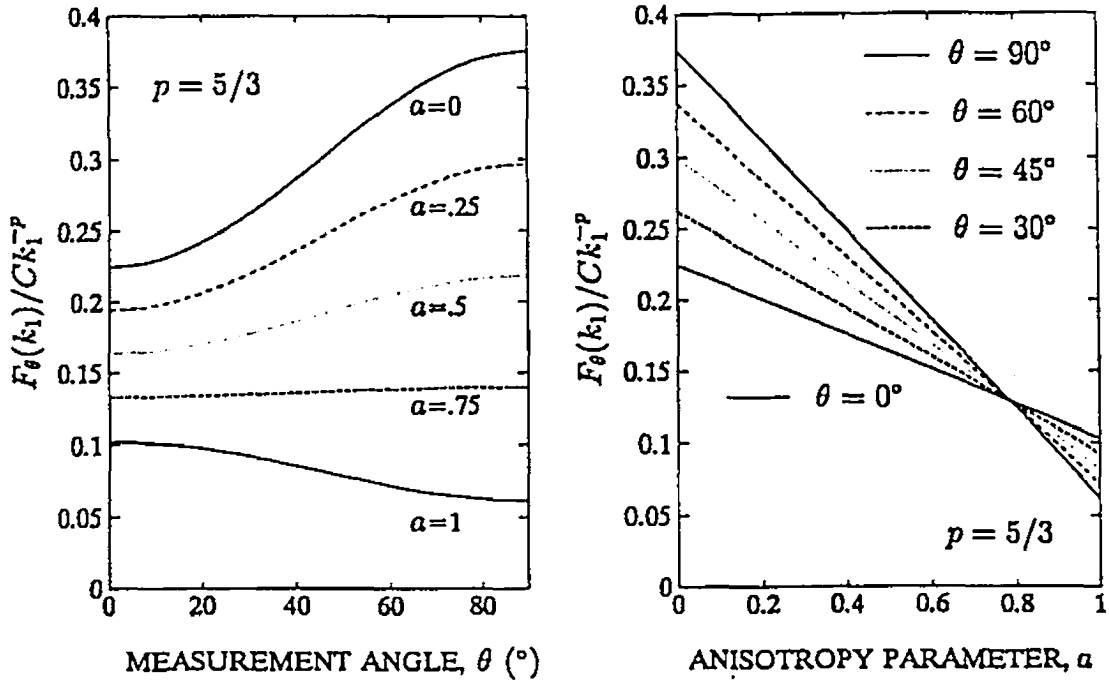

Figure 5.3: One-dimensional energy spectrum versus measurement angle and anisotropy parameter.

where

$$b = (p+2)(1-a). \tag{5.44}$$

In Fig. 5.3, $F_\theta(k_1)/Ck_1^{-p}$ is plotted as a function of the measurement angle, θ, and anisotropy parameter, a, for a spectral slope $p = 5/3$. By definition, $a = 0$ implies that all the turbulent kinetic energy is contained in the horizontal mode of motion. The figure shows that as a increases, the fraction of turbulent energy detected by horizontal velocity measurements decreases. The figure also shows that there is a certain value of a,

$$a_o = \frac{p+2}{p+3} = 0.79 \quad \text{for } p = 5/3, \tag{5.45}$$

for which the measured horizontal kinetic energy spectrum does not depend on measurement angle θ. As θ approaches 90°, the measured kinetic energy increases for $a < a_o$ and decreases for $a > a_o$.

Fig. 5.4 displays the ratio of cross-stream to streamwise one-dimensional spectra

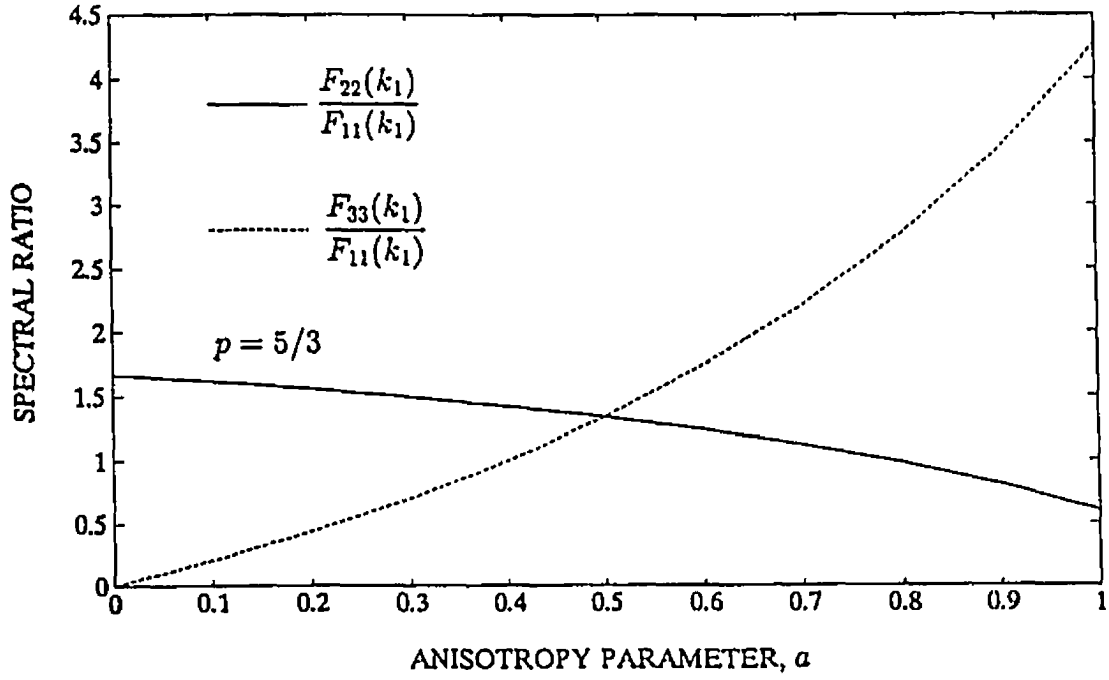

Figure 5.4: Ratio of cross-stream to streamwise one-dimensional spectra as a function of the anisotropy parameter a.

as a function of the anisotropy parameter a. This suggests an empirical method for measuring a. If a turbulent flow is axisymmetric about a known direction, then the cross-stream to streamwise spectral ratio can be used to quantify the departure from isotropy. As the flow approaches isotropy, $a = 1/2$, the spectral ratio tends to 4/3.

Assuming a long measuring baseline, $k_1 \ell \sin\theta \gg 4\pi$, we find an expression for the line-averaged spectrum,

$$\tilde{F}_\theta(k_1) = 2(1-a)\frac{C k_1^{-p}}{k_1 \ell}\frac{K(p)\sin^p\theta}{p}, \tag{5.46}$$

and the spectral transfer ratio for axisymmetric turbulence,

$$T_a(k_1\ell, \theta, p) = \frac{S_a(\theta, p)}{k_1 \ell}, \tag{5.47}$$

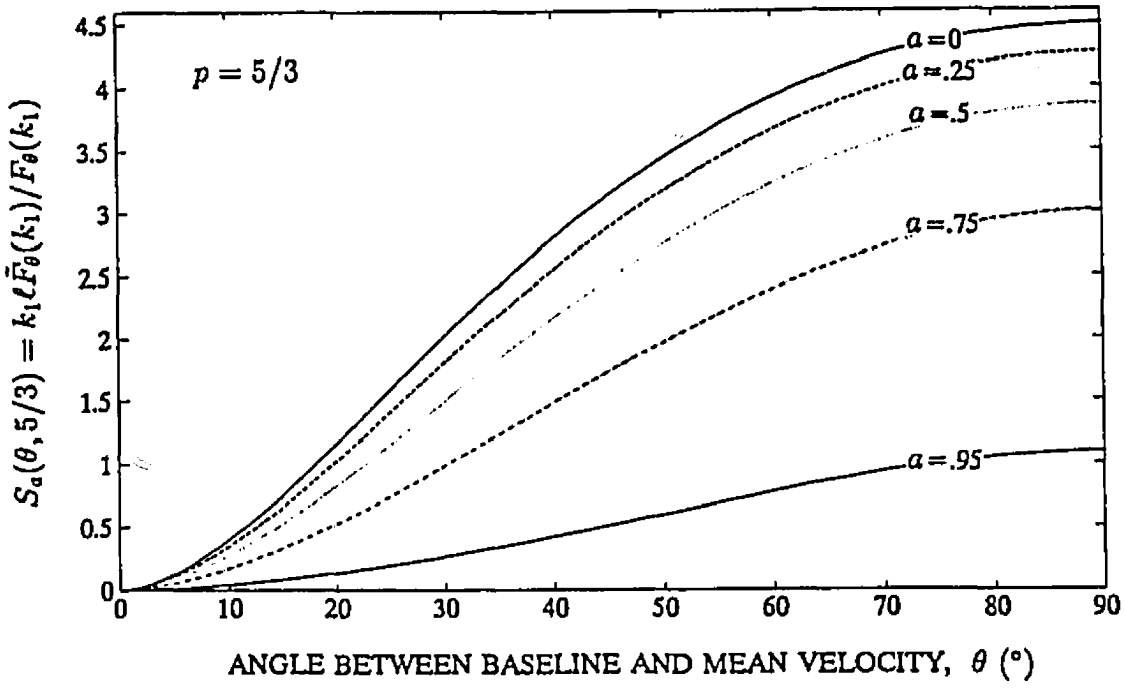

Figure 5.5: Spectral transfer ratio between line-averaged and point measurements of velocity as a function of measurement angle and anisotropy parameter.

where

$$S_a(\theta, p) = \frac{2b(p+1)K(p)\sin^p\theta}{(b+ap)\cos^2\theta + (a+bp)\sin^2\theta}. \tag{5.48}$$

Equations (5.44), (5.47) and (5.48) say that the sensitivity of line-averaged horizontal velocity measurements to turbulent velocity fine structure is a function both of the measuring angle and of the relative amount of turbulent kinetic energy contained in the horizontal mode of motion. In Fig. 5.5, we plot $S_a(\theta, 5/3)$ as a function of measuring angle, θ, and anisotropy parameter, a. The spectral transfer ratio is maximum when the measuring baseline is perpendicular to the vector mean current and all the turbulent kinetic energy is contained in the horizontal mode of motion.

Fig. 5.6 compares the axisymmetric to the isotropic spectral transfer ratio as a function of the anisotropy parameter a. We see that for $a = 0$, *i.e.* when all the kinetic energy is contained in the horizontal mode of motion, and $\theta = 90°$,

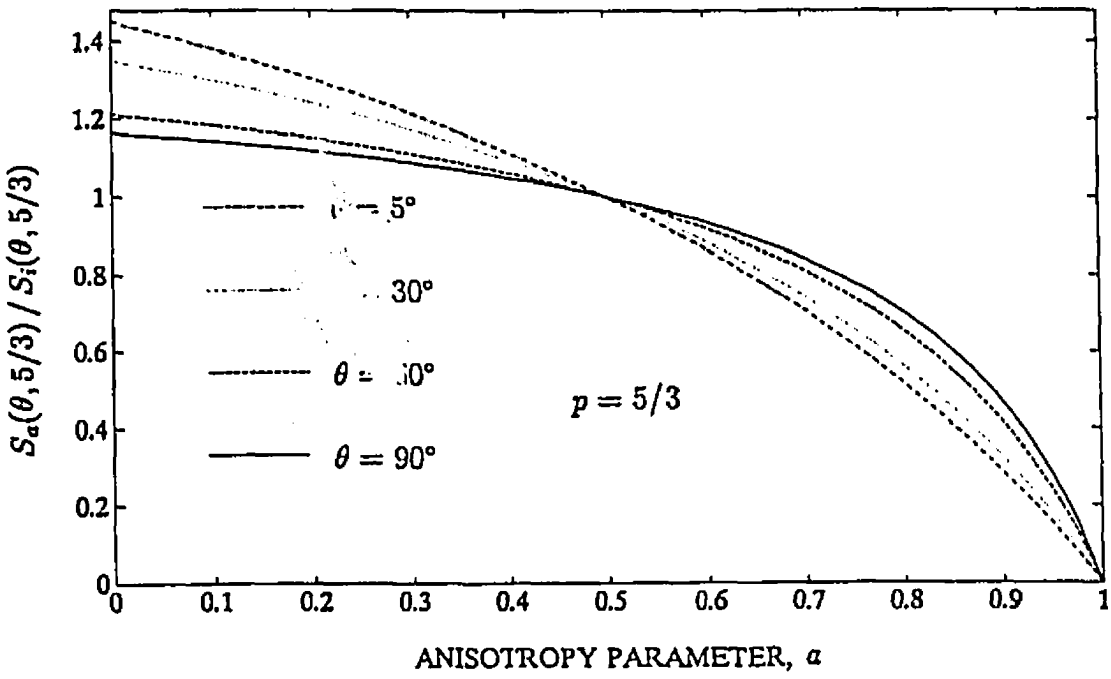

Figure 5.6: Comparison of axisymmetric to isotropic spectral transfer ratio as a function of the anisotropy parameter a.

i.e. the measuring baseline is perpendicular to the vector mean flow, the spectral transfer function is 16% higher than for the isotropic case. For other values of θ, the discrepancy between the isotropic and the axisymmetric spectral transfer ratio is at most 46% for $a < 1/2$. Equation (5.47) also says that the spectral transfer ratio is inversely proportional to the dimensionless wavenumber $k_1\ell$.

Anisotropic Turbulence

It has been shown that for sufficiently long measuring baselines, $k_1\ell \sin\theta \gg 4\pi$, the spectral transfer function, $T(k_1\ell) = \tilde{F}(k_1)/F(k_1)$, is inversely proportional to the dimensionless wavenumber $k_1\ell$, both for isotropic and axisymmetric flows. Here, a dimensional argument is used to extend this result to fully anisotropic turbulence.

Consider a baseline of length ℓ that is split in two pieces of length α and β so that

$$\ell = \alpha + \beta. \tag{5.49}$$

The line-averaged velocity along ℓ, $\tilde{u}$, is related to $\tilde{u}_\alpha$ and $\tilde{u}_\beta$, the velocities averaged along α and β respectively, by

$$\tilde{u} = \frac{\alpha\tilde{u}_\alpha + \beta\tilde{u}_\beta}{\ell}. \tag{5.50}$$

Define $\tilde{F}_\alpha(k_1)$ and $\tilde{F}_\beta(k_1)$ to be the one-dimensional spectra associated with $\tilde{u}_\alpha$ and $\tilde{u}_\beta$ respectively. For $k_1\alpha$ and $k_1\beta$ sufficiently large, $\tilde{u}_\alpha$ and $\tilde{u}_\beta$ are statistically independent and in that wavenumber range

$$\tilde{F}(k_1) = \frac{\alpha^2\tilde{F}_\alpha(k_1) + \beta^2\tilde{F}_\beta(k_1)}{\ell^2}. \tag{5.51}$$

Assuming homogeneity, (5.51) can only be satisfied when

$$\ell\tilde{F}(k_1) = \alpha\tilde{F}_\alpha(k_1) = \beta\tilde{F}_\beta(k_1), \tag{5.52}$$

i.e. the measured spectra are inversely proportional to the averaging length. It is also known that line-averaged spectra and point spectra share the same units; therefore, they must be related by a non-dimensional constant, and k_1 is the only relevant parameter that can be used to non-dimensionalize ℓ. This suggests that at high wavenumbers the spectral transfer function is inversely proportional to the non-dimensional wavenumber,

$$T(k_1\ell) \propto \frac{1}{k_1\ell}, \tag{5.53}$$

which is consistent with analytic expressions (5.31), (5.34) and (5.47). This dimensional argument illustrates why attenuation due to line-averaging is proportional to $1/k_1\ell$ when the length scales considered are short compared to the measuring baseline, and not $(1/k\ell)^2$ as is the case for coherent disturbances along the entire measuring baseline.

Inhomogeneous Turbulence

Up to this point, it has been assumed that the turbulent flow is homogeneous. In this section, the assumption of homogeneity is relaxed by considering measurements that span several regions of locally homogeneous turbulence. Consider a baseline that traverses two regions with different spectral characteristics; $F_\alpha(k_1)$ is the spectrum associated with the region spanned by α and similarly β spans the region characterized by $F_\beta(k_1)$ so that $\ell = \alpha + \beta$. Using (5.53), the line averaged spectrum can be written

$$\tilde{F}(k_1) \propto \frac{1}{k_1 \ell}\left(\frac{\alpha F_\alpha(k_1) + \beta F_\beta(k_1)}{\ell}\right), \tag{5.54}$$

i.e. the integrated spectrum $\tilde{F}(k_1)$ is a true average along the measuring baseline. The same argument can be made for an arbitrary number of locally homogeneous regions, provided the scales of interest are small compared to the extent of each region. For this reason, line-averaged measurements can provide a representative areal average, in the plane formed by the mean velocity vector and the measuring baseline, that is not unduly influenced by local inhomogeneities of the flow.

5.2.4 Nonfrozen Turbulence

The interpretation of time spectra in terms of spatial correlations is done by assuming a frozen field pattern advected by the mean flow past a sensor. Alternatively, the sensor can be moved with a known velocity through a frozen field. This assumption, first introduced by Taylor [74], has been used extensively to infer the spatial characteristics of turbulence in the atmosphere and the ocean. Here, the conditions under which the frozen field assumption is justified are reviewed, and correction formulas for the spatial and temporal variability of advection velocity across the measuring baseline are derived.

Frozen Field Hypothesis

Taylor's frozen field hypothesis is based on the argument that when the streamwise speed fluctuations are small relative to the mean velocity, *i.e.*

$$\overline{u_1^2} \ll \overline{U}^2, \tag{5.55}$$

then the time rate of change at a fixed point can be approximated by

$$\frac{\partial \mathrm{u}}{\partial t} \approx -\overline{U}\frac{\partial \mathrm{u}}{\partial x_1}. \tag{5.56}$$

If this assumption holds, the space and time correlation coefficients are related by

$$R(r_1 = \overline{U}\tau) \approx R(\tau), \tag{5.57}$$

and the streamwise one-dimensional spatial spectrum can be obtained from the frequency spectral density of the observed time series, that is

$$F(k_1 = \omega/\overline{U}) \approx \overline{U}F(\omega). \tag{5.58}$$

Criteria for Point Measurements

Fisher and Davies [22] suggested several mechanisms which can prevent the direct interpretation of time spectra as space spectra by the frozen field hypothesis in shear flows. First, different turbulent spectral components may appear to travel at different speeds past a fixed point due to the mean shear. Second, the temporal evolution of a turbulent eddy may change the apparent frequency of a particular wavenumber component. Finally, fluctuations of the advection velocity may also change the observed frequency as small eddies are carried within larger ones. We will examine each of these mechanisms in more detail and establish criteria under which the frozen field hypothesis can be applied to shear flows.

Lin [39] showed that Taylor's hypothesis can break down in a flow with nonuniform mean velocity, $\overline{U}(x_3)$, because the fluctuations sensed at a point might be

caused by eddies somewhere else and therefore advected with a different mean velocity. Under these circumstances, the frozen field hypothesis is expected to hold only for eddies sufficiently small that the velocity difference across them caused by the mean shear is small compared to the advection velocity, that is

$$\frac{\partial \overline{U}}{\partial x_3} \ll k_1 \overline{U}. \tag{5.59}$$

Next, we require that an eddy be essentially frozen as it is carried past a fixed point. Roughly, a turbulent eddy has characteristic length $1/k_1$ and velocity $[k_1 F(k_1)]^{1/2}$, so that a time scale is $1/[k_1^3 F(k_1)]^{1/2}$. We want this time to be short compared to the time required to advect the eddy past the measuring point, $1/k_1\overline{U}$, hence the criterion

$$k_1 F(k_1) \ll \overline{U}^2. \tag{5.60}$$

Finally, we consider the change of apparent frequency of a particular wavenumber component due to fluctuations of advection velocity. These fluctuations are a result of large eddies carrying smaller ones within them. In general, the spatial spectrum is overestimated. This is because energy at slightly higher and lower wavenumbers is aliased to k_1, and the spectrum is concave upward. Therefore, there is a net gain. Lumley [41] derived an approximate correction formula,

$$F_T(k_1) \approx F_{11}(k_1) + \frac{\overline{v_1^2}}{2\overline{U}^2}\left(k_1^2 \frac{\partial^2}{\partial k_1^2} F_{11}(k_1) - 2F_{11}(k_1)\right), \tag{5.61}$$

where $F_T(k_1)$ is the measured spectrum obtained by applying Taylor's hypothesis, $F_{11}(k_1)$ is the streamwise one-dimensional spectrum, and $v_1(\mathbf{x}, t)$ is the streamwise velocity associated with the energy containing eddies. Consider the spectrum

$$F_{11}(k_1) \propto k_1^{-p}, \tag{5.62}$$

then (5.61) says that the fractional error,

$$\frac{F_T(k_1) - F_{11}(k_1)}{F_{11}(k_1)} \approx \frac{\overline{v_1^2}}{2\overline{U}^2}[p(p+1) - 2], \tag{5.63}$$

increases with steeper spectral slope and does not vanish at high wavenumbers. Assuming $p = 5/3$, as expected in a Kolmogorov inertial subrange, and $\overline{v_1^2}/\overline{U}^2 = 2\%$, a typical value in the boundary layer beneath ice, the overestimation of the spectrum predicted by (5.63) is 2.4%.

Criteria for Line-Averaged Measurements

When the above criteria are satisfied, point measurements in a fixed location may be used to infer the streamwise spatial structure of turbulent shear flows. If, instead of point measurements, we make line-averaged velocity measurements along ℓ, some additional criteria must be imposed in order to ensure the applicability of Taylor's frozen field hypothesis.

First, in addition to (5.59) which requires that the velocity difference caused by the mean shear across an eddy be small, we must also impose the condition that the mean velocity difference across the instrument baseline be negligible, that is

$$\nabla\overline{U} \cdot \ell \ll \overline{U}. \tag{5.64}$$

It is possible to quantify the error due to mean horizontal shear, and later we will show that its effect can be neglected for typical values of shear observed during the arctic experiment.

Next, we must modify criterion (5.60) which requires that an eddy be essentially frozen as it is carried past the measuring point. The time required to advect an eddy past the instrument baseline, $1/k_1\overline{U}\sin\theta$, is a function of θ, the angle between the mean velocity vector and the baseline. When θ is small, the advection time is $(\ell + 1/k_1)/\overline{U}$. Therefore, eddies appear frozen as they are advected by the instrument if

$$k_1 F(k_1) \ll \overline{U}^2 \sin^2\theta \qquad \text{for} \qquad k_1 \geq \frac{1}{\ell}\left(\frac{1-\sin\theta}{\sin\theta}\right), \tag{5.65}$$

and

$$k_1^3 F(k_1)\left(\ell + \frac{1}{k_1}\right)^2 \ll \overline{U}^2 \qquad \text{for} \qquad k_1 < \frac{1}{\ell}\left(\frac{1-\sin\theta}{\sin\theta}\right). \tag{5.66}$$

Correction for Variable Advection Velocity

Finally, we consider how the fluctuations of advection velocity affect the measurement of spatial spectra. Following Lumley [41], we assume that at high wavenumbers the spectrum may be described adequately by isotropic frozen regions advected by a spatially uniform fluctuating velocity, $\mathbf{v}(\mathbf{x},t)$, that is

$$u_i(\mathbf{x},t) = \int_{-\infty}^{\infty} \exp[i\mathbf{k}\cdot(\mathbf{x} - \overline{\mathbf{U}}t - \mathbf{v}t)]\, dZ_i(\mathbf{k}), \tag{5.67}$$

where $dZ_i(\mathbf{k})$ is defined as before. The fluctuations of advection velocity, $\mathbf{v}(\mathbf{x},t)$, may have the characteristics of the energy containing turbulent eddies as Lumley assumed, or they may have other causes such as high frequency internal waves. We also assume that $\mathbf{v}$ and $d\mathbf{Z}$ are statistically independent,

$$\overline{\mathbf{v}\, d\mathbf{Z}} = \overline{\mathbf{v}}\,\overline{d\mathbf{Z}}, \tag{5.68}$$

and that, over the range of $\mathbf{k}$ for which $\varphi_{ij}(\mathbf{k})$ is nonzero, one may approximate the characteristic function of $\mathbf{v}t$ by its first two terms,

$$\overline{\exp(-i\mathbf{k}\cdot\mathbf{v}t)} = 1 - \frac{t^2}{2}\overline{(\mathbf{k}\cdot\mathbf{v})^2}. \tag{5.69}$$

We diverge from Lumley's work in that we need to consider line-averaged velocity fluctuations, $\tilde{u}_\theta(\mathbf{x},t)$ instead of point measurements. Using the above assumptions, and observing that

$$\int_{-\infty}^{\infty} \exp(-ik_1\overline{U}t)\,(\overline{U}t)^2 F(k_1)\, dk_1 = \int_{-\infty}^{\infty} \exp(-ik_1\overline{U}t)\,\frac{\partial^2}{\partial k_1^2} F(k_1)\, dk_1, \tag{5.70}$$

one can find an expression for the line-averaged spatial spectrum obtained by applying Taylor's hypothesis, $\tilde{F}_T(k_1)$, in terms of the spectral tensor $\varphi_{ij}(\mathrm{k})$, that is

$$\tilde{F}_T(k_1) = \tilde{F}_\theta(k_1) + \frac{1}{2\overline{U}^2}\frac{\partial^2}{\partial k_1^2}\iint_{-\infty}^{\infty}\overline{(\mathrm{k}\cdot\mathrm{v})^2}\,\tilde{\varphi}_\theta(\mathrm{k})\,dk_2\,dk_3, \tag{5.71}$$

where

$$\tilde{\varphi}_\theta(\mathrm{k}) = \frac{\sin^2(\mathrm{k}\cdot\ell/2)}{(\mathrm{k}\cdot\ell/2)^2}\varphi_\theta(\mathrm{k}), \tag{5.72}$$

and $\varphi_\theta(\mathrm{k})$, $\tilde{F}_\theta(k_1)$ are defined as in (5.18) and (5.27). If the fluctuations of the advection field, $\mathrm{v}(\mathrm{x},t)$, are isotropic, then

$$\overline{(\mathrm{k}\cdot\mathrm{v})^2} = k^2\overline{v_1^2}, \tag{5.73}$$

and (5.71) reduces to

$$\tilde{F}_T(k_1) = \tilde{F}_\theta(k_1) + \frac{\overline{v_1^2}}{2\overline{U}^2}\frac{\partial^2}{\partial k_1^2}\iint_{-\infty}^{\infty}k^2\tilde{\varphi}_\theta(\mathrm{k})\,dk_2\,dk_3. \tag{5.74}$$

For a measuring baseline that is long compared to the size of the turbulent eddies being measured, we can use (5.29) to obtain an analytic correction formula for the error caused by fluctuations of the advection velocity,

$$\frac{\tilde{F}_T(k_1) - \tilde{F}_\theta(k_1)}{\tilde{F}_\theta(k_1)} = \frac{\overline{v_1^2}\,p^2}{2\overline{U}^2\sin^2\theta}, \tag{5.75}$$

for $k_1\ell\sin\theta \gg 4\pi$.

In his discussion of errors due to these factors on point measurements, Lumley considers the effect of violation of three of the assumptions made in the model: isotropy of the advection field, isotropy of the advected field, and lack of correlation between the two. He concludes that relaxation of these assumptions does not change the magnitude of the correction materially. Here, we consider the effect of anisotropy of the advection and advected field on path-averaged measurements.

We can easily relax the assumption of isotropy of the advection field, in which case (5.71) yields

$$\frac{\tilde{F}_T(k_1) - \tilde{F}_\theta(k_1)}{\tilde{F}_\theta(k_1)} = \frac{p}{2\overline{U}^2 \sin^2\theta}[(p-1)(\overline{v_1^2}\sin^2\theta + \overline{v_2^2}\cos^2\theta) + \overline{v_3^2}], \qquad (5.76)$$

for $k_1 \ell \sin\theta \gg 4\pi$. The above equation says that line-averaged spectra are influenced by both vertical and horizontal velocity fluctuations of the advection field. If the vertical velocity fluctuations are negligible, and the advection field is horizontally isotropic,

$$\overline{v_1^2} \approx \overline{v_2^2} \gg \overline{v_3^2}, \qquad (5.77)$$

then the correction formula reduces to

$$\frac{\tilde{F}_T(k_1) - \tilde{F}_\theta(k_1)}{\tilde{F}_\theta(k_1)} = \frac{\overline{v_1^2}\, p(p-1)}{2\overline{U}^2 \sin^2\theta}, \qquad (5.78)$$

i.e. the line-averaged spectra are overestimated when the shape of the spectrum is upward concave.

We can also relax the assumption of isotropy of the advected field. We find that the correction equation (5.76) remains unchanged when the isotropic advected field is replaced with one that is axially symmetric about the vertical axis.

Fig. 5.7 displays the correction required by the breakdown of Taylor's frozen field hypothesis due to fluctuations of the advection velocity, as a function of angle between the measuring baseline and the mean flow. We have assumed a spectral slope of $p = 5/3$. Traces for several values of $\overline{v_1^2}/\overline{U}^2$ are displayed, both for an isotropic advection field and for $\overline{v_3^2} = 0$. For $\overline{v_1^2} = \overline{v_2^2} = 0.10\,\overline{U}^2$ and $\overline{v_3^2} = 0$, the spectral correction predicted by (5.76) is less than 6% when the mean velocity is perpendicular to the measuring baseline. At small angles between the measuring baseline and the mean flow, the correction required is significantly larger.

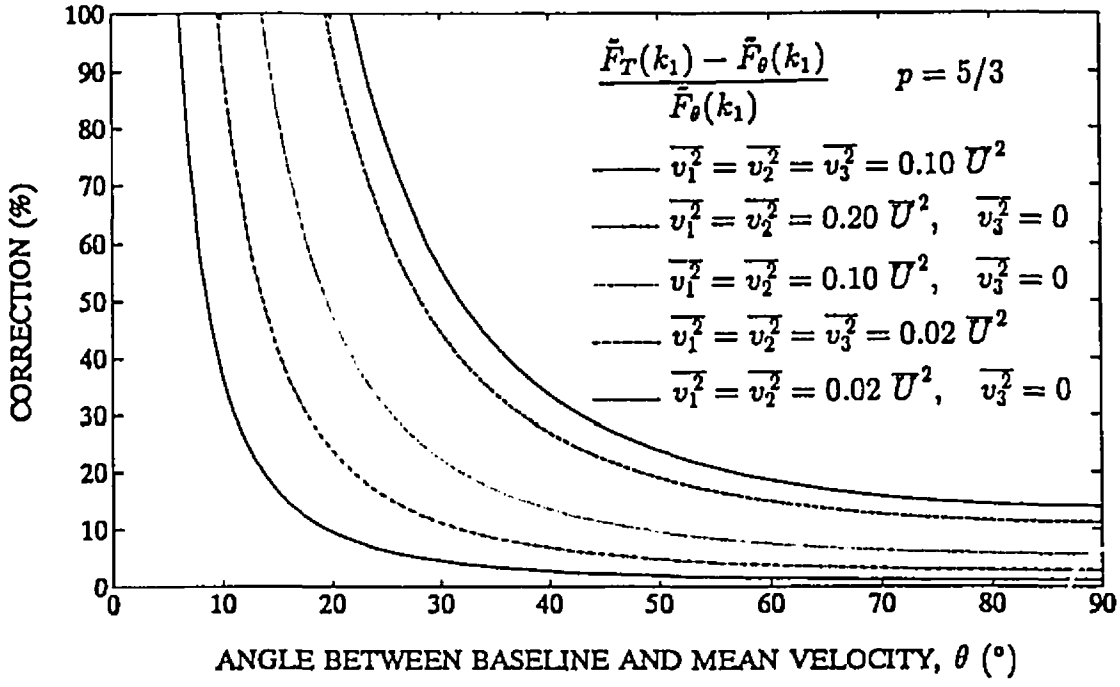

Figure 5.7: Correction of line-averaged spectra required by the breakdown of Taylor's frozen field hypothesis due to fluctuations of advection velocity along the measuring baseline.

Correction for Horizontal Shear

A similar mathematical formulation can be used to correct measured spectra for the effect of mean horizontal shear. Given mean velocity

$$\overline{U} = \overline{U_0} + \sigma x_2, \tag{5.79}$$

we can model the flow field as

$$u_i(\mathrm{x}, t) = \int_{-\infty}^{\infty} \exp[i\mathrm{k} \cdot \mathrm{x} - ik_1(\overline{U_0} + \sigma x_2)t]\, dZ_i(\mathrm{k}). \tag{5.80}$$

Assuming that

$$\exp(-ik_1\sigma x_2 t) = 1 - \frac{t^2}{2}(k_1\sigma x_2)^2 \tag{5.81}$$

is a valid approximation over the range of k for which $\varphi_{ij}(\mathrm{k})$ is nonzero, the line-averaged spatial spectrum obtained by applying Taylor's hypothesis is

$$\tilde{F}_T(k_1) = \tilde{F}_\theta(k_1) + \frac{(\sigma \ell \sin\theta)^2}{2\overline{U_0}^2} \frac{\partial^2}{\partial k_1^2} \iint_{-\infty}^{\infty} k_1^2 B(\mathrm{k}, \ell) \varphi_\theta(\mathrm{k})\, dk_2\, dk_3, \tag{5.82}$$

where

$$B(\mathrm{k}, \ell) = \frac{\sin^2(\mathrm{k}\cdot\ell/2)}{(\mathrm{k}\cdot\ell/2)^2}\left(\frac{1}{4} - \frac{2}{(\mathrm{k}\cdot\ell)^2}\right) + \frac{2\sin(\mathrm{k}\cdot\ell)}{(\mathrm{k}\cdot\ell)^3}. \tag{5.83}$$

If the instrument baseline is long compared to the size of the turbulent eddies being measured, $B(\mathrm{k}, \ell)$ simplifies to

$$B(\mathrm{k}, \ell) = \frac{\sin^2(\mathrm{k}\cdot\ell/2)}{4(\mathrm{k}\cdot\ell/2)^2}, \tag{5.84}$$

and we obtain

$$\tilde{F}_T(k_1) = \tilde{F}_\theta(k_1) + \frac{(\sigma \ell \sin\theta)^2}{8\overline{U_0}^2} \frac{\partial^2}{\partial k_1^2}[k_1^2 \tilde{F}_\theta(k_1)]. \tag{5.85}$$

Consider the spectrum

$$\tilde{F}_\theta(k_1) \propto \frac{k_1^{-p}}{k_1 \ell}, \tag{5.86}$$

then (5.85) results in the following correction formula,

$$\frac{\tilde{F}_T(k_1) - \tilde{F}_\theta(k_1)}{\tilde{F}_\theta(k_1)} = \frac{(\sigma \ell \sin\theta)^2}{8\overline{U_0}^2} p(p-1). \tag{5.87}$$

For example, for a pathlength $\ell = 200$ m, mean horizontal shear $\sigma = 10^{-4}$ s^{-1}, mean velocity $U_0 = 20$ cm/s, and spectral slope $p = 5/3$, the correction required is less than 0.2%.

In conclusion, when certain conditions are satisfied, Taylor's frozen field hypothesis can be used to interpret the time spectra of line-averaged measurements

in terms of spatial correlations. When the measuring baseline is long compared to the size of the eddies being sensed, the hypothesis fails for small angles between the mean flow and the baseline. Correction formulas for both the effect of fluctuating advection velocity and mean horizontal shear have been derived. Under conditions typical of the arctic experiment, mean horizontal shear is unlikely to cause a significant error.

5.2.5 Practical Limitations

So far, we have assumed that reciprocal acoustical transmission provides a continuous time-series of true line-averaged velocity along a given baseline. Of course, practical data sets can only approximate such requirements. In Section 4.3, we investigated the sources of error for actual reciprocal travel time measurements along 200 m horizontal paths in the ocean. In particular, we considered the effects of sampling, mean shear, multipath interference and mooring motion. Here we discuss additional limits on measurement accuracy imposed by turbulent shear and by scattering due to velocity and refractive index variability.

Due to diffraction effects, scales smaller than the first Fresnel zone cannot be acoustically resolved at the receiver (Section 6.2.3). The first Fresnel zone is the region where the pathlengths of scattered acoustic rays deviate from the unscattered pathlength by half a wavelength or less. The size of this zone is approximately $(\lambda_a \ell)^{1/2}$ at midpath, where λ_a is the acoustic wavelength and ℓ is the pathlength. The velocity measurements obtained using reciprocal travel time difference approximate a line-average only for turbulent scales larger than the dimensions of the first Fresnel zone. To probe smaller scales, the acoustic frequency must be increased or the pathlength decreased.

In the presence of shear, the acoustic propagation paths of sound rays traveling in opposite directions between two points do not overlap. The maximum separation between sound rays propagating in opposite directions is of the order of $\sigma\ell^2/4c$, where σ is the mean shear, ℓ the pathlength, and c the mean sound speed

(Appendix B). The error due to mean shear is negligible as long as the reciprocal path separation is small compared to the scales of interest (which is the case for the experimental parameters).

Turbulent shear increases at high wavenumbers roughly as $[k^3 E(k)]^{1/2}$, where k is the wavenumber and $E(k)$, the three dimensional energy spectrum. Therefore, turbulent shear can potentially interfere with velocity measurements by causing the acoustic path in one direction to differ from the reciprocal path. Turbulent shear causes some scatter of the acoustical energy and introduces some uncertainty in the measurement of travel time, but this is a second order effect when compared to the effect of velocity fluctuations parallel to the acoustic path.

Uncertainty in the measurement of travel time is also caused by refractive index fluctuations due to temperature and salinity fine structure along the acoustic path. Assuming that in the wavenumber range of interest, the sound speed field remains essentially unchanged during the time required for reciprocal transmission, the subtraction of travel times cancels out the effect of temperature and salinity fine structure. To a good first order approximation, only velocity fluctuations along the acoustic path are sensed by reciprocal travel time measurements. Therefore, the simultaneous transmission of acoustic pulses in opposite directions between two points can be used to separate the effects of velocity fine structure on acoustic propagation from the effects of sound-speed structure.

5.3 Observations

5.3.1 Experimental Data

The motivation for the preceding theoretical discussion was a desire to interpret horizontal velocity fluctuations observed with the path-averaging acoustical current meter in the turbulent boundary layer beneath ice. During the experiment, transducers were deployed at the corners of a horizontal equilateral triangle of side $\ell = 200$ m. This configuration ensures that there is at least one acoustic

path within 30° of being perpendicular to the mean velocity vector for any given direction of flow relative to the ice. Precise acoustic travel times in both directions between transducer pairs were recorded. The travel time difference of reciprocal transmissions is interpreted as the line-averaged velocity along each sonic path. Given a carrier frequency of f_a = 132.3 kHz, the first Fresnel zone has $(\lambda_a \ell)^{1/2}$ = 1.5 m diameter at midpath. In addition to the path-averaging current meter, clusters of high resolution mechanical current meters were deployed roughly at the center of the acoustic array by McPhee [45].

The underside surface of the ice is irregular and contains keels that extend down to 10 m depth in the vicinity of the acoustic array. In addition, because of the passage of internal waves and tides under the ice camp, steady current flow in one direction is rarely achieved for periods long enough to obtain good statistical averages. The assumptions of homogeneity and stationarity are not well satisfied, and some departure of observed properties from the theoretical predictions is expected.

5.3.2 Comparison with Point Measurements

Here, we present measurements made at the 20-m depth for a six hour period on April 13, 1989, during which the mean current velocity relative to the ice was 15 cm/s in a northward direction. In Fig. 5.8, we compare spectra of line-averaged and locally measured horizontal velocity fluctuations. The 95% confidence interval is estimated by calculating the variance of the unaveraged spectral estimates under the assumption of a normal distribution.

For this six-hour average, the point measurements of horizontal velocity exhibit a -5/3 dependence on the wavenumber up to length scales of 75 m, and a line of slope -5/3 has been fitted to the high wavenumber region of the point measurements. Certainly, at those scales, we do not expect the conditions of local isotropy to hold due to the proximity of the ice. Nevertheless, the existence of a -5/3 slope has often been observed outside the Kolmogorov inertial subrange, at scales where local isotropy is not satisfied [49, 24].

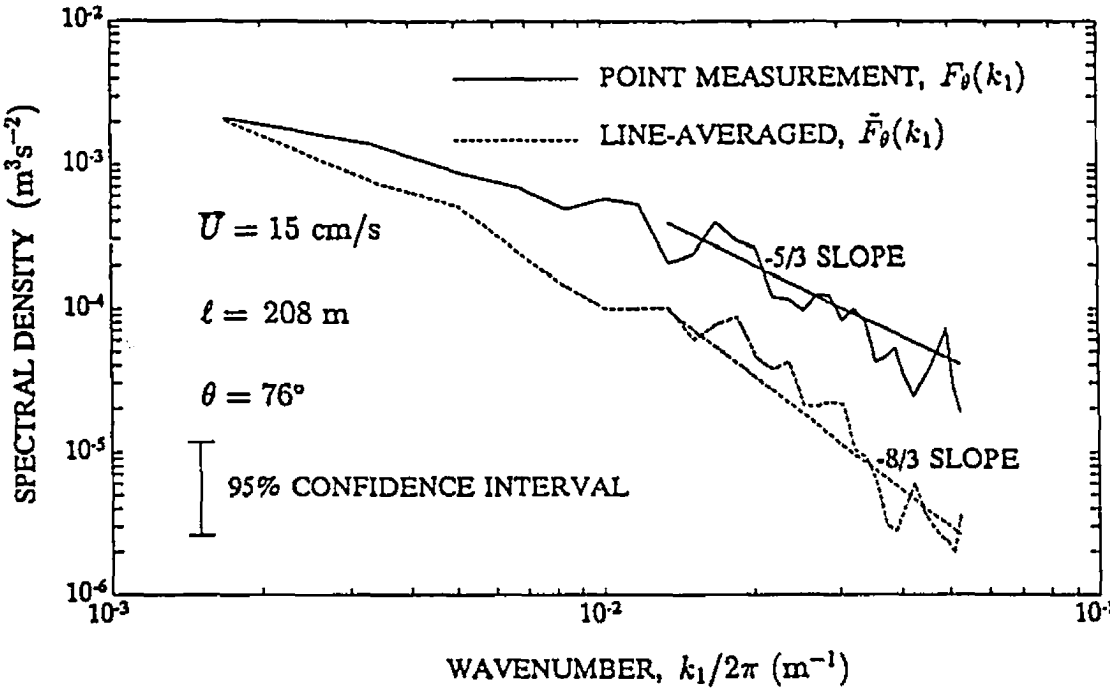

Figure 5.8: Comparison of energy spectra for point and line-averaged horizontal velocity measurements obtained 20 m beneath floating ice in the arctic boundary layer, on April 13, 1989. The point measurements were made by McPhee with a high resolution mechanical current meter. Line-averaged velocity was obtained using reciprocal acoustical travel time measurements along a 208 m horizontal path. The spectra are a six hour average during which time there was a 15 cm/s mean current flowing northward relative to the ice.

The line-averaged data corresponds to a sonic path of length, $\ell = 208$ m, that forms angle $\theta = 76°$ with the mean flow. Clearly, the integrated spectrum displays some attenuation relative to the point spectrum. Our goal is to determine whether the theory derived in Section 5.2 adequately predicts the high wavenumber attenuation of the integrated spectrum.

In the wavenumber range considered, the length scales vary from 20 to 50 m, thus satisfying the condition $k_1\ell > 8\pi$. Based on the spectra of Fig. 5.8, this wavenumber range is associated with turbulent eddies that have characteristic velocities of 0.5 cm/s, and time scales of the order of 2 hours. For mean ice-relative velocity $\overline{U} = 15$ cm/s, it only takes a few minutes to advect these eddies past the measuring baseline. Therefore, the use of Taylor's frozen field hypothesis

Parameter	*Value*
Pathlength ℓ (m)	208
Measurement angle θ (°)	76
Spectral slope p	5/3
Anisotropy parameter a	0.25
Mean ice-relative velocity $\overline{U}$ (cm/s)	15
Streamwise fluctuations of advection velocity $(\overline{v_1^2})^{1/2}$ (cm/s)	5
Cross-stream fluctuations of advection velocity $(\overline{v_2^2})^{1/2}$ (cm/s)	3
Vertical fluctuations of advection velocity $(\overline{v_3^2})^{1/2}$ (cm/s)	1

Table 5.1: Parameters used to predict spectral attenuation.

is justified.

Table 5.1, and equations (5.47) and (5.76) are used to predict the spectral attenuation due to line-averaging. All the parameters listed in the table were measured experimentally except for the anisotropy parameter a. The variance of the spectral estimates for the six-hour period of Fig. 5.8 is too large to obtain a meaningful estimate of a. However, the spectral transfer function (5.47) is fairly insensitive to the anisotropy parameter, and by assuming an intermediate value, $a = 0.25$, the maximum possible error due to this parameter does not exceed 10%. The predicted integrated spectrum which has a slope of -8/3, is drawn on Fig. 5.8, and falls well within the 95% confidence interval of the measured spectrum.

5.3.3 Angular Dependence of Spectral Transfer Ratio

Next we compare the predicted and the measured angular dependence of the spectral transfer function. The triangular acoustical array provides three separate measuring baselines separated by 120° on a horizontal plane. For the six-hour period analysed in Section 5.3.2, the three acoustic paths form angles of 13°, 46° and 76° with the mean ice-relative velocity vector. The integrated velocity spectra of the three measuring baselines have been calculated, and lines of slope -8/3 have been fitted to the high wavenumber region corresponding to turbulent eddy

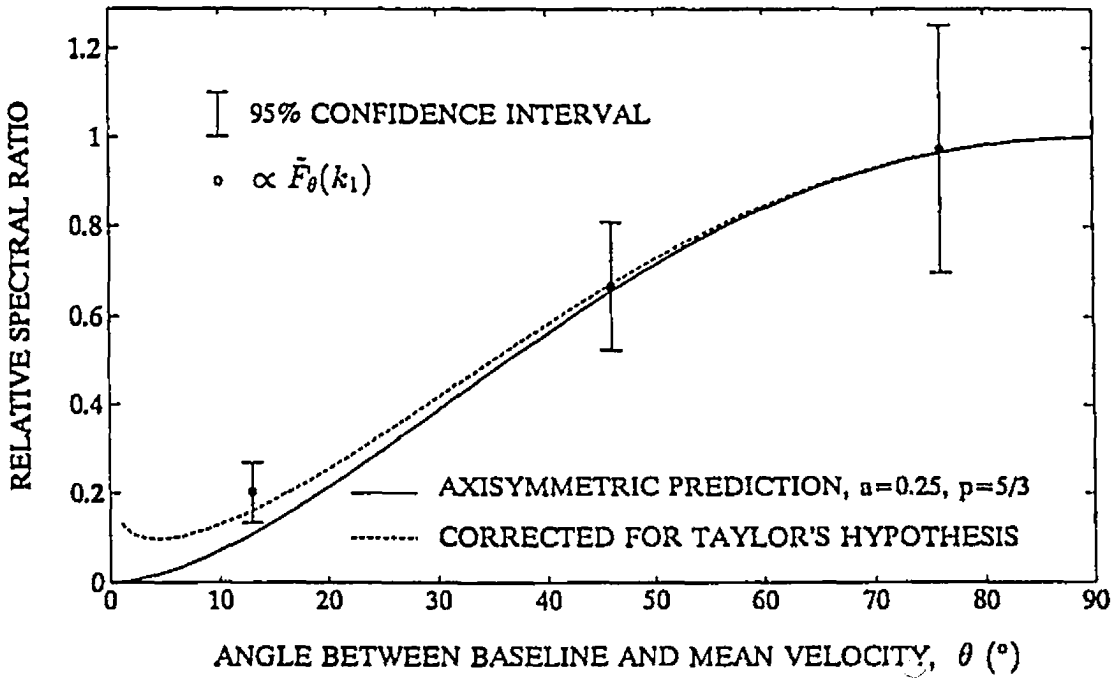

Figure 5.9: Predicted and measured dependence of the integrated spectra, $\tilde{F}_\theta(k_1)$, on the angle between the measuring baseline and the mean velocity vector, for the same six hour period as Fig. 5.8.

scale sizes ranging from 20 to 50 m. The normalized proportionality constants are displayed on Fig. 5.9 along with 95% confidence intervals. We use (5.46) to predict the angular dependence of the integrated spectrum $\tilde{F}_\theta(k_1)$, and the normalized prediction is drawn as a solid line on the figure. The broken line is the angular dependence corrected for fluctuations of advection velocity and is obtained using (5.76) and the rms velocity fluctuations listed in Table 5.1. The corrected prediction differs significantly from the uncorrected one at small measuring angles and provides a closer fit to the measured spectral level for $\theta = 13°$. We conclude that for the six-hour interval considered, there is good agreement between experimental measurements and theory, and that the Kolmogorov spectral properties, appropriately corrected, are consistent with the observations at these scales in an anisotropic regime.

5.3.4 Measurement of Dissipation Rate

The patchiness and intermittency of geophysical turbulence is an important consideration when measuring energy dissipation rate. Oakey and Elliott [58] report significant changes, often a factor of 10, in turbulence levels between two profiles a few minutes apart. Yamazaki *et al.* [85] reported a factor of 2 difference between vertical and horizontal measurements of dissipation rates. These differences emphasize the necessity of adequate space-time averaging to obtain good mean values of ϵ. We suggest a new remote sensing technique, based on line-averaged velocity measurements, for evaluating mean dissipation rate. Apart from the usual advantage associated with remote sensing techniques in general, *i.e.* that they are non-intrusive, the suggested method results in a dissipation rate averaged across the area of water formed as the turbulent fluid is carried past the measuring baseline by the mean flow. This two-dimensional average may help overcome some of the sampling limitations of conventional profilers.

It is clear from (5.12), (5.15) and (5.30) that integrated velocity spectra can be used to infer dissipation rate when measurements are taken inside the inertial subrange. The available line-averaged velocity measurements probe length scales lying just outside the inertial subrange. This is due to instrumentation limitations that could be overcome in a future experiment. Nevertheless, we can obtain rough estimates of dissipation by assuming that the spectra of horizontal turbulent velocity have a $k_1^{-5/3}$ range outside the inertial subrange with the *correct* value for the Kolmogorov constant A of (5.15). Though not supported by theory, this hypothesis may be justified first because we indeed observe a -5/3 slope outside the inertial subrange (Section 5.3.2), and second because this situation has often been reported during experimental work [24]. Here, we test this hypothesis against dissipation data collected by Padman and Dillon [61] using velocity shear probes, and by McPhee using turbulence clusters .

The velocity shear probes were mounted on a rapid-sampling vertical profiler

which was operated from an ice hut located 250 m from the acoustic array. The cycling time between profiles was usually 15-20 min. Two orthogonally mounted airfoil shear sensors measured velocity shear microstructure $u_z = \partial u/\partial z$ and $v_z = \partial v/\partial z$, with a spatial resolution of about 0.03 m. Estimates of the turbulent kinetic energy dissipation rate ϵ were made for approximately 1.4 m depth intervals by integrating the velocity shear spectra in the wave number range 2-20 cpm. Assuming isotropy of velocity fluctuations in this wave number band,

$$\epsilon = \frac{15}{2}\nu \left\langle \frac{u_z^2 + v_z^2}{2} \right\rangle \tag{5.88}$$

where ν is the kinematic viscosity of seawater, and angle brackets denote vertical averaging.

Equation (5.15) and spectral measurements obtained with turbulence clusters in the inertial subrange were used to estimate dissipation of turbulent kinetic energy by M. G. McPhee (1993, personal communication).

The estimates of dissipation rate from the acoustic array are obtained in the following way. The line-averaged horizontal velocity measurements are divided into overlapping 40-min sections, and energy spectra are computed for each section. The mean ice-relative velocity is used to convert the spectra from frequency to wavenumber space. A line of slope -8/3 is fitted to the 20-50 m subrange of each spectrum using a least squares algorithm. Equations (5.12), (5.15), (5.30), and (5.76) are then used to obtain an estimate of ϵ.

On Fig. 5.10, estimates of dissipation rate obtained with the microstructure profiler at the 20-m depth are compared to those obtained with the acoustical current meter. An 11-day time series is presented. Each point on the figure represents a 12-hour average. The mean ice-relative current speed at the 20-m depth is also drawn for reference. The mean dissipation rate, as measured with the microstructure profiler, is approximately 10^{-8} W/kg, except during days 102, 103 and 104 when it averages 10^{-7} W/kg. This increase in the dissipation rate is

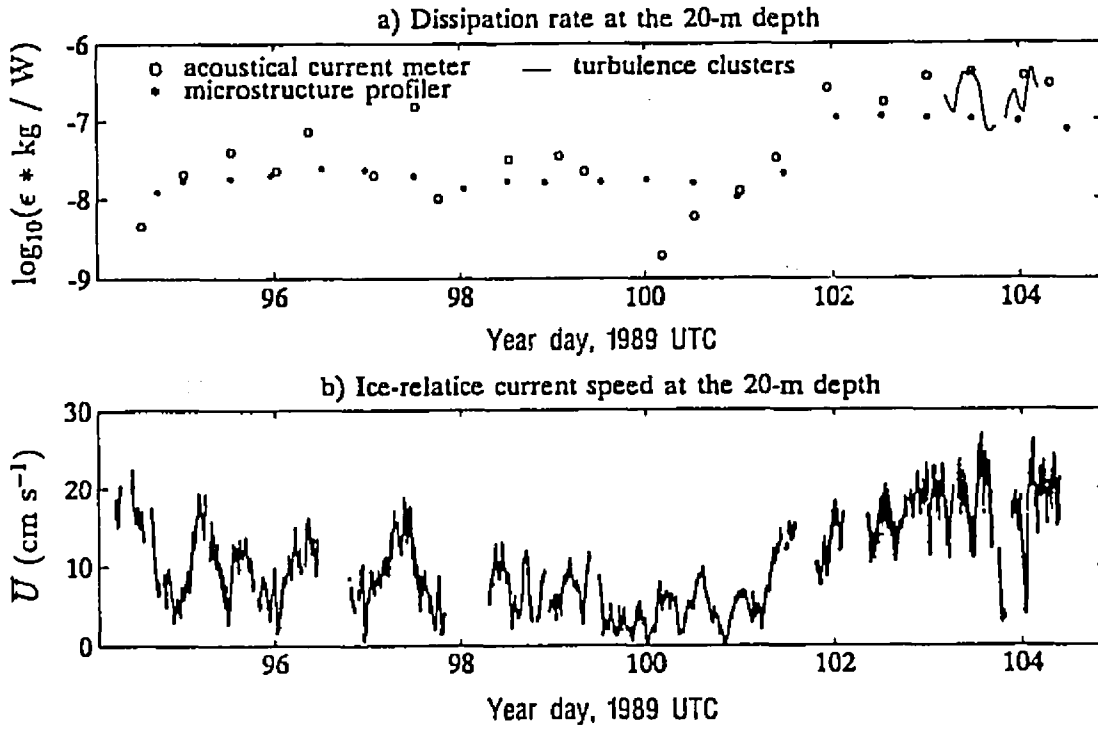

Figure 5.10: (a) Comparison of estimates of dissipation rate from microstructure profiler, turbulence clusters, and acoustical current meter at the 20-m depth. (b) Ice-relative current speed at the 20-m depth.

seen to correspond to an increased ice-relative current speed. Padman and Dillon [61] have shown that during the experiment, the depth-integrated dissipation rate is roughly proportional to the cube of the mean ice-relative current speed at 30 m below the ice.

The estimates of dissipation rate obtained with the acoustic current meter exhibit a larger scatter than those obtained with the microstructure profiler. We speculate that this large scatter results from the acoustical estimates of ϵ being based on a wavenumber range lying outside the inertial subrange, where the assumption of a -5/3 slope with the *correct* Kolmogorov constant is not always valid. Despite this limitation, the similarity of the two estimates of ϵ point to the possibility of using line-averaged velocity measurements as a remote sensing tool for measuring energy dissipation. Once instrumentation limitations are overcome, and measurements are made inside the inertial subrange, it should be possible to obtain

accurate estimates of dissipation rate.

5.4 Summary and Conclusions

In this chapter we have shown that line-averaged velocity measurements over paths of several hundred meters can be used to probe the statistical behaviour of turbulent velocity fine structure in the ocean. Measuring baselines several times longer than the scales of interest have been considered and analytic expressions for the transfer function between true and line-averaged one-dimensional spectra have been derived both for isotropic and for axially symmetric turbulence. The measurements are most sensitive to velocity fluctuations when the mean velocity vector is transverse to the measuring baseline; for this situation, the error incurred by assuming isotropy instead of axial symmetry is unlikely to exceed 16%. A dimensional argument has been used to show that for homogeneous turbulence and long measuring baselines, the spectral attenuation due to line-averaging is inversely proportional to the non-dimensional wavenumber $k_1\ell$. At sufficiently high wavenumbers, line-averaged measurements provide a representative areal average of the kinetic energy spectrum in the plane formed by the mean velocity vector and the measuring baseline.

Criteria have been obtained for applying Taylor's frozen field hypothesis to long measuring baselines, and correction formulas have been derived for the effects of variable advection velocity and mean horizontal shear. Neither of these two phenomena are likely to cause errors exceeding 10%, as long as the mean velocity vector is within 30° of being perpendicular to the measuring baseline. Some practical limitations of this measuring technique have been discussed and it is concluded that the theory is only applicable to scales of the order of the first Fresnel zone or larger. To probe smaller scales, the problem must be treated as a volume average, which has not been done here; alternatively the acoustic frequency can be increased or the pathlength decreased.

The theory appears to fit observations of high-frequency horizontal velocity fluc-

tuations obtained during the arctic experiment. The predicted spectral attenuation has been compared with the actual attenuation between point and line-averaged measurements. The predicted dependence of this attenuation on the angle between the mean ice-relative velocity and the measuring baseline has been compared to the ratio of the velocity spectra for each of the three acoustic paths of the triangular array. A new acoustic remote sensing technique for measuring turbulent energy dissipation rate has been suggested, and estimates of dissipation obtained with the acoustic array have been compared to measurements of dissipation obtained using a shear microstructure profiler.

In conclusion, reciprocal acoustical transmission applied over hundreds of meters is a promising remote sensing technique for obtaining line-averaged statistical information about the velocity fine structure of a turbulent fluid. By simultaneously transmitting acoustic pulses in opposite directions between two points, one can separate the effects of velocity fine structure on acoustic propagation from the effects of sound speed structure; in conjunction with an analysis of forward scatter acoustical scintillations, reciprocal travel time measurements can provide information about both the velocity and the sound speed structure of the intervening fluid. If the measurements are made inside a Kolmogorov inertial subrange, it is possible to obtain an areal average of energy dissipation rate which is insensitive to local inhomogeneities of the flow.

Chapter 6

Amplitude Scintillation Analysis

6.1 Introduction

One of the objectives of the arctic experiment was to study the boundary layer beneath ice using acoustic scintillations. In Chapter 5, we introduced the concept of reciprocal travel-time scintillation analysis for sensing velocity fine structure. Traditional scintillation analysis relies on the interpretation of amplitude and phase (or time-of-arrival) fluctuations of forward scattered acoustic energy, to remotely sense ocean flows. During the arctic experiment, the phase measurements were contaminated by mooring motion (Section 4.4), and for this reason phase fluctuations have not been analysed. Amplitude scintillations are less sensitive to mooring motion, and their interpretation is discussed in this chapter.

The technique of acoustic scintillation has been adapted to the study of the ocean by Clifford and Farmer [10], from previous experiments that utilized electromagnetic radiation to measure atmospheric, ionospheric and solar winds. When an acoustic wave propagates through a turbulent fluid, perturbations of the wave fronts by refractive index anomalies in the medium give rise to intensity fluctuations on a receiving plane. This time-varying scintillation pattern contains information about the intervening fluid. The structure and movement of this pattern may be interpreted in terms of the structure and motion of the intervening water.

The advection of the scintillation pattern on a receiving plane can be used

to infer fluid velocity transverse to the measuring baseline [20]. The variance of acoustic intensity at the receiver can be related to the refractive index structure parameter, which is a measure of the strength of refractive index fluctuations caused by turbulent transport of temperature, salinity and momentum past the measuring baseline [21]. By using several acoustic projectors and hydrophones, it becomes possible to focus on specific locations across the acoustic path with a resolution dependent on the complexity of the receiving and transmitting arrays [12, 19].

Refractive index fluctuations in the oceanic boundary layer are primarily the result of variations in the temperature, salinity and velocity of the fluid. The refractive index structure parameter, C_μ^2 (Section 6.2), is a measure of the strength of the refractive index fluctuations. Typical values of , C_μ^2, in the arctic boundary layer, are of order 10^{-11} $m^{-2/3}$, compared to 10^{-9} $m^{-2/3}$ reported by Farmer *et al.* [21] in a tidal channel. Therefore, the measurement of acoustic scintillations in the Arctic requires instrumentation that is two orders of magnitude more sensitive than that used previously.

The signal-to-noise ratio for the measurements obtained in the Arctic is severely limited by interference of ice-reflected acoustic energy with the direct path. This is a limitation of the instrumentation that could be overcome in future experiments as discussed on page 6.4. This problem is compounded by the fact that amplitude scintillations focus on Fresnel sized disturbances, which are less energetic, and therefore harder to measure, than the scales observed using reciprocal travel-time scintillation analysis in Chapter 5. Nevertheless, the results obtained are encouraging; they demonstrate the applicability of amplitude scintillation analysis to the study of arctic boundary layers.

The measurements reported here are unique in several ways. Previous oceanic scintillation measurements were obtained in a tidal channel, while the ones described here probe the boundary layer beneath ice in the Arctic. In turbulent tidal channels, temperature and velocity microstructure play equally important roles as

acoustic scatterers [21]. In the arctic boundary layer, the ice cover maintains water temperature close to the freezing point, and temperature fine structure is negligible. Mixing is driven by buoyancy fluxes due to brine rejection during freezing, and by surface stress due to ice-relative current speed. As a result, there is some salinity fine structure, but it is velocity fluctuations that are primarily responsible for forward acoustic scatter (Section 6.3.1). The significance of this is that amplitude scintillation analysis in the arctic boundary layer results in direct estimates of dissipation rate, provided the acoustic frequency and range are chosen so that the first Fresnel zone is contained within the Kolmogorov inertial subrange.

In addition to one-way propagation data, reciprocal travel-time measurements were obtained during the arctic experiment. As discussed in Chapter 5, reciprocal travel-time scintillation analysis measures velocity variability, to the exclusion of other refractive index perturbations. Therefore, the simultaneous measurement of amplitude and reciprocal travel-time scintillations permits the separation of velocity fine structure effects on acoustic propagation from those of sound speed structure due to temperature and salinity fluctuations.

In this chapter, we first outline the theory that relates acoustic amplitude fluctuations on a receiving plane, with refractive index perturbations in the flow, for the weak scattering regime. After a brief description of the turbulent field and an introduction to some functions commonly used to describe amplitude fluctuations, we present a qualitative interpretation of amplitude scintillations. Some important theoretical results are quoted. Next, some practical considerations are examined, including important design parameters, and an estimate of refractive index variance in the arctic boundary layer. Finally, we use amplitude scintillation analysis to obtain an estimate of transverse velocity and to measure dissipation rate.

6.2 Theory

The theory of wave propagation through random media is well established for the weak scattering regime [36, 73]. Here, we outline some of the important definitions

and results necessary for the interpretation of amplitude scintillation measurements from the arctic experiment.

Statement of Problem

We consider transmitting and receiving transducers immersed in a turbulent flow, and separated by distance ℓ from each other. The intervening random fluctuations in acoustic refractive index produce a signal whose pressure amplitude $P(\mathbf{x},t)$ varies as a function of position and time. The forward problem consists in obtaining an expression that describes certain characteristics of $P(\mathbf{x},t)$, given some knowledge about the turbulent flow.

We begin this section with a statistical description of the turbulent flow. Then, we introduce functions that describe pressure-amplitude fluctuations. Next, we present a simple qualitative model describing amplitude fluctuations caused by refractive index variability of the flow. Finally, we state the exact solution of the problem and explore some numerical implications.

Notation

Wave propagation in random media has applications in several fields including meteorology, astronomy and oceanography. Advances of the theory in one field are often borrowed and applied in the others. This has lead to the coexistence of a disconcerting variety of notations.

In choosing notation, we have strived for economy and consistency throughout the dissertation. The random functions defined have zero mean; therefore, correlation instead of covariance functions can be used as discussed in Section 2.1.1. The wavenumber $k = 2\pi/\lambda$ is associated with scales of turbulence, and $k_a = 2\pi/\lambda_a$ is associated with the wavelength of the acoustic frequency.

6.2.1 Description of the Turbulent Field

Sound Speed Fluctuations

Refractive index is the acoustically significant property of ocean flows; it describes sound speed c as a function of position and time:

$$n(\mathbf{x}, t) = \frac{\langle c \rangle}{c(\mathbf{x}, t)}, \tag{6.1}$$

where the angle brackets denote ensemble averaging, and by definition $\langle n \rangle = 1$. The fractional sound speed fluctuation,

$$\mu = n - 1 \tag{6.2}$$

is a convenient parameter with zero mean, $\langle \mu \rangle = 0$, often used to study scattering effects of turbulent flows.

Spectral Description

The parameter μ is a random function best described by its statistical properties. The most useful ones are the variance, $\sigma_\mu^2 = \langle \mu^2 \rangle = R_\mu(0,0)$, and the space-time correlation function

$$R_\mu(\mathbf{x}, \mathbf{r}, t, \tau) = \langle \mu(\mathbf{x}, t)\, \mu(\mathbf{x} + \mathbf{r}, t + \tau) \rangle. \tag{6.3}$$

Assuming stationary and homogeneous turbulence, the Fourier transform pair,

$$R_\mu(\mathbf{r}) = \langle \mu(\mathbf{x}) \mu(\mathbf{x} + \mathbf{r}) \rangle = \int_{-\infty}^{\infty} \exp(i\mathbf{k} \cdot \mathbf{r}) \varphi_\mu(\mathbf{k})\, d\mathbf{k}, \tag{6.4}$$

and

$$\varphi_\mu(\mathbf{k}) = \frac{1}{(2\pi)^3} \int_{-\infty}^{\infty} \exp(-i\mathbf{k} \cdot \mathbf{r}) R_\mu(\mathbf{r})\, d\mathbf{r}, \tag{6.5}$$

is defined in a coordinate system moving with the mean flow velocity; $\varphi_\mu(\mathbf{k})$ is the spectral density of the refractive index, and $\mathbf{k}$ is a wavevector associated with scales of turbulence.

Structure Function

When the refractive index fluctuations are not stationary or homogeneous, they are more conveniently described by the structure function

$$D_\mu(\mathrm{x},\mathrm{r},t,\tau) = \langle[\mu(\mathrm{x},t) - \mu(\mathrm{x}+\mathrm{r},t+\tau)]^2\rangle. \tag{6.6}$$

If $\mu(\mathrm{x},t)$ has stationary increments and is locally homogeneous, (6.6) simplifies to $D_\mu(\mathrm{r},\tau)$, a function of displacement and delay. For stationary and homogeneous turbulence, the correlation and structure functions are trivially related by

$$D_\mu(\mathrm{r},\tau) = 2[R_\mu(0,0) - R_\mu(\mathrm{r},\tau)], \tag{6.7}$$

and

$$R_\mu(\mathrm{r},\tau) = \frac{1}{2}[D_\mu(\infty,\infty) - D_\mu(\mathrm{r},\tau)]. \tag{6.8}$$

Isotropic Turbulence

Isotropy implies that only the magnitude of r is important; the correlation and structure functions, (6.3) and (6.6), simplify to $R_\mu(r,\tau)$ and $D_\mu(r,\tau)$.

Kolmogorov Inertial Subrange

In Section 5.2.1, we introduced the Kolmogorov inertial subrange and its characteristic $k^{-5/3}$ energy spectrum. Temperature is usually the main source of sound speed variability in the ocean. Depending on conditions, and time and length scales of interest, temperature may behave as an advected, passive contaminant which closely follows the turbulent velocity behaviour. Under these circumstances, a -5/3 law is again predicted for the inertial subrange [47]. As a result, the refractive-index structure function is [73]

$$D_\mu(r) = C_\mu^2\, r^{2/3}, \tag{6.9}$$

and the spectral density of μ is

$$\varphi_\mu(k) = 0.033\, C_\mu^2\, k^{-11/3}, \tag{6.10}$$

where C_μ^2 is the structure parameter that characterizes the strength of refractive-index fluctuations.

Measurements made at the ice camp indicate that velocity fluctuations are the main source of refractive index variability in the boundary layer beneath ice (Section 6.3.1). For velocity fluctuations, the Kolmogorov inertial subrange extends through scales $l_o \ll \lambda < l_t \ll L_o$. The inner scale l_o is a function of dissipation rate ϵ, and kinematic viscosity ν [30]:

$$l_o = 2\pi(\nu^3/\epsilon)^{1/4}. \tag{6.11}$$

For seawater, $\nu \approx 1.8 \times 10^{-6}$ m^{2}s^{-1}, and we have measured $\epsilon \sim 10^{-7}$ m^{2}s^{-3}, therefore l_o is about 2 cm.

Medwin [47] gives an empirical expression for the transition scale l_t in the upper ocean as a function of depth z in meters,

$$l_t \sim 0.7 \exp(z/40), \tag{6.12}$$

where l_t is in m. For example, at a depth of 20 m (6.12) implies that $l_t \sim 1.2$ m. Expression (6.12) is based on mid latitude measurements at depths below 100 m. The arctic boundary layer is of course very different from the ice-free ocean, as surface waves and buoyancy fluxes are greatly attenuated by the presence of the ice. Therefore, (6.12) can only serve as a very rough estimate of the transition scale. The outer scale L_o represents the size of the largest turbulent eddies, usually of order of the depth or width of the flow.

6.2.2 Acoustic Amplitude Fluctuations

Log-Amplitude

The pressure-amplitude fluctuations of scattered acoustic energy are usually expressed in terms of the log-amplitude random variable

$$\chi = \ln(P/\langle P \rangle), \tag{6.13}$$

where P is the pressure-amplitude. Note that for $\chi \ll 1$, which holds in the weak scattering regime considered here, the log-amplitude is equal to the fractional pressure fluctuations, $\chi \approx P/\langle P \rangle - 1$, and has zero mean, $\langle \chi \rangle \approx 0$. The weak scattering regime is characterized by log-amplitude variance, $\sigma_\chi^2 = \langle \chi^2 \rangle$, less than about 0.3.

Spectral Description

To study the spatial and temporal variations of amplitude scintillation patterns, we construct the log-amplitude correlation function,

$$R_\chi(\mathbf{x}, \mathbf{r}, t, \tau) = \langle \chi(\mathbf{x}, t)\, \chi(\mathbf{x} + \mathbf{r}, t + \tau) \rangle. \tag{6.14}$$

Practical measurements for one transmitter-receiver pair yield the time-lagged autocorrelation of χ,

$$R_\chi(\tau) = \overline{\chi(t)\chi(t+\tau)} = 2 \int_0^\infty \cos(2\pi f \tau) F_\chi(f)\, df, \tag{6.15}$$

and the frequency spectrum

$$F_\chi(f) = 2 \int_0^\infty \cos(2\pi f \tau) R_\chi(\tau)\, d\tau, \tag{6.16}$$

such that

$$\int_0^\infty F_\chi(f)\, df = \frac{1}{2} R_\chi(0) = \frac{1}{2} \overline{\chi^2}; \tag{6.17}$$

the overbar denotes time-averaging, equivalent to ensemble averaging for an ergodic variable, and easier to measure. Assuming Taylor's frozen field hypothesis is applicable, the time-lagged autocorrelation is related to the spatial correlation function by (5.57), $R_\chi(r_1 = \overline{U}\tau) = R_\chi(\tau)$, where r_1 is a displacement parallel to the mean velocity vector $\overline{\mathbf{U}}$.

6.2.3 Qualitative Interpretation of Scintillation

In this section we present a qualitative description of pressure-amplitude fluctuations for an acoustic wave propagating through a turbulent medium. Both refraction and diffraction effects are considered. Following Tatarskii [73], an expression for the mean-square amplitude fluctuations, apart from a numerical coefficient, is derived from these simple qualitative considerations.

Refraction Effects

Consider a plane wave incident on a weak collecting lens with focal length f_o and radius r_o. On a receiving plane, parallel to the acoustic wavefront, and a distance x from the lens, the cross section of the beam is r_x, where $r_o/f_o = r_x/(f_o - x)$. If the pressure-amplitude is P_o before the lens, P_x at x, and there are no transmission losses, then $(P_o r_o)^2 = (P_x r_x)^2$. Therefore, the relative change in pressure-amplitude is

$$\frac{\delta P}{P_o} = \frac{P_x}{P_o} - 1 = \frac{r_o}{r_x} - 1 = \frac{x}{f_o - x}. \tag{6.18}$$

If $x \ll f_o$, then $\delta P/P_o \approx x/f_o$. Therefore, the largest focusing effect will be caused by lenses with the smallest focal length.

The focal length of a lens,

$$f_o = r_o/\mu, \tag{6.19}$$

depends on its radius of curvature r_o, and the fractional change of sound speed μ. Refractive index inhomogeneities due to turbulence act as lenses; in the inertial subrange, (6.6), (6.9) and (6.19) say that an inhomogeneity of size r is associated with refractive index perturbation $\mu \approx C_\mu r^{1/3}$, and focal length $f_o \approx r^{2/3}/C_\mu$. If l_o is the inner scale of turbulence, then the smallest and most effective lenses have $r = l_o$, and the acoustic ray is intercepted by approximately ℓ/l_o such lenses, where ℓ is the pathlength. The parameter x varies for each lens, but is of order

ℓ. Therefore, the mean square pressure-amplitude fluctuation at the receiver is approximately

$$\sigma_\chi^2 \approx \left\langle \left(\frac{\delta P}{P_o}\right)^2 \right\rangle \sim \left(\frac{C_\mu \ell}{l_o^{2/3}}\right)^2 \frac{\ell}{l_o} = \frac{C_\mu^2 \ell^3}{l_o^{7/3}}. \tag{6.20}$$

The description thus far is purely geometrical, *i.e.* it is valid for very short acoustic wavelengths, $\lambda_a \ll l_o^2/\ell$.

Fresnel Zone

The first Fresnel zone is the region where the pathlengths of scattered acoustic rays deviate from the unscattered pathlength by half a wavelength or less. The size of this zone is approximately $\sqrt{\lambda_a \ell}$ at midpath, where λ_a is the acoustic wavelength and ℓ is the pathlength. Due to diffraction effects, inhomogeneities smaller than the first Fresnel zone cannot be acoustically resolved at the receiver.

Diffraction Effects

Diffraction effects do not directly contribute to pressure-amplitude fluctuations at the receiver because the diffraction pattern from a weak collecting lens is roughly the same as that of a weak dispersing lens. However, when the size of the turbulent lenses is small compared to the first Fresnel zone, the lenses lose their ability to focus acoustic energy on the receiving plane, and have little effect on amplitude fluctuations. The smallest refractive index inhomogeneities which retain the ability to focus are roughly Fresnel sized; $r \sim \sqrt{\lambda_a \ell}$. Hence, the parameter l_o in the geometrical approximation for σ_χ^2, (6.20), must be replaced with $\sqrt{\lambda_a \ell}$:

$$\sigma_\chi^2 \sim C_\mu^2 k_a^{7/6} \ell^{11/6}, \tag{6.21}$$

where $k_a = 2\pi/\lambda_a$. In other words, the effect of all small scale inhomogeneities measuring less than $\sqrt{\lambda_a \ell}$ is essentially removed because of diffraction effects.

6.2.4 Quantitative Description of Scintillation

Correlation Function

For spherical waves (*i.e.* small projector diameter relative to the Fresnel size $\sqrt{\lambda_a \ell}$), in the weak scattering regime, the equation that relates the log-amplitude correlation function, $R_\chi(\mathrm{r}, \tau)$, with the spectral density of the refractive index fluctuations, $\varphi_\mu(\mathrm{k}, \mathrm{x})$, is [36, 73]

$$R_\chi(\mathrm{r}, \tau) = 2\pi k_a^2 \int_0^\ell \int_{-\infty}^{\infty} \exp\left[i\mathrm{k}_s \cdot \left(\frac{\mathrm{r}s}{\ell} - \mathrm{U}(s)\tau\right)\right] \varphi_\mu(\mathrm{k}_s, s) \sin^2\left(\frac{k_s^2 s(\ell - s)}{2k_a \ell}\right) d\mathrm{k}_s\, ds. \tag{6.22}$$

This is an integral, both along the acoustic path, $0 \leq s \leq \ell$, and over the two-dimensional wave number space, $d\mathrm{k}_s$, where k_s is a wavevector of the refractive index fluctuations in a plane transverse to the acoustic path. The first two terms of the integrand represent the contribution of a single Fourier component, k_s, of the refractive index field at path position s. These contributions are assumed to be uncorrelated; they are integrated over all wavenumbers to obtain refractive index screens, and all path positions to give the log-amplitude correlation function. Implicit in the argument $[\mathrm{r}s/\ell - \mathrm{U}(s)\tau]$ is the use of Taylor's frozen field hypothesis. The last term of the integrand measures the scattering efficiency of an irregularity with wavenumber k_s at position s; it accounts for the refraction and diffraction effects discussed in Section 6.2.3. This *filter* function emphasizes Fresnel-zone-sized disturbances. As a result, they are the ones that contribute most effectively to log-amplitude fluctuations.

If the significant scale sizes, $k_s \sim \sqrt{\lambda_a \ell}$, lie in a range where the spectral density of the refractive index fluctuations is isotropic, then $\varphi_\mu(\mathrm{k}, s) = \varphi_\mu(k, s)$, and (6.22)

can be simplified by integrating k_s over angles:

$$R_\chi(\mathbf{r},\tau) = 4\pi^2 k_a^2 \int_0^\ell \int_0^\infty J_o\left(k\left|\frac{\mathbf{r}s}{\ell} - \mathbf{U}(s)\tau\right|\right) k\varphi_\mu(k,s)\sin^2\left(\frac{k^2 s(\ell-s)}{2k_a\ell}\right) dk\,ds, \tag{6.23}$$

where J_o is the zero-order Bessel function of the first kind.

Log-Amplitude Variance

If the Fresnel size lies within the inertial subrange, the spectral density of the refractive index fluctuations is given by (6.10), and the variance of the log-amplitude is easily obtained from (6.23):

$$\sigma_\chi^2 = R_\chi(0,0) = 0.124\, C_\mu^2\, k_a^{7/6}\, \ell^{11/6}. \tag{6.24}$$

If the structure parameter C_μ^2 is not known, but an estimate of the refractive index variance σ_μ^2 is available, Medwin [47] suggested another expression for the log-amplitude variance,

$$\sigma_\chi^2 \sim \frac{\sqrt{\pi}}{10}\sigma_\mu^2\, k_a^2\, \ell\, \exp(z/40), \tag{6.25}$$

where z is the depth of the acoustic propagation path in m. This semi-empirical prediction is limited to the upper ocean ($z < 100$ m), and is based on data from mid latitudes. Nevertheless, it may prove to be a useful first order approximation when knowledge about a region is limited.

Frequency Spectrum

Clifford [9] used (6.23) to derive a temporal spectrum of log-amplitude fluctuations at a receiving point,

$$F_\chi(f) = 8\pi^2 k_a^2 \int_0^\ell \int_{2\pi f/U_\perp}^\infty k\varphi(k)[(kU_\perp)^2 - (2\pi f)^2]^{-1/2} \left[1 - \cos\left(\frac{k^2 s(\ell - s)}{k_a \ell}\right)\right] dk\, ds, \tag{6.26}$$

where $U_\perp$ is the mean flow speed perpendicular to the acoustic path. This equation is valid for spherical waves propagating through a weakly scattering medium, and an acoustic path length much longer than the outer scale of turbulence, $\ell \gg L_o$. For a Kolmogorov refractivity spectrum, (6.10), Clifford obtained an analytic solution for (6.26),

$$\begin{aligned} F_\chi(f) \;=\; & 2.19 \frac{k_a^{2/3} \ell^{7/3} C_\mu^2}{U_\perp} \left(\frac{f}{f_F}\right)^{-8/3} \Re\left\{1 - H\left[1, \frac{-5}{6}, \frac{3}{2}, \frac{-1}{3}, \frac{i}{4}\left(\frac{f}{f_F}\right)^2\right]\right. \\ & \left. - \frac{4}{11}\Gamma\left(\frac{-4}{3}\right)\left(\frac{f}{f_F}\right)^{4/3} H\left[\frac{1}{2}, 1, \frac{17}{6}, 1, \frac{i}{4}\left(\frac{f}{f_F}\right)^2\right]\right\}, \end{aligned} \tag{6.27}$$

where $f_F = U_\perp (2\pi\lambda_a \ell)^{-1/2}$ is the Fresnel normalization frequency, $\Re$ indicates the real component of the bracketed expression, $\Gamma(-4/3) \approx 3.05$ is the gamma function, and

$$H(a, b, c, d, z) = \sum_{n=0}^{\infty} \frac{\Gamma(a+n)\Gamma(b+n)\Gamma(c)\Gamma(d) z^n}{\Gamma(a)\Gamma(b)\Gamma(c+n)\Gamma(d+n) n!} \tag{6.28}$$

is the confluent hypergeometric function. The series in (6.28) is easily and quickly evaluated by noting that the first term of the summation is $h_o = 1$, and that each successive term can be obtained using the recursive formula

$$h_{n+1} = h_n \frac{(a+n)(b+n)z}{(c+n)(d+n)(n+1)}. \tag{6.29}$$

However, the convergence of (6.28) is slow for $f \gg f_F$, and the asymptotic form given below should be used instead. The asymptotic forms for the log-amplitude frequency spectrum are

$$F_\chi(f) = 0.191 \frac{k_a^{2/3} \ell^{7/3} C_\mu^2}{U_\perp} \left[1 + 0.119 \left(\frac{f}{f_F} \right)^{4/3} \right] : \qquad f \ll f_F, \tag{6.30}$$

and

$$F_\chi(f) = 2.19 \frac{k_a^{2/3} \ell^{7/3} C_\mu^2}{U_\perp} \left(\frac{f}{f_F} \right)^{-8/3} : \qquad f \gg f_F. \tag{6.31}$$

6.3 Practical Considerations

6.3.1 Refractive Index Variability

As discussed in Section 6.1, the sub-ice boundary layer has unique acoustical scattering properties. Refractive index variability in the upper ocean is often caused by velocity fine structure advecting passive scalars. These scalar quantities include temperature, salinity, and, near the open ocean surface, air bubbles. The component of velocity fine structure parallel to the acoustic propagation path is also responsible for apparent changes of the sound speed and forward acoustic scatter. Here, we estimate the variance of the fractional sound speed fluctuations, σ_μ^2, based on measurements obtained by M. G. McPhee (1989, personal communication) during the arctic experiment:

mean ice-relative velocity	$\overline{U}$	$\sim$	0.1 m/s
velocity standard deviation	$\sigma_u^2 = \overline{u_1^2}$	$\sim$	$(0.01 \text{ m/s})^2$
mean temperature	$\overline{T}$	$\sim$	-1.839 °C
temperature standard deviation	$\sigma_T^2 = \overline{(T - \overline{T})^2}$	$\sim$	$(10^{-4} \text{ °C})^2$
mean salinity	$\overline{S}$	$\sim$	34.12 ‰
salinity standard deviation	$\sigma_S^2 = \overline{(S - \overline{S})^2}$	$\sim$	$(10^{-3} \text{ ‰})^2$,

where the overbar denotes a 15 min averaging period. These data are typical of conditions observed on April 18, at the 8-m depth. A simple empirical equation

for sound velocity [6],

$$\begin{aligned} c &= 1449.2 + 4.6\,T - 0.055\,T^2 + 0.00029\,T^3 \\ &\quad +(1.34 - 0.010\,T)(S - 35) + 0.016\,z \end{aligned} \tag{6.32}$$

where c is the sound speed in ms^{-1}, T the temperature in °C, S the salinity in parts per thousand (‰), and z the depth in meters, is used to estimate the contributions of temperature, salinity and velocity fine structure to the refractive index variance of the medium:

$$\sigma_\mu^2(T) \approx \left(\frac{4.6\,\sigma_T}{\langle c \rangle}\right)^2 \sim 10^{-13}, \tag{6.33}$$

$$\sigma_\mu^2(S) \approx \left(\frac{1.35\,\sigma_S}{\langle c \rangle}\right)^2 \sim 10^{-12}, \tag{6.34}$$

and

$$\sigma_\mu^2(u) \approx \left(\frac{\sigma_u}{\langle c \rangle}\right)^2 \sim 10^{-10}. \tag{6.35}$$

Based on these numbers, we expect velocity fine structure to be the main source of forward scatter in the arctic boundary layer, a conclusion that is further supported by the results reported in Section 6.5.2.

6.3.2 Design Requirements

An acoustic scintillation instrument designed to exploit the theory outlined in Section 6.2 must satisfy several conditions; the most important requirements pertain to the choice of acoustic carrier and pathlength, the sampling rate, and the detection threshold.

It was pointed out in Sections 6.2.3 and 6.2.4 that Fresnel-sized refractive index disturbances are responsible for most of the log-amplitude variance. Therefore, through judicious choice of carrier frequency f_a and range ℓ, it is possible to emphasize the desired turbulence scales. During our arctic experiment, the choice

of the parameters, $f_a = 132.3$ kHz and $\ell = 200$ m, was such that scales of order $\sqrt{\lambda_a \ell} = 1.5$ m were emphasized. The specific carrier frequency was chosen because of transducer availability, as it is difficult to find an omnidirectional source at any higher frequency. Based on (6.12), this value lies just outside the inertial subrange, in the transition range, for the propagation depths of the experiment, d =8–20 m.

The second requirement is that of an adequate sampling rate to avoid aliasing. The dominant amplitude fluctuations have an observed period that is a function of their size and of the mean advection velocity transverse to the acoustic path,

$$\tau = \sqrt{\lambda_a \ell}/U_\perp. \tag{6.36}$$

For typical ice-relative advection velocity, $U_\perp = 0.1$ ms^{-1}, the dominant period of the amplitude scintillations is $\tau = 15$ s, and a sampling frequency greater than $2/\tau = 0.13$ Hz is necessary. The pulse repetition rate during our arctic experiment was 1.1 Hz, thus satisfying this requirement.

The last design parameter discussed here is signal to noise ratio (SNR). A rough estimate of the log-amplitude variance can be obtained from (6.25) and (6.35). Given $\sigma_\chi^2 \sim 10^{-3}$, the required SNR is approximately

$$\text{SNR} > -10 \log \sigma_\chi^2 \sim 30 \text{ dB}. \tag{6.37}$$

Therefore, signal-to-noise ratio greater than 30 dB for a filtered sampling rate of 0.13 Hz is necessary to observe log-amplitude fluctuations in the arctic boundary layer. The signal-to-noise ratio achieved during the arctic experiment (Section 4.2) is barely adequate for the observation of amplitude scintillations. Nevertheless, some useful results have been obtained (Sections 6.4 and 6.5).

6.4 Measurement of Transverse Velocity

Reciprocal transmission, as discussed in Chapter 5, provides the flow component along the propagation path. The drift of the scintillation pattern on a receiving plane contains information about the perpendicular flow component. Several

techniques for measuring crosswind from optical scintillations have been suggested [77]; some of these, including delay to the peak and slope at zero time lag of the cross-correlation function have been adapted to the study of ocean flows using acoustic scintillation analysis [20]. During the arctic experiment, high-frequency log-amplitude fluctuations were masked by noise due to limitations of the instrumentation. For this reason, only the peak delay method can be applied.

In Fig. 6.1 we compare time series of log-amplitude, $\chi(t)$, for two parallel horizontal acoustic paths of length $\ell = 211$ m, orientation 344° T and depth 8.4 m. The two paths are separated by $\rho = 56.3$ cm, approximately one third of the Fresnel size, $\sqrt{\lambda_a \ell} = 1.5$ m. During the time of the measurement, the mean flow relative to the ice at the 8.4 m depth has speed 11 cm/s and direction 55° T; therefore, the component of flow perpendicular to the acoustic paths is $U_\perp = 10.4$ cm/s.

Four minute time series of $\chi(t)$ obtained on April 18, 1989, for the upstream and downstream acoustic paths are displayed in Figs 6.1a and b respectively. The time series are noisy, and there appears to be little correlation between the two. Segments of the log-normalized sound intensity of 256 points length are Fourier transformed and normalized by the Fresnel translation frequency $f_F = U_\perp (2\pi\lambda_a \ell)^{-1/2}$, in order to determine the spectral properties of the time series. In Fig. 6.1c we display a seven hour average of the acoustic log-amplitude power spectrum $F_\chi(f)$ for the upstream acoustic path normalized by f/f_F so as to allow direct comparison with Fig. 9 of Farmer *et al.* [21]. The dotted lines enclose the 95% confidence interval of the spectrum. The dashed line is a constant fitted to the high frequency noise floor. We attribute this noise to interference from the ice-reflected acoustic signal. Though the measurements are an order of magnitude more sensitive than those made by Farmer *et al.* in Cordova Channel, the peak at the Fresnel wave number predicted by the propagation theory is barely above the noise level (Section 6.5.2). This may be explained by the much weaker refractive index variability in the ice-water boundary layer as discussed in Section 6.3.1.

In Fig. 6.1d, we plot the coherence function between the log-amplitude spectra

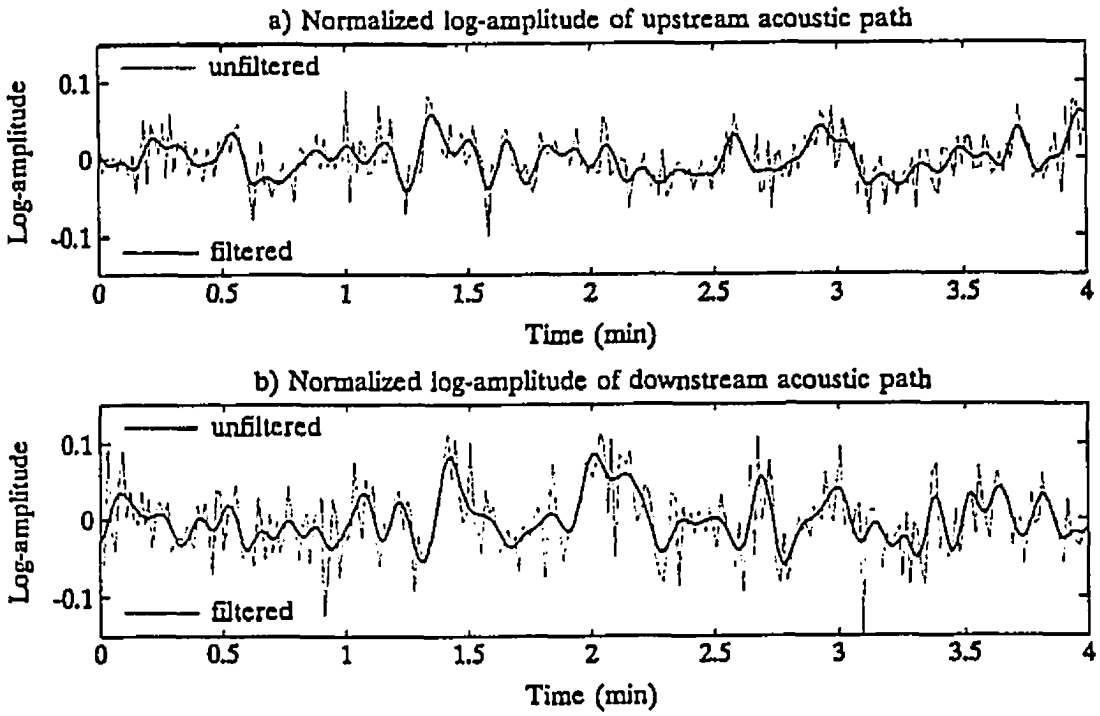

Figure 6.1: Comparison of log-amplitude time series for two adjacent horizontal acoustic paths. (a) Normalized log-amplitude $\chi(t)$ of the upstream acoustic path, length $\ell = 211$ m, orientation 344° T and depth 8.4 m. (b) $\chi(t)$ for the adjacent parallel acoustic path located $\rho = 56.3$ cm downstream of the first path. (c) Normalized spectrum $F_\chi(f)f/f_F$ of the upstream acoustic path. (d) Coherence between the two paths. (e) Autocovariance of the two paths. (f) Cross-covariance between the two paths.

of the two adjacent acoustic paths. For $f/f_F > 6$, the two time series are uncorrelated; at lower frequencies there is some coherence between the two time series. This indicates that a certain percentage of the observed fluctuations are caused by refractive index fine structure that remains coherent as it is advected past the two acoustic paths. We lowpass filter the log-amplitude time series to remove what is known to be measurement noise and plot the resulting time series and spectrum as solid lines in Figs 6.1a, b and c respectively.

In Fig. 6.1e and f, we plot the normalized log-amplitude autocovariance and cross-covariance of the filtered time series for the four minute segments displayed in Fig. 6.1a and b. Because the high frequency end of the spectrum is missing, the

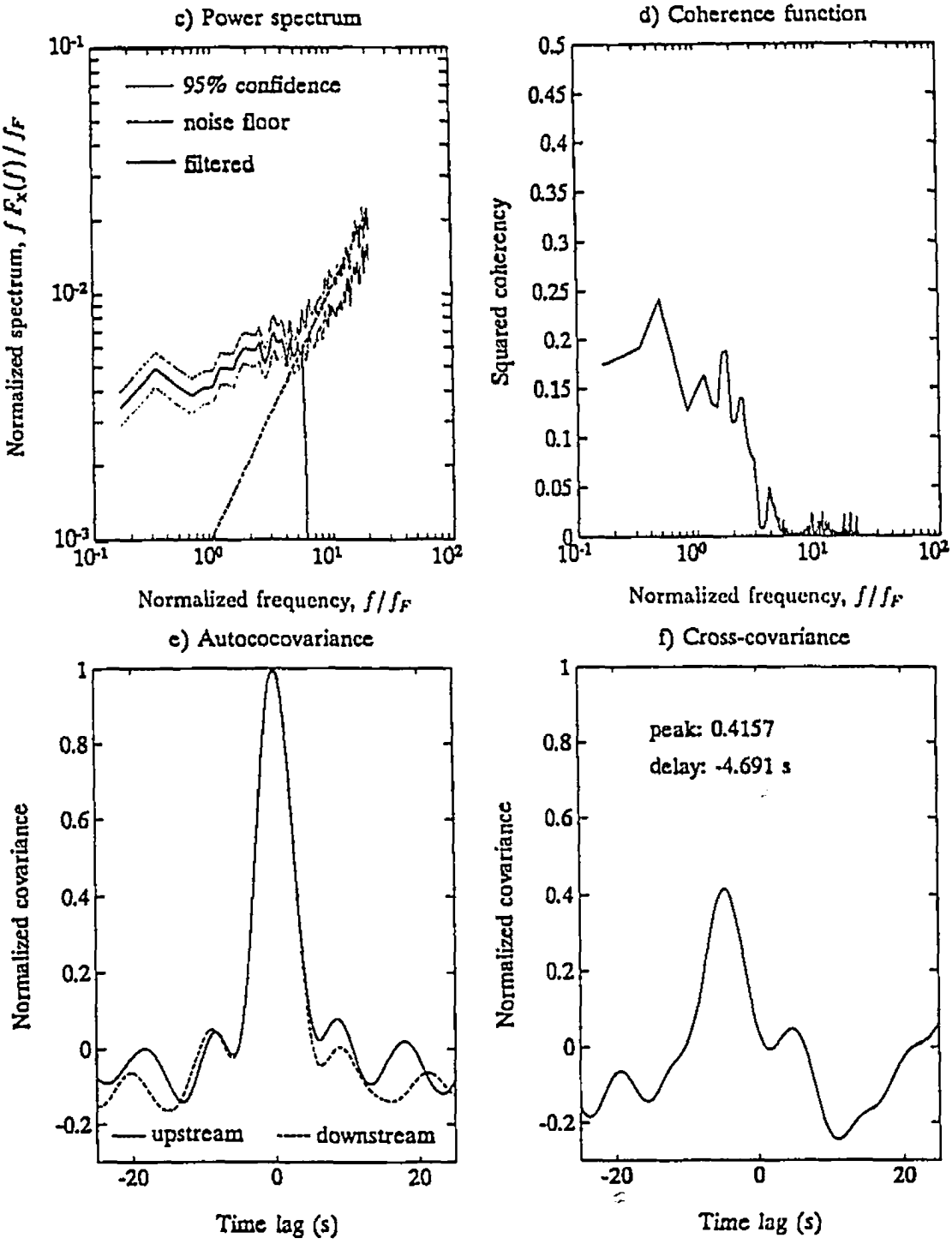

Figure 6.1: (*Continued*)

width of the autocovariance peak at zero lag has no physical significance; it depends on the characteristics of the applied filter. For the same reason, the slope at zero lag of the cross-covariance cannot be used to determine flow speed. However, there is some similarity between the autocovariance function of the two paths, which indicates that the refractive index fine structure remains somewhat coherent as it is advected past the two parallel acoustic paths. Therefore, we may use delay to the peak of the cross-covariance function, $\tau_p = -4.7$ s, to estimate the horizontal velocity component normal to the acoustic paths, $U_\perp \approx -\rho/\tau_p = 12$ cm/s.

Figure 6.2 shows time series of horizontal velocity determined using τ_p along one side of the triangular array and velocity obtained using reciprocal transmission along the other two sides of the array. The amplitude scintillation velocity estimates are based on 4, 20 and 40 min time series. The 4-min averages do not provide a good estimate of transverse velocity because the high-frequency end of the spectrum is not available. However, estimates of velocity based on 20 and 40-min averages seem to fit those obtained with reciprocal transmission reasonably well. Despite the limitations of eddy decay, a flow-dependent weighting function, and the difficulty in measuring small currents using the peak delay processing scheme, the measurements shown here demonstrate the viability of the scintillation technique for use in the ice-water boundary layer.

The signal to noise ratio was dominated by interference from the ice reflected path. However, a modest change in data recording (i.e. continuously recording both the direct and reflected arrivals, or including longer guard sequences as detailed in Section 3.2.1) would have greatly improved results, allowing accurate scintillation flow measurements based on the full spectrum.

6.5 Measurement of Dissipation Rate

Much of the turbulent energy dissipation in the arctic boundary layer occurs very close to the base of the ice, where accurate estimates of mean dissipation rate are difficult to obtain. One of the problems is the patchiness and intermittency of

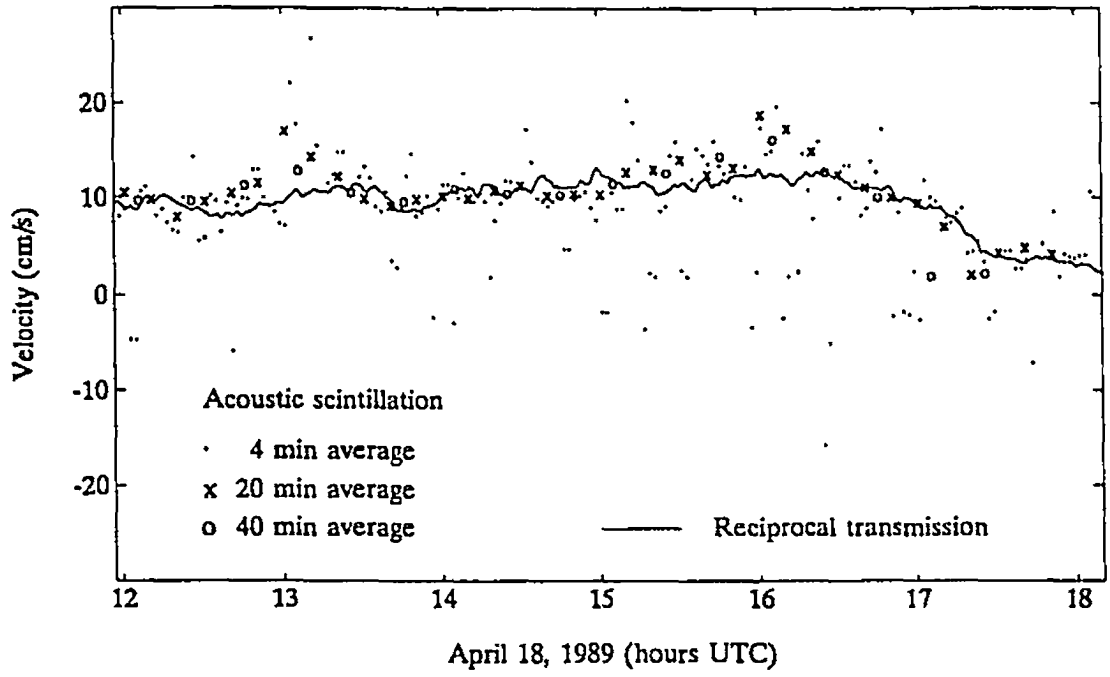

Figure 6.2: Time series of horizontal velocity determined using delay to the peak of the cross-covariance function, τ_p, compared to velocity measurements obtained using reciprocal transmission.

turbulence discussed in Section 5.3.4. A second problem is that point measurements may not be representative of the average properties of the boundary layer because of the presence of ice keels which change local dissipation rate. Finally, shear microstructure profilers cannot measure ϵ adequately in the first 12 m because of instrument vibration following release [61]. Rising profilers can overcome this limitation, but they are hard to operate through the ice.

Here, we use reciprocal travel time and amplitude scintillation analysis to obtain two independent estimates of mean dissipation rate at the 8.4 m depth, *i.e.* approximately 6 m below the bottom of the ice cover. This value is then compared to estimates of dissipation rate obtained with a shear microstructure profiler. For the analysis, we have chosen the same data segment as that of Section 6.4. The reason for this choice is that the mean ice-relative velocity is almost constant during this 7-hour period. Given an overturning time scale of order 1 hour [61], this

should result in fairly good statistical averages.

6.5.1 Reciprocal Travel Time Scintillation

We begin by estimating mean dissipation rate, ϵ, using reciprocal travel-time scintillation measurements and the method described in Section 5.3.4. Fig. 6.3 is the spectrum of line-averaged horizontal velocity fluctuations for the 7-hour period. The spatial spectrum displayed is obtained from the frequency spectrum using Taylor's frozen field hypothesis, (5.58). A line of slope -8/3 is fitted to the wavenumber range corresponding to 3–7 m scales, because smaller scales are masked by mooring motion (peak at $k_1/2\pi \sim 0.8$ m^{-1}), and white noise due to interference from the ice-reflected path. As we did in Section 5.3.4, we assume that for horizontal velocity fluctuations the $k_1^{-8/3}$ range extends outside the isotropic inertial subrange with the *correct* Kolmogorov constant. Equations (5.12), (5.15) and (5.30) are used to obtain the mean dissipation rate, $\epsilon \approx 2.7 \times 10^{-7}$ W/kg.

6.5.2 Amplitude Scintillation

From the rough calculations of Section 6.3.1, we expect velocity fine structure to be the main cause of forward acoustic scatter in the arctic boundary layer. For this reason, amplitude scintillation measurements provide another estimate of dissipation rate.

Scattering due to Velocity Fluctuations

The effective refractive index spectral density due to velocity fine structure is [73]

$$\varphi_\mu(k) = \frac{E(k)\cos^2(\vartheta/2)}{4\pi c^2 k^2}, \tag{6.38}$$

where $E(k) = A\epsilon^{2/3}k^{-5/3}$ is the three-dimensional energy spectrum (5.15), ϑ is the scattering angle, and c is the mean sound speed; the factor c^2 converts velocity

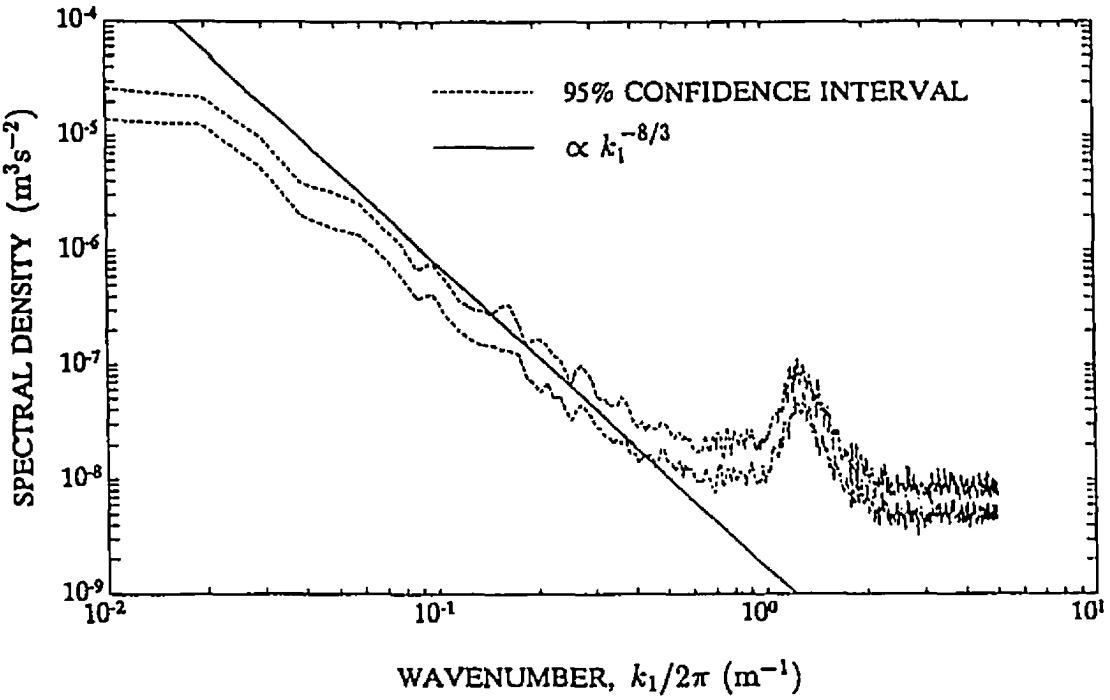

Figure 6.3: Spectral density of line-averaged horizontal velocity, pathlength ℓ = 211 m, orientation 344° T and depth 8.4 m. The spectrum represents a 7-hour average starting at 1155 UTC, 18 April 1989.

fluctuations to sound speed fluctuations. From (6.38), it is clear that velocity fluctuations do not contribute to backscatter ($\vartheta = 180°$), a direct consequence of the incompressibility in the turbulent flow. For forward acoustic scatter, the effective refractive index structure parameter is

$$C_\mu^2 = \frac{2.41}{c^2} A c^{2/3}. \tag{6.39}$$

This result is obtained by comparing (6.10) with (6.38).

Log-Amplitude Spectrum

Fig. 6.4 is the frequency spectrum of log-amplitude fluctuations for the same time period and acoustic path as Fig. 6.3. The spectrum is normalized by f/f_F, where $f_F = U_\perp(2\pi\lambda_a\ell)^{-1/2}$ is the Fresnel translation frequency. Equations (6.27) and

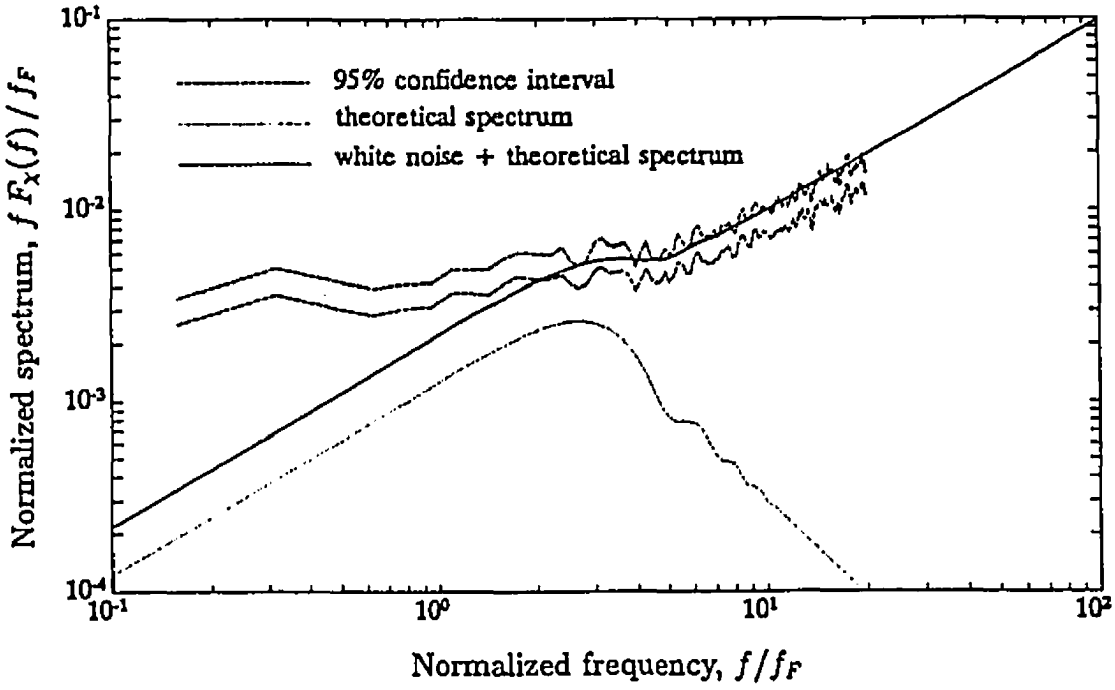

Figure 6.4: Frequency spectrum of log-amplitude fluctuations normalized by f/f_F, where $f_F = U_\perp(2\pi\lambda_a\ell)^{-1/2}$ is the Fresnel translation frequency. The spectrum corresponds to the same time period and acoustic path as Fig. 6.3. The theoretical spectrum is obtained for an isotropic inertial subrange, and for dissipation rate $\epsilon = 2.7 \times 10^{-7}$ W/kg obtained in Section 6.5.1. The white noise added to the theoretical spectrum is at a level consistent with that observed at high frequency.

(6.39), with $\epsilon = 2.7 \times 10^{-7}$ W/kg, are used to predict the shape of the spectrum under the assumption of an isotropic inertial subrange. White noise is added to this theoretical spectrum, at a level consistent with the noise floor observed at high frequency. The measured and predicted spectra agree in the vicinity of the Fresnel maximum, $f/f_F = \sqrt{2\pi}$. For lower frequencies, the assumption of an isotropic inertial subrange does not hold, and we do not expect the measured and the predicted spectra to correspond. The correspondence between the measured and predicted spectral levels in the vicinity of the Fresnel maximum leads us to three important conclusions. First, as expected, velocity fine structure is the principal cause of forward acoustic scatter in the arctic boundary layer during our measurements; the contribution from temperature and salinity fluctuations is negligible. Second, the

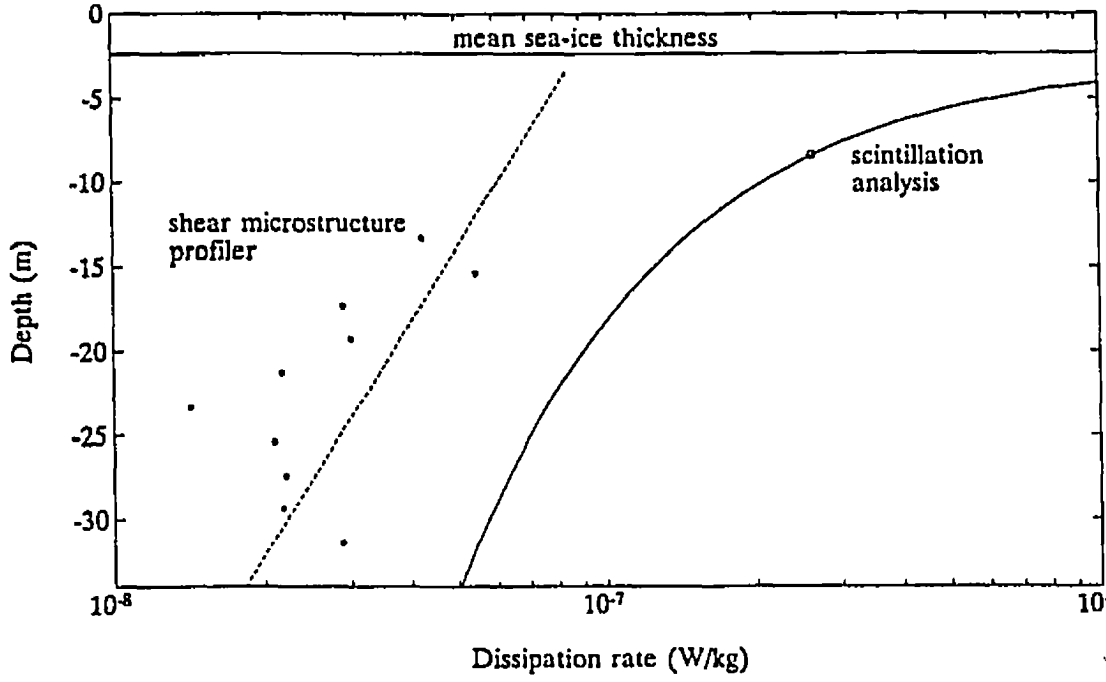

Figure 6.5: Dissipation rate as a function of depth from scintillation analysis (circles), and from shear microstructure profiles (asterisks). The data points are 7-hour averages starting at 11:55 UTC, 18 April 1989. The microstructure profiler data is also averaged over 2-m depth bins The dashed line is an exponential fit to the profiler estimates of ϵ, and the solid line is an estimate of $\epsilon(z)$ based on scintillation analysis and the assumption of a logarithmic surface layer extending out to 35 m depth.

assumption of an isotropic inertial subrange appears to be reasonable at least up to the Fresnel size $\sqrt{\lambda_a \ell} = 1.5$ m at the 8-m depth. Finally, we have obtained two independent estimates of mean dissipation rate that agree well with each other, using reciprocal travel-time and amplitude scintillation analysis.

6.5.3 Shear Microstructure Profiler

It is interesting to compare the value of mean dissipation rate obtained using scintillation analysis, with the profiles obtained by Padman and Dillon [61] using a shear microstructure probe. Dissipation rates as a function of depth are displayed on Fig. 6.5. The shear microstructure profiler measurements are only reliable below

about 12 m because of instrument vibration following release. The dissipation rate measured with the scintillation apparatus at the 8.4-m depth is roughly one order of magnitude greater than dissipation rates obtained with the shear profiler. This indicates that much of the energy dissipation occurs very close to the base of the ice, in the region that is not resolved by the profiling instrument. To determine the contribution to the depth-integrated dissipation rate,

$$\bar{\epsilon} = \int_0^D \epsilon(z)\, dz, \tag{6.40}$$

from the unresolved surface layer, 0 m $< z <$ 12 m, Padman and Dillon [61] assumed that the dissipation rate was exponentially decaying,

$$\epsilon(z) = \alpha \exp(-\beta z), \tag{6.41}$$

consistent with the decay scale found in the resolved portion of the profile, 12 m $< z < D$, where D is the mixed layer depth. The dashed line on Fig. 6.5 is an exponential fit to the profiler dissipation data. The solid line is an estimate of dissipation rate obtained from scintillation measurements and by assuming a constant stress surface layer as discussed in Section 2.2.2. Using turbulence clusters deployed at the center of the scintillation array, M. G. McPhee (1993, personal communication) also measured shear production [45] and energy dissipation rates that were consistently higher than those reported by Padman and Dillon [60]. The high dissipation rates measured by McPhee and by the scintillation apparatus may be the result of enhanced local turbulence due to pronounced bottom topographic features (Fig. 2.4).

6.5.4 Discussion

The estimated energy dissipation rate, $\epsilon = 2.7 \times 10^{-7}$ W/kg, obtained in Sections 6.5.1 and 6.5.2, was the result of measurements made at the 8.4 m depth.

This is sufficiently close to the bottom of the ice, $z \approx 6$ m, so that useful estimates of turbulent stress near the surface, $\tau_o = 0.08$ ntm^{-2}, drag coefficient, $C_D(6\text{ m}) = 0.006$, and roughness length, $z_o = 0.05$ m, can be made using surface layer approximations, (2.35), (2.36) and (2.38), introduced in Section 2.2.2. These values are consistent with previous measurements under multiyear pack ice [44], $0.002 < C_D(6\text{ m}) < 0.01$ and $0.002\text{ m} < z_o < 0.1$ m.

Under steady state conditions, the atmospheric stress exerted on the ice is balanced by the momentum flux entering the water (oceanic drag on the ice), a term due to planetary rotation (normal to the velocity of the ice), and the gradient of internal ice stress [44]. For a first order analysis, we neglect internal ice stress and the Coriolis term, and assume that the magnitude of atmospheric stress is roughly equal to the magnitude of oceanic stress near the ice. During the dissipation measurements, a steady northerly wind, $\overline{U_a}(2.82\text{ m}) = 7$ ms^{-1}, was recorded [28]. For the measured atmospheric conditions of -17°C, 1.03 bar and 72% relative humidity, the density of air above the ice is 1.4 kgm^{-3} [78]. We use the surface layer approximations of Section 2.2.2 to estimate the drag coefficient, $C_a(10\text{ m}) = 9.5 \times 10^{-4}$, and roughness length, $z_a = 2.3 \times 10^{-5}$ m, associated with momentum transfer between the atmosphere and the ice. These estimates are at the lower end of values previously measured over pack ice [7], $8.3 \times 10^{-4} < C_a(10\text{ m}) < 2.3 \times 10^{-3}$ and $10^{-5}\text{ m} < z_a < 2.4 \times 10^{-3}$ m, and the surface drag coefficient is lower than typical values ($\sim 1.3 \times 10^{-3}$) observed over open ocean. This may be an indication of significant internal stress gradient in the ice. Padman *et al.* [62] point out that diurnal tidal currents in the vicinity of the Yermak Plateau are enhanced by plateau topography. These tidal currents cause stress divergence at the base of the ice which greatly exceeds the typical divergence of the surface wind stress. Therefore, the tides may be responsible for the anomalously deep mixing layers observed under the ice camp, and for introducing internal stress gradients causing local deformations of the ice.

The kinetic energy flux from the ice to the ocean is proportional to ρu_*^3, where ρ is seawater density and u_* is friction velocity as defined in Section 2.2.2. Padman and Dillon [61] estimated the proportionality constant by assuming that all kinetic energy input at the surface is dissipated locally, and that buoyancy effects are negligible. They used the approximation discussed in Section 6.5.3 to estimate the depth-integrated dissipation rate, $\bar{\epsilon}$, and found that

$$\bar{\epsilon} \approx 2.4\, \rho u_*^3. \tag{6.42}$$

This may be compared to proportionality constants of 4 and 6 obtained from open ocean studies by Oakey and Elliott [58] and Dewey and Moum [15], respectively. The lower value in the Arctic may in part result from the unique mechanism of momentum transfer between the ice and the mixed layer, and from the absence of surface waves or direct interaction between the atmosphere and the ocean. Based on data comparison in Section 6.5.3, Fig. 6.5, we suggest that another possible cause for the low proportionality constant may be that energy dissipation rate is underestimated by profiler data because the measurements are not representative of true areal average, or because the unresolved near-surface dissipation rates are much higher than approximation (6.41) made in [61].

6.6 Summary and Conclusions

Though a limitation of our signal-recording scheme restricts the accuracy of the scintillation measurements, the present results demonstrate the usefulness of amplitude scintillation analysis for the study of the arctic boundary layer. We find that velocity fine-structure is the principal cause of forward acoustic scatter at the 8-m depth. This permits a direct estimation of energy dissipation rate from amplitude scintillation measurements. By combining reciprocal travel-time and amplitude scintillation analysis, we obtain both the along-path and the transverse component of the mean flow velocity. Minor modifications to the instrumentation

would provide the full spectrum, and appropriate analysis would allow excellent scintillation flow measurements.

Chapter 7

Surface Waves

7.1 Introduction

In Chapters 5 and 6 we discussed the measurement of velocity and refractive index fine structure; the scales considered were small compared to the dimensions of the acoustic array, $\lambda \ll \ell$. The incoherence of flow disturbances along the measuring baseline translates into a spectral attenuation proportional to $1/k_1\ell$ at high wavenumbers instead of the $1/(k_1\ell)^2$ expected for coherent events; phase information is lost, but it remains possible to infer the spectral properties of sound speed and velocity fine structure. In Chapters 7 and 8, we discuss flow disturbances with scales relatively large compared to the dimensions of the acoustic array, $\lambda \gg \ell$, and which remain coherent along the measuring baseline. We exploit the spatial filtering properties of the array (Section 4.5.2) to detect surface and internal waves that have amplitudes well below the resolution of conventional current meters. In this chapter, we present concurrent measurements of ice tilt and path-averaged horizontal velocity fluctuations due to surface gravity waves.

7.2 Background

Swell from the open ocean propagates into the Arctic as flexural-gravity waves [76]. Scattering at the ice edge damps high frequency swell. In addition, leads, irregularities in the ice and plastic creep dissipate swell energy within the pack ice,

attenuating short wavelengths more strongly than long ones. For these reasons, the ice acts as a lowpass filter whose cutoff frequency decreases with increasing distance from the open ocean, allowing only low frequencies to reach the central pack ice.

During the arctic experiment, horizontal velocity fluctuations caused by swell were very weak ($\sim 10^{-4}$ ms^{-1}) because of the distance ($\sim$ 200 km) separating the ice camp from the open ocean. This signal is masked by turbulent velocity fluctuations, and well below the resolution of conventional current meters. Swell this far away from the ice edge can be observed with tiltmeters, strainmeters and accelerometers deployed on the ice, but it has never before been reported on current meter records. Typical surface wave periods measured at the ice camp range from 20 to 50 s and correspond to wavelengths of 600 to 4000 m. At these wavelengths, the ice cover exerts little influence on the propagation of the waves, and the dispersion relation of surface gravity waves is applicable [64], namely

$$\omega^2 = gk \tanh kh, \tag{7.1}$$

where $\omega = 2\pi f$ is the radial frequency, $k = 2\pi/\lambda$ is the wavenumber, $g = 9.8$ ms^{-2} is the acceleration due to gravity, and h is the ocean depth. For typical depths measured during the experiment (Fig. 2.5), $2h > \lambda$ and (7.1) simplifies to

$$\omega^2 = gk. \tag{7.2}$$

7.3 Ice Tilt

During the experiment, swell caused tilt fluctuations of order of a few μrad at periods ranging from 20 to 50 s [14]. Typical spectra are plotted on Fig. 7.1. The north-south tilt fluctuations at frequencies associated with flexural-gravity waves are more energetic than the east-west fluctuations; this is an indication of the origin and propagation direction of the waves, *i.e.* most of the wave energy originates from the open ocean, roughly a few hundred kilometers south of the ice camp.

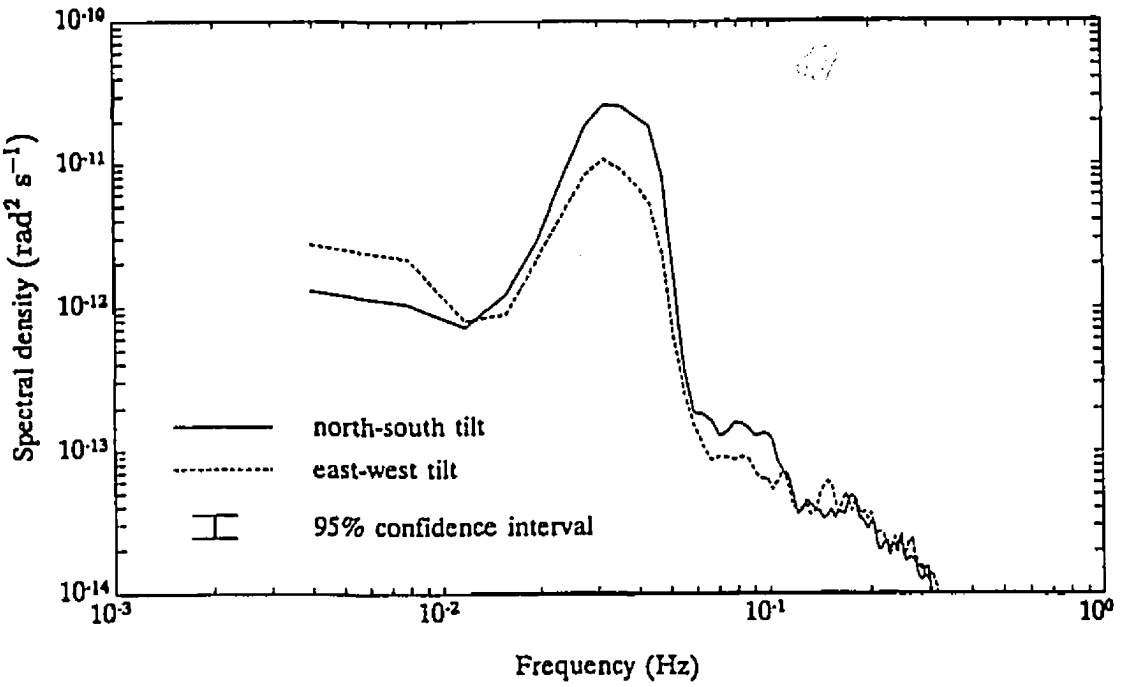

Figure 7.1: North-south and east-west spectra of tilt fluctuations from a five-hour record starting at 1300 UTC, 10 April 1989.

Czipott and Podney [14] determined the range of headings of swell impinging on the tiltmeter by cross spectral analysis of the two orthogonal axes. They found that short period swell ($\sim$ 20 s) comes predominantly from the eastern Fram Strait ($\sim$ 195° T), where it passes through less ice (Fig. 2.1); long period swell ($\sim$ 50 s) comes mainly from the western Fram Strait ($\sim$ 220° T), as it can travel longer distances with less attenuation. Finally, it must be pointed out that the analog lowpass filters used prior to digitization of the tilt data introduce a frequency-dependent phase shift, and that there is a calibration uncertainty which translates in a 2–4 factor error margin for tilt-amplitude at the frequencies considered here; this complicates comparison of tilt measurements with other data.

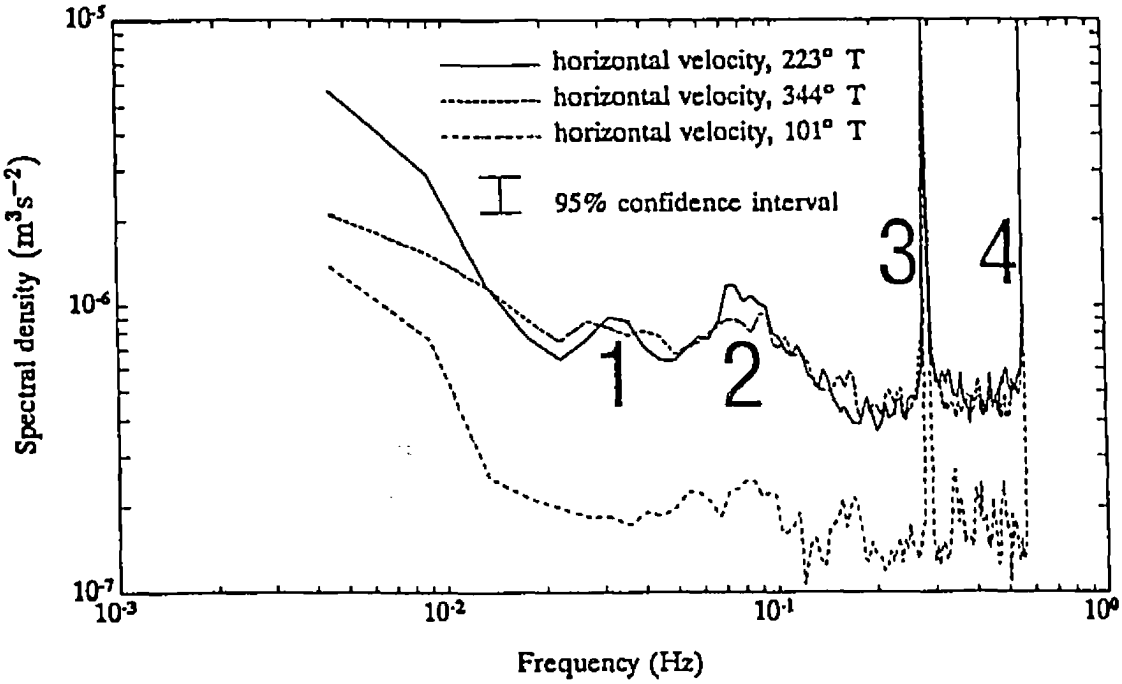

Figure 7.2: Line-averaged horizontal velocity spectra for each of the three measuring baselines of the acoustic array at the 20-m depth from a five-hour record starting at 1300 UTC, 10 April 1989.

7.4 Horizontal Velocity

Spectra of line-averaged horizontal velocity, for each of the three acoustic paths at the 20-m depth, are displayed on Fig. 7.2 for the same time period as that of Fig. 7.1. The spectra are five-hour averages starting at 1300 UTC, 10 April 1989 (day 100). During this period the mean ice-relative current speed at the 20-m depth is 6 cm/s in a southward direction, and the turbulence intensity is low (Fig. 5.10). The low level of turbulence maximizes the possibility of detecting swell with the acoustical current meter. The following comments can be made about the spectra of Fig. 7.2.

- The energetic spikes labeled 3 and 4 at half-Nyquist (0.29 Hz) and Nyquist (0.57 Hz) are caused by a periodic clock synchronization problem of the sonars. This problem is associated with the asynchronous resetting of each

sonar between transmissions (Section 3.1), and can be disregarded for the present analysis.

- The noise floor at high-frequency is caused by interference of the reflected path with the direct path. During the period considered here, the 101° T sonic path (the one under smooth ice) happens to be the quietest of the three paths; a possible explanation for this is presented in Section 7.6.

- Spectral peaks bearing label 2 and centered at 0.08 Hz result from relative motion of the moorings during each reciprocal transmission. The peaks are located at lower frequency than that of Fig. 4.3 because of the deeper deployment depth (20 vs 8 m), and are four times less energetic because of decreased turbulence intensity.

- Turbulence is responsible for spectral energy detected below 20 mHz, as discussed in Chapter 5.

- An unaccounted-for spectral peak marked by 1, which is above the 95% confidence level, is observed at 0.03 Hz in the 223° T spectrum (solid line).

We attribute the observed 33 mHz spectral peak to low frequency surface gravity waves of period $\approx$ 30 s, and use the tilt measurements to support this assertion in Section 7.5.

7.5 Comparison of Tilt and Horizontal Velocity

For a deep ocean and thin ice, relative to the wavelength of the flexural-gravity waves, *i.e.* when the ice and the bottom are not "seen" by the waves, dispersion relation (7.2) is applicable. For the case of a surface wave with elevation

$$\eta(\mathbf{x},t) = \eta_o \cos(\mathbf{k}\cdot\mathbf{x} - \omega t), \tag{7.3}$$

the horizontal velocity component parallel to the wavevector for deep water is [64]

$$u_h(\mathbf{x},t) = \omega\eta_o \exp(-kz)\cos(\mathbf{k}\cdot\mathbf{x} - \omega t), \tag{7.4}$$

at depth z below the surface. Near the surface, (7.4) simplifies to

$$u_h = \omega\eta. \tag{7.5}$$

Ice tilt τ is then related to surface displacement and horizontal velocity by

$$\tan\tau = \nabla_h \eta = \frac{1}{\omega}\nabla_h u_h, \tag{7.6}$$

where ∇_h is the horizontal gradient operator. For small surface displacements relative to the wavelength, (7.6) yields

$$\tau_o = k\eta_o = \frac{k}{\omega}u_o, \tag{7.7}$$

where τ_o, η_o, and u_o are the amplitudes of ice tilt, surface displacement, and horizontal velocity, respectively. Equations (4.8), (4.12) and (7.7) relate tilt and the path-averaged horizontal velocity fluctuations, $\tilde{u}_\theta$, due to surface waves and measured by the acoustical current meter near the surface:

$$\frac{|\tilde{u}_\theta|}{\tau_o} = \frac{\omega}{k}\frac{\sin(\mathrm{k}\cdot\ell/2)}{k\ell/2}, \tag{7.8}$$

where ℓ is the averaging baseline.

Tilt measurements establish that long period swell is roughly aligned with the 223° T acoustic path (Section 7.3). Equation (7.8) says that this path should therefore be the most sensitive to the passage of surface waves. The 223° T line-averaged horizontal velocity spectrum is redrawn on Fig. 7.3 along with a prediction based on (7.8) and the tilt measurements. Both the measured and the predicted spectra of line-averaged horizontal velocity exhibit a peak at 33 mHz. There is some discrepancy in the spectral levels, but that may be caused by additive noise and by the uncertainty in the calibration of the tilt measurements (Section 7.3).

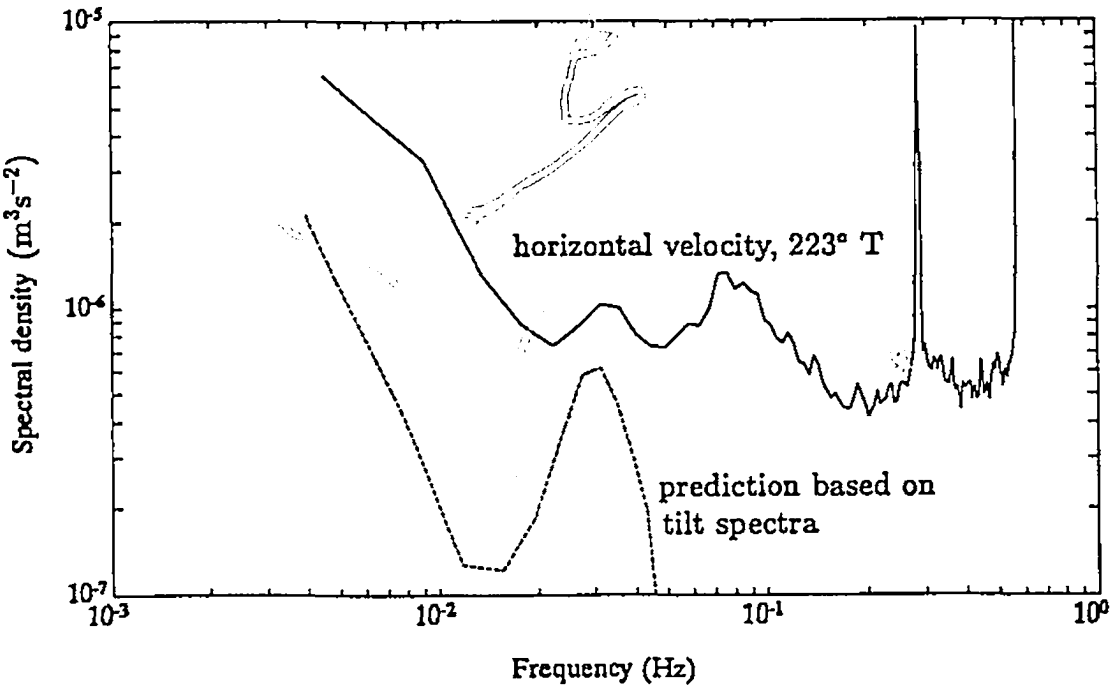

Figure 7.3: Line-averaged horizontal velocity spectrum for measuring baseline 223° T at the 20-m depth from a five hour record starting at 1300 UTC, 10 April 1989. A prediction of horizontal velocity caused by surface gravity waves based on tilt measurements is also drawn.

7.6 Mooring Motion

Based on the observed propagation direction of surface waves, and the low level of turbulence, one can conjecture why the noise level of the 101° T path in Fig. 7.2 is 2.5 times less than that of the other two paths. As discussed in Section 4.3, uncertainty in the measured acoustic travel time is principally caused by interference from the ice-reflected path and by relative mooring motion. The spectra of Fig. 7.2 suggest that the northern mooring common to acoustic paths 223° T and 344° T moves substantially more than the other two moorings. Due to the small ice-relative current speed and the low turbulence level during the period considered here, we speculate that surface waves are the main driving force responsible for the motion of the northern mooring, which is a 3-m long horizontal bar suspended 20 m below the ice transverse to the propagation direction of the waves.

The other two moorings are oblique to the wave vector and hence less sensitive to the passage of the waves. The preceding discussion suggests that mooring motion measured acoustically may be used as an exceptionally sensitive detector of velocity at frequencies neighboring mechanical resonance. Furthermore, mooring design and deployment parameters can be chosen to emphasize a desired direction and scale.

7.7 Summary and Conclusions

The detection of horizontal velocity associated with surface waves is an example of the sensitivity and spatial filtering property of the acoustical current meter we deployed in the Arctic. The velocity disturbance caused by the waves is of order 10^{-4} ms^{-1} and cannot be detected by point current measurements both because the disturbance is well below the resolution of conventional current meters, and because it is masked by turbulent velocity fluctuations. For mean advection velocity of 6 cm/s, 2 m sized turbulent eddies with characteristic velocity of 10^{-3} ms^{-1} are responsible for 33 mHz horizontal velocity fluctuations. The acoustical current meter attenuates these turbulent scales by more than an order of magnitude (Section 5.2.3). By comparison, the surface waves detected at the ice camp have wavelengths that are long relative to the averaging pathlengths; hence, they are not substantially attenuated. This is but one example of how the spatial filtering characteristic of the acoustical current meter may be used to detect phenomena that cannot be observed with the traditional approach; local flow disturbances are attenuated and the array focuses on events with scales that are large compared to its dimensions. We have shown that within the limits of experimental accuracy, the assumptions of thin ice, deep ocean and linear surface gravity wave theory are justified. Most importantly, we have obtained a measurement independent of ice tilt that confirms the presence of surface waves at the ice camp.

Chapter 8

Internal Waves

8.1 Introduction

In Chapter 7, we discussed the detection of surface waves using measurements of path-averaged horizontal velocity and ice tilt. Internal gravity waves are another source of flow disturbance with scales large compared to the dimensions of the acoustical current meter. Once again, we exploit the spatial filtering properties of the acoustical array, and the sensitivity of the tilt measurements, to observe internal waves with amplitudes smaller than the resolution of conventional current meters. The passage of an energetic wave packet is reported. Simultaneous observations at two depths are used to measure attenuation of internal wave kinetic energy as the ice is approached.

8.2 Low-Amplitude Wave Train

Because it attenuates turbulent velocity fluctuations, the acoustic current meter is particularly sensitive to the passage of internal waves which have wavelengths greater than 450 m (Section 4.5.2). Fig. 8.1a shows the signature of a very low amplitude internal wave train on horizontal current in the mixed layer at the 20.4 m depth. This coherent wave train was also detected by P. V. Czipott (1989, personal communication) using ice tilt measurements (Fig. 8.1b).

To relate tilt to horizontal velocity near the surface, we use the equation of

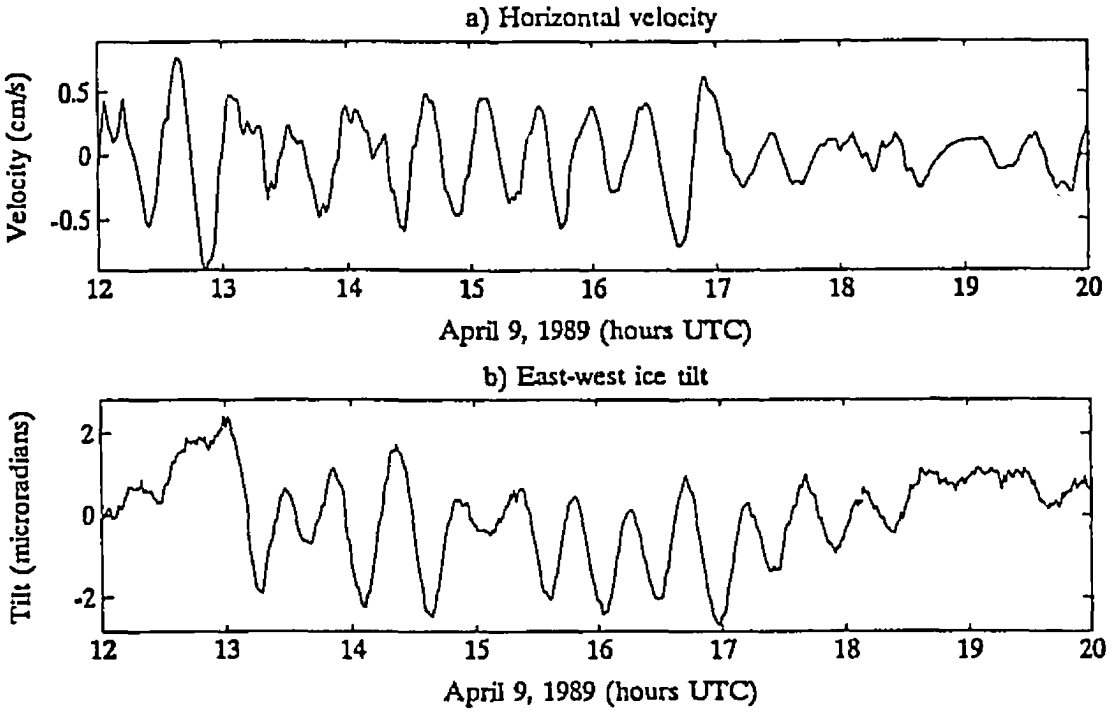

Figure 8.1: Low amplitude wave train. (a) Current speed relative to the ice at the 20.4 m depth. The time series is filtered with 0.0083 Hz lowpass and 1 cph highpass filters. (b) East-west ice tilt. The tiltmeter and the acoustic array were separated by some 337 m.

motion for non-viscous and incompressible fluid

$$\frac{\mathrm{dU}}{\mathrm{d}t} = \frac{\partial \mathrm{U}}{\partial t} + \mathrm{U} \cdot \nabla \mathrm{U} = \frac{-1}{\rho} \nabla P + \mathrm{g}, \tag{8.1}$$

where ∇ is the gradient operator, P the pressure, ρ the density, and g the acceleration due to gravity. The vertical component of (8.1) is simplified using the hydrostatic approximation,

$$\frac{\mathrm{d}U_3}{\mathrm{d}t} = \frac{-1}{\rho} \frac{\partial P}{\partial x_3} - g = 0, \tag{8.2}$$

and integrated with boundary condition $P = 0$ at the surface to obtain

$$P = \rho g(\eta - x_3), \tag{8.3}$$

where η is the surface elevation. The horizontal component of (8.1) can be written

$$\frac{\mathrm{d}U_h}{\mathrm{d}t} = \frac{-1}{\rho}\nabla_h P = -g\nabla_h \eta. \tag{8.4}$$

where U_h is the horizontal velocity near the surface, and ∇_h is the horizontal gradient operator. For internal waves at wavelengths much greater than the thickness of the ice, the ice is a flaccid membrane that responds to wave forcing as a free surface. Ice tilt τ is then proportional to horizontal acceleration of seawater near the surface,

$$\tan\tau = \nabla_h \eta = \frac{-1}{g}\frac{\mathrm{d}U_h}{\mathrm{d}t}. \tag{8.5}$$

Equation (8.5) shows that tilt of the ice reflects horizontal acceleration at the surface and that neither a steady flow, nor a spatially uniform flow forces tilt of the ice cover. For small surface displacement, and neglecting the Doppler shift caused by ice camp drift and the nonlinear terms, (8.5) simplifies to

$$\tau_o = k\eta_o = \frac{\omega}{g}u_o, \tag{8.6}$$

where τ_o, η_o, and u_o are the amplitudes of ice tilt, surface displacement, and horizontal velocity, respectively. The wave train of Fig. 8.1 has 28-min period and 3.5-mm/s root-mean-square (rms) horizontal velocity. Using (8.6), the expected tilt is 1.35 μrad rms as measured. The less than perfect coherence and the phase delay between tilt and acoustic current measurements is due in part to the 337 m separation between the tiltmeter and the acoustic array.

This low amplitude wave train was not detected by thermistor chains at the thermocline, or by other current meters at the ice camp. The detection of such an event using the path-averaging current meter and ice tiltmeters demonstrates the sensitivity of these two instruments to small internal waves. However, it must be pointed out that the current measurements have the advantage of seeing lower frequency flow fluctuations than the tiltmeters, and that ice tilt can be caused by

other things (and people), including thermal effects. Also, the current measurements do not suffer the uncertainty due to Doppler shift and the nonlinear terms in (8.5) as discussed in Section 8.3.2.

8.3 Energetic Wave Packet

As the camp drifted near the 2000-m isobath along the northern slope of the Yermak Plateau (Fig. 2.2), from 13 April to 20 April 1989, strong internal bores passed diurnally. Internal wave packets, with two to three oscillations at periods from 20 to 40 min, rode the crest of the bores. In this section, we report on the passage of one of these packets. Over the limited aperture ($\sim$ 1 km) of measurement arrays at the camp, the packet described herein passed at constant speed without change of form. It resembled a solitary wave coming from tidal flow over the Yermak Plateau [59].

8.3.1 Observations

The internal wave packet was observed passing the ice camp at 82.53° N, 8.58° E between 00 and 02 hours universal time coordinates (UTC) on 18 April 1989 (day 108) [13]. The wave forced a peak-to-peak ice tilt of 36 μrad in a north-south direction (Fig. 8.2a), in phase with the vertical component of seawater velocity in the pycnocline extending from about 100 to 200 m (Fig. 8.3) in water 1800 m deep. The vertical velocity in the packet had a maximum excursion of 15 cm/s at a depth near 125 m (Fig. 8.2b). Water temperature also revealed vertical displacement in a signal 90° out of phase with tilt and vertical velocity (Fig. 8.2c). Numerical integration of vertical velocity in the pycnocline shows that its maximum excursion was about 36 m during the passage of the packet (Fig. 8.2d). The internal undular bore resulted in a pycnocline displacement of about 15 m. Integrated velocity compares closely with pycnocline displacement determined from the temperature record of Fig. 8.2c. We used a mean gradient of -31 m/°C in the thermocline to

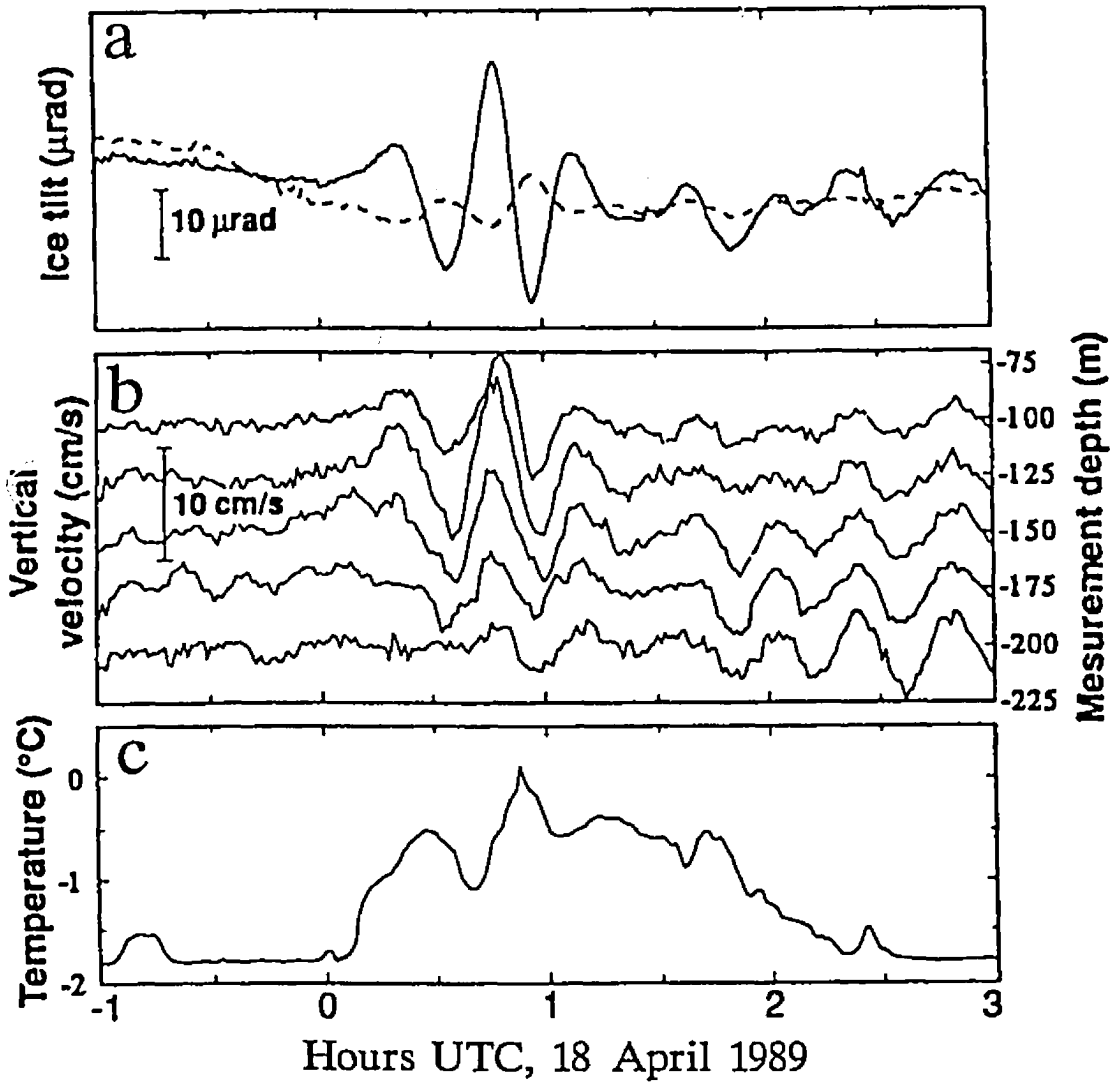

Figure 8.2: Signals during passage of a packet of internal waves between 00 and 02 hours UTC on 18 April 1989 (day 108) [13]. (a) Ice tilt measured in a north-south (solid line) and in an east-west direction (dashed line). The packet produced a maximum excursion of 36 μrad in north-south tilt and 7 μrad in east-west tilt. (b) Vertical velocity measured at depths of 100, 125, 150, 175, and 200 m, as marked on the right ordinate. The maximum excursion of vertical velocity in the packet was 15 cm/s at 125 m. (c) Water temperature at a depth of 99.5 m. Before the arrival of the packet, the thermometer was in a nearly isothermal mixed layer and was insensitive to vertical displacement of water. The mixed layer shoaled as the packet arrived. The thermometer, then in a thermocline, responded to displacements of the water column.

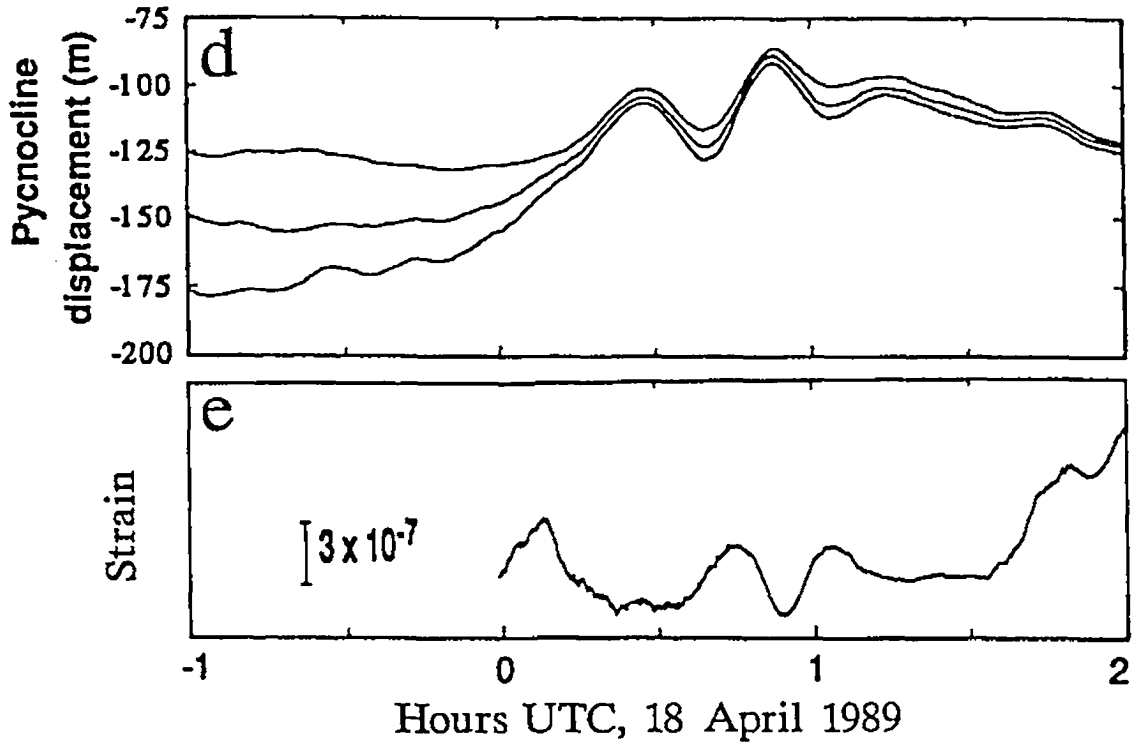

Figure 8.2: *(Continued)* (d) Pycnocline displacement determined by numerical integration over time of vertical velocity in the pycnocline, starting at 125-, 150-, and 175-m depths. It shows a peak excursion of 36 m during passage of the packet. (e) Longitudinal strain measured along a north-south axis on the surface of the ice. It shows an excursion of 3×10^{-7} coming from the packet.

convert temperature to a measure of displacement also indicating a peak excursion of 36 m. Strain of the ice, measured along a north-south direction, showed an excursion of 3×10^{-7} during the passage of the wave packet (Fig. 8.2e).

Tiltmeter and temperature arrays showed that the packet propagated in a direction within 20° of true north at a speed of 0.45 ms^{-1}; its wavelength was 632 m and its period was 24 [illegible]. The comparatively small east-west tilt shows that wave crests were orthogonal to the propagation vector. The wave form preserved its shape as it propagated through the instrument arrays.

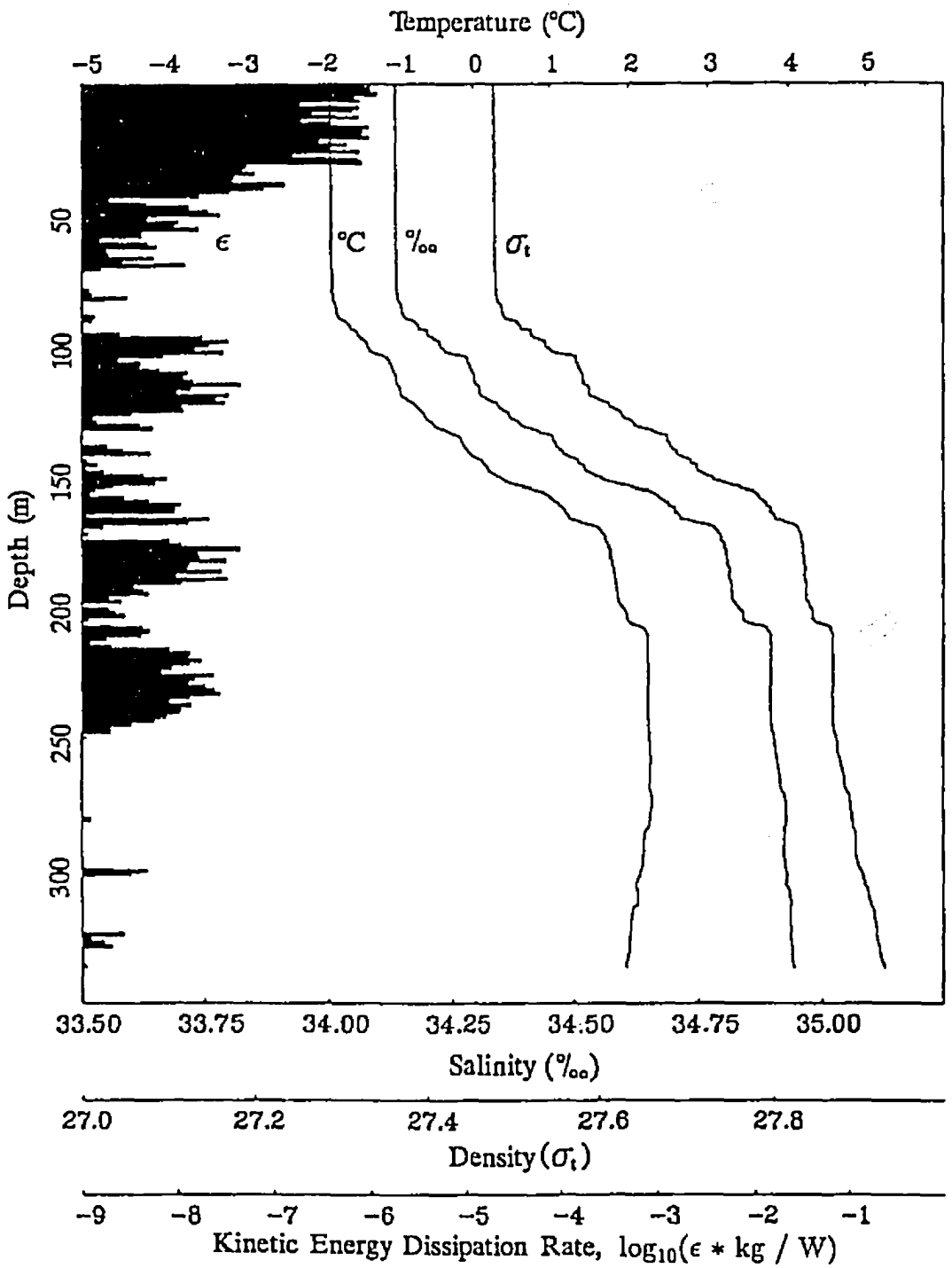

Figure 8.3: Vertical profile of temperature, salinity, density, and dissipation rate measured from the ice camp on 17 April 1989, 23:59 UTC, just before the passage of the internal wave packet [60].

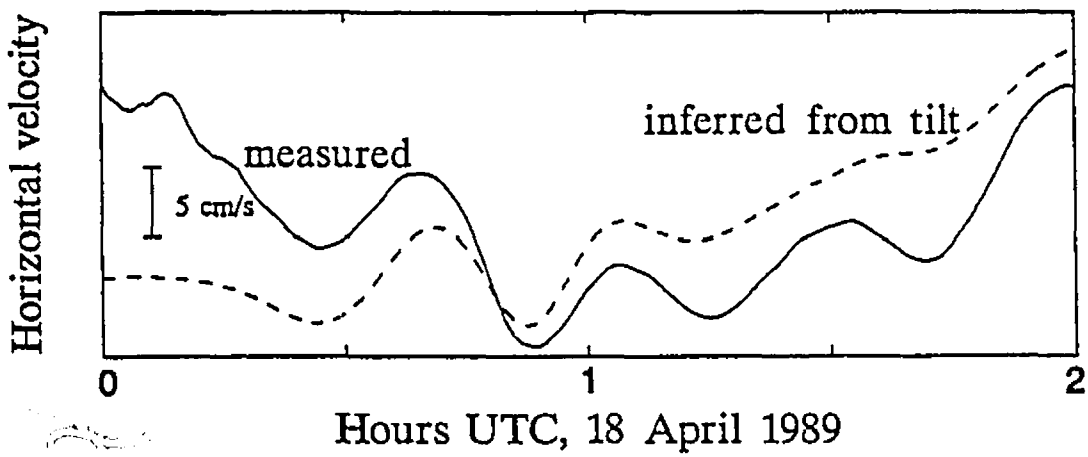

Figure 8.4: Horizontal seawater velocity near the surface during the internal wave packet. The 344° T horizontal current, measured at the 8-m depth by the path-averaging acoustic current meter (solid line), shows a maximum excursion of 12 cm/s during the packet. Horizontal current at the surface, inferred from ice tilt using (8.6) (dashed line), shows a maximum excursion of 8 cm/s during the packet. A 10-min delay was observed between ice tilt and horizontal velocity measurements; it results from the separation of the tiltmeter and acoustic array and has been removed in the figure.

8.3.2 Horizontal Velocity

As discussed in Section 8.2, the dimensions of the acoustic array are ideally suited for detecting horizontal velocity caused by the passage of internal waves. Scales smaller than 450 m are attenuated due to path-averaging, and a very "clean" record of the passage of the wave packet (λ = 632 m) is obtained. Compare for example the point and line-averaged horizontal velocity measurements of Fig. 4.5 during the passage of the internal wave packet.

In Fig. 8.4, we compare the measured horizontal seawater velocity near the surface with that inferred from ice tilt measurements during the internal wave packet. The 344° T horizontal current, which is roughly aligned with the propagation direction of the packet, measured at the 8-m depth by the path-averaging current meter is drawn as a solid line; it shows a maximum excursion of 12 cm/s during the packet. Horizontal current at the surface, inferred from ice tilt of Fig. 8.2a and (8.6) is drawn as a dashed line; it shows a maximum excursion of 8 cm/s during the

packet. The tilt measurements lagged the current measurements by approximately 10 min as a result of the separation between the tiltmeter and acoustic array.

Considering the good agreement between tilt and horizontal velocity for the low amplitude wave train of April 9 (Fig. 8.1), we were puzzled by the amplitude discrepancy observed during the April 18 event (Fig. 8.4). We expected the horizontal velocity measurements to be attenuated by the proximity of the ice (5.6 m on average), and the presence of deep ice keels (Fig. 2.4). Contrary to our expectations, the measured velocity excursion during the passage of the packet is 50% higher than that inferred from ice tilt.

At first, we thought that the amplitude discrepancy might result from the pressure differential δP supported by ice flexure at the ice-water interface. However, a first order approximation shows that δP is negligible compared to hydrostatic pressure from surface displacement. For a thin ice cover of thickness h and density ρ_i floating on water of density ρ, the expression [76]

$$\delta P = \left[\frac{E(hk)^4}{12(1-\nu^2)\rho g h} - \left(\frac{\omega^2}{gk}\right)\left(\frac{\rho_i}{\rho}\right)kh\right]\rho g\eta \tag{8.7}$$

gives the pressure differential for an oscillation with frequency ω, wavenumber k, and surface displacement η. Young's modulus of elasticity, E, and Poisson's ratio, ν, are 9.2×10^9 Pa and 0.365, respectively for sea ice [18]. For ice $h = 2.4$ m thick, the pressure differential δP caused by ice flexure during the passage of the wave packet is only 1.2% of the hydrostatic pressure $\rho g\eta$ that results from surface displacement. Therefore, differential pressure is negligible compared to hydrostatic pressure, and the ice cover is a flaccid membrane that effectively responds to wave forcing as a free surface.

Another attempt to reconcile ice tilt and horizontal current near the surface is based on Doppler-frequency shift caused by relative motion of the measuring platform (the ice camp) and the underlying seawater (Section 4.5.4). Consider an internal wave with radial frequency $\omega = 2\pi f$, wave vector k, and wavenumber

$k = 2\pi/\lambda$, propagating with phase speed $C = \omega/k$ in seawater. The apparent phase speed measured from the ice floe is

$$C_d = C + \mathrm{k} \cdot \overline{\mathrm{U}}/k = \omega_d/k, \tag{8.8}$$

where $\overline{\mathrm{U}}$ is the mean ice-relative velocity of seawater, and

$$\omega_d = \omega + \mathrm{k} \cdot \overline{\mathrm{U}} \tag{8.9}$$

is the Doppler-shifted frequency. Surface tilt caused by the passage of internal waves is proportional to ω, but does not depend on $\overline{\mathrm{U}}$. Using ω_d instead of ω to infer horizontal velocity from tilt results in a fractional error $\mathrm{k} \cdot \overline{\mathrm{U}}/kC$. The phase speed of the energetic wave packet measured from the drifting ice platform is $C_d = 45$ cm/s, and the ice-relative seawater velocity parallel to the wave vector is $\mathrm{k} \cdot \overline{\mathrm{U}}/k = 7.5$ cm/s. Therefore, neglecting the Doppler shift accounts for roughly half the discrepancy between the measured and inferred horizontal velocity of Fig. 8.4.

In the first-order analysis presented here, we have also neglected the nonlinear terms of (8.5). Roughly, the magnitude of these terms, $k|u_h|^2$, is approximately 27% that of the linear term, $\omega|u_h|$. For this reason, we attribute the remaining discrepancy between the measured and inferred horizontal velocity to the nonlinear terms.

8.3.3 Vorticity

M. D. Levine (1989, personal communication) suggested that the passage of internal waves under the ice camp may have a measurable relative vorticity signature due to conservation of potential vorticity as the mixed layer depth contracts and expands. Provided that there is no input of vorticity, such as might come from frictional effects within the ice, we have

$$\frac{\mathrm{d}}{\mathrm{d}t}\left(\frac{\zeta + f}{D}\right) = 0, \tag{8.10}$$

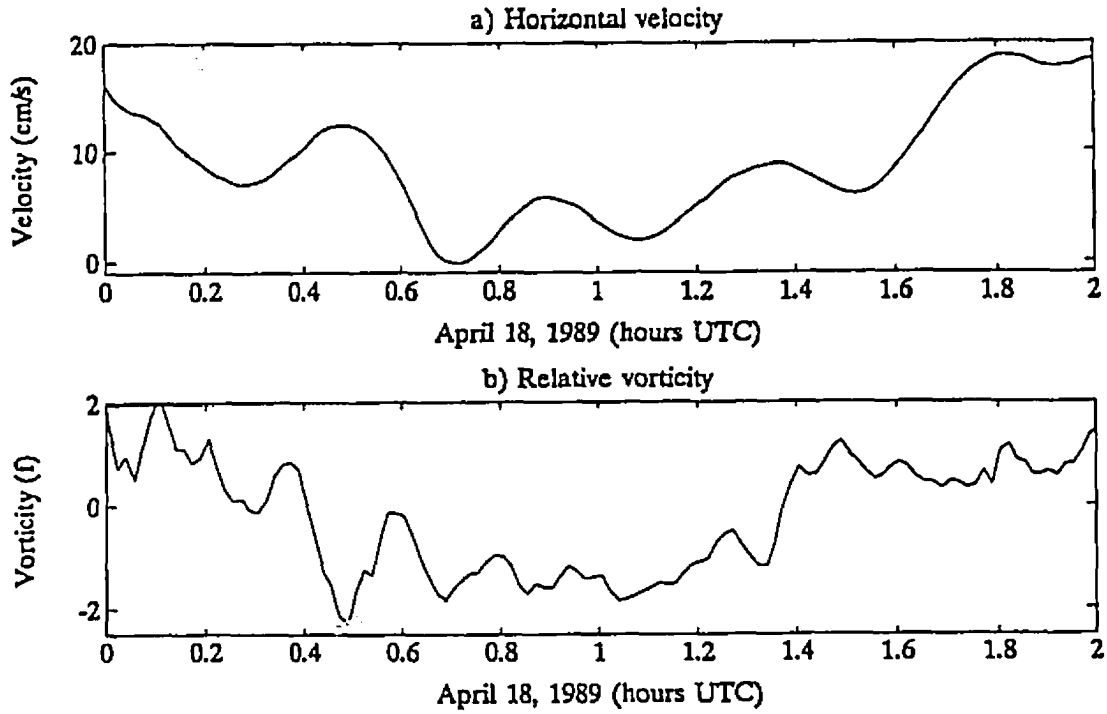

Figure 8.5: Vorticity at the 8.4-m depth forced by the passage of an energetic internal wave packet under the ice camp. (a) Horizontal velocity, 344° T. (b) Relative vorticity.

where ζ is the relative vorticity, f the planetary vorticity, and D the depth of the mixed layer.

We test this hypothesis during the passage of the energetic wave packet that propagated under the ice camp between 00 and 02 UTC on April 18, 1989. The waves in the packet had phase velocity 45 cm/s, wavelength 632 m and period 24 min (Section 8.3.1). The size of the acoustic array (approximately one third of the wavelength), was ideally suited to detect vorticity at these scales. The undisturbed depth of the mixed layer before the passage of the packet was 100 m (Fig. 8.3), and the packet caused a maximum excursion of 36 m in the pycnocline (Fig. 8.2d). Based on (8.10), and assuming negligible relative vorticity before the passage of the wave, we expect a vorticity excursion of order 0.3 f.

In Fig. 8.5 we plot the horizontal velocity parallel to the propagation direction and the relative vorticity at 8.4 m depth during the passage of the wave packet. The

measured vorticity is much greater than what can be accounted for by conservation of potential vorticity. In addition, the frequency of the vorticity signal is double that of the internal waves, *i.e.* the interaction of the waves and the ice is nonlinear. We conclude that interaction between the boundary layer and the ice is a more important source of relative vorticity than changes in the depth of the mixed layer.

R. W. Stewart (1993, personal communication) suggested that lift due to flow around ice keels may be a significant source of local ice strain. Consider for example circulation (3.17) $\Gamma \approx 5$ m^{2}s^{-1}, and mean ice-relative velocity $\overline{U} \approx 0.1$ ms^{-1}, typical of conditions measured during the experiment. The lift force per unit length normal to the flow direction on an ice keel is of order [33]

$$L = \rho \Gamma \overline{U} \approx 500 \text{ ntm}^{-1}, \tag{8.11}$$

where ρ is seawater density. Fig. 2.4 indicates that the acoustic array encloses a pressure ridge keel with characteristic depth of order 5 m. Therefore, the lift force exerted on that keel is of order 2500 nt. Compare the magnitude of this force to the drag due to turbulent momentum flux on the region spanned by the acoustic array, $\tau_o A_T \approx 1500$ nt, where $\tau_o \approx 0.08$ ntm^{-2} is a typical value for the oceanic stress exerted on the ice (Section 6.5.4), and $A_T = 18327$ m^2 is the area enclosed by the array. We conclude that the lift force may indeed be significant in causing localized ice strain (Fig. 8.2e). However, due to the random distribution and shape of ice keels, we expect the lift force to be negligible when averaged over a large enough area, as opposed to drag which is proportional to the size of the area under consideration.

8.4 Comparison Between Two Depths

Because of its sensitivity, the acoustic current meter is well suited to the study of boundary layer effects on internal wave velocity structure, and of coupling between internal waves and turbulence in terms of dissipation of internal wave energy.

Neglecting the effects of ice friction and planetary rotation, the expected horizontal velocity of internal waves in the mixed layer,

$$u_h(z) = u_h(0)\cosh(k_h z), \tag{8.12}$$

is a function of depth z and horizontal wavenumber k_h [66]. For example, given a 600 m wavelength, we expect 1.64% attenuation of horizontal velocity at 10 m depth compared to 20 m depth. Any additional attenuation may indicate dissipation of internal wave energy due to frictional effects.

In Fig. 8.6, we compare internal wave velocities measured by the acoustic current meter at depths of 10.4 and 20.4 m. For periods greater than 20 min, there is zero lag and good coherence between the measurements at the two depths as shown on Figs 8.7a and 8.7b respectively. This is consistent with the notion that velocity fluctuations with periods greater than 20 min are principally caused by internal waves which are coherent throughout the boundary layer, while fluctuations with periods shorter than 20 min result mostly from turbulent eddies which have limited vertical extent. The horizontal velocity energy spectra (Fig. 8.8) indicate possible attenuation of internal wave energy and intensification of turbulent kinetic energy as the ice is approached.

In Fig. 8.6d we compare relative vorticity measured at two depths. There is very little coherence between the two time-series even at periods associated with internal waves. As for velocity spectra (Fig. 8.8), the spectra of vorticity (Fig. 8.9) indicate low frequency attenuation and high frequency intensification as the ice is approached. We found little coherence between horizontal velocity and relative vorticity measurements; therefore, we discount the possibility that the similar behavior of the spectra results from common measurement errors.

8.5 Summary and Conclusions

In this chapter, we have discussed the detection and study of internal waves using the path-averaged horizontal velocity signal and the relative vorticity measure-

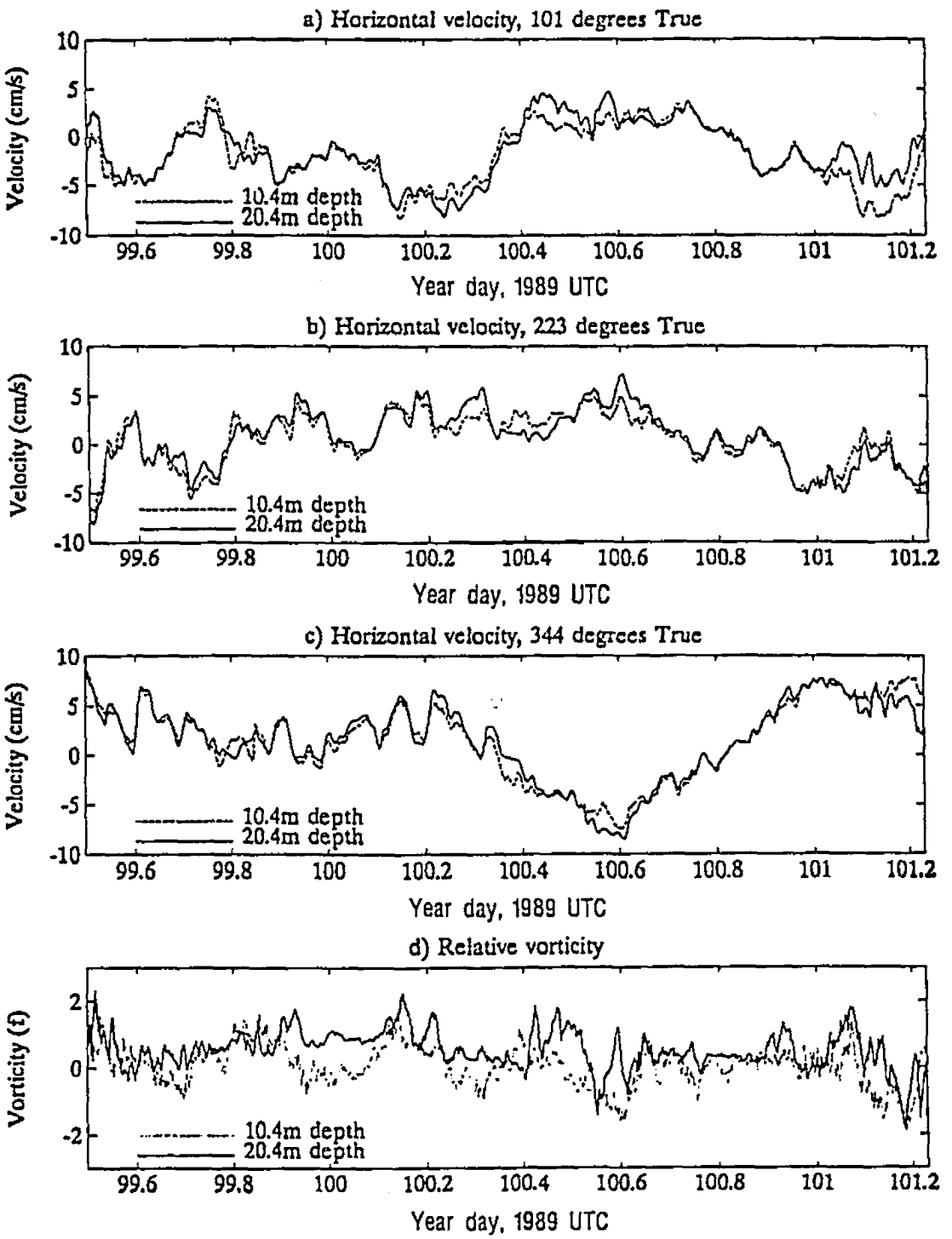

Figure 8.6: Velocity and vorticity measurements at the 10.4 and 20.4-m depths. (a) Horizontal velocity, 101° T. (b) Horizontal velocity, 223° T. (c) Horizontal velocity, 344° T. (d) Relative vorticity.

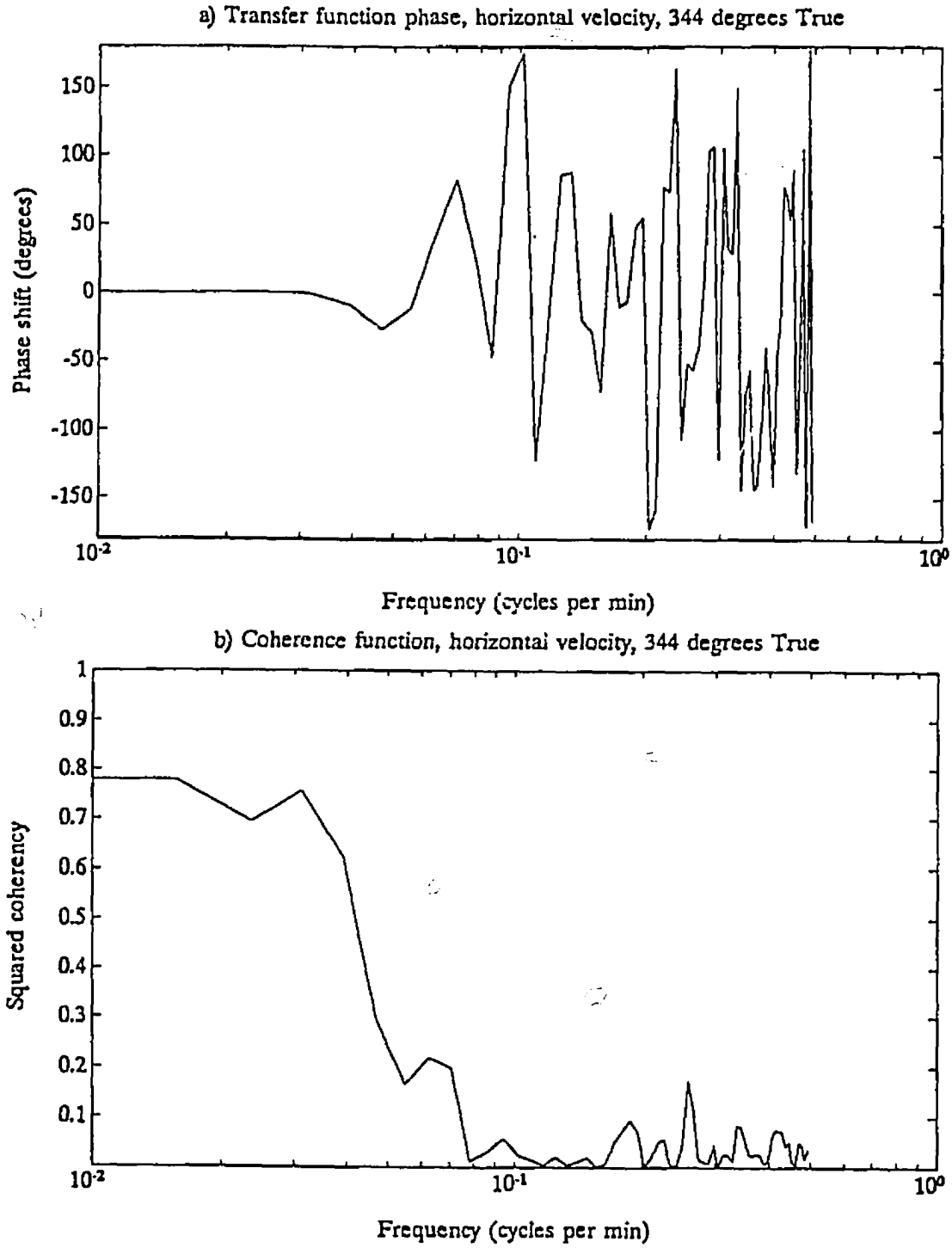

Figure 8.7: Cross-spectrum of the 10.4- and 20.4-m depth horizontal velocity for the 344° T acoustic path. (a) Phase. (b) Coherence.

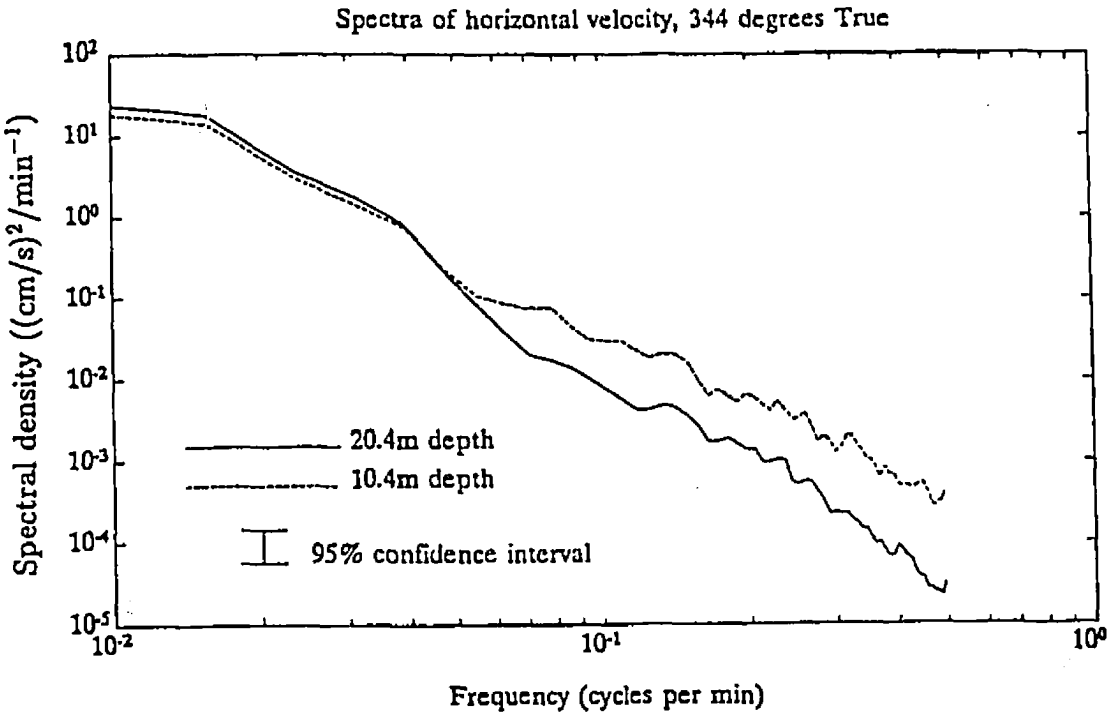

Figure 8.8: Spectra of 344° T horizontal velocity at the 10.4- and 20.4-m depth.

ments made with the acoustic array in the mixed layer beneath ice. The dimensions and spatial filtering properties of the acoustic current meter make it ideally suited for detecting high-frequency, low-amplitude internal waves which are otherwise masked by turbulent velocity fluctuations and local inhomogeneities of the flow. Conventional current meter measurements of water velocity near the surface often cannot detect the small velocities forced by internal waves, because flow over the rough bottom of the ice leads to turbulence. The low-amplitude wave train event of April 9 was not detected by acoustic Doppler nor by mechanical current meters deployed at the ice camp, or by temperature-sensor arrays. The only other instruments deployed at the ice camp with comparable sensitivity to the passage of low-amplitude internal waves were the tiltmeters; the ice acts as a spatial filter to suppress small-scale turbulence and enables tiltmeters to measure vertical surface currents from internal waves. But the tiltmeters have serious limitations—*i.e.* inability to see low frequency fluctuations and bias caused by ice drift. For the

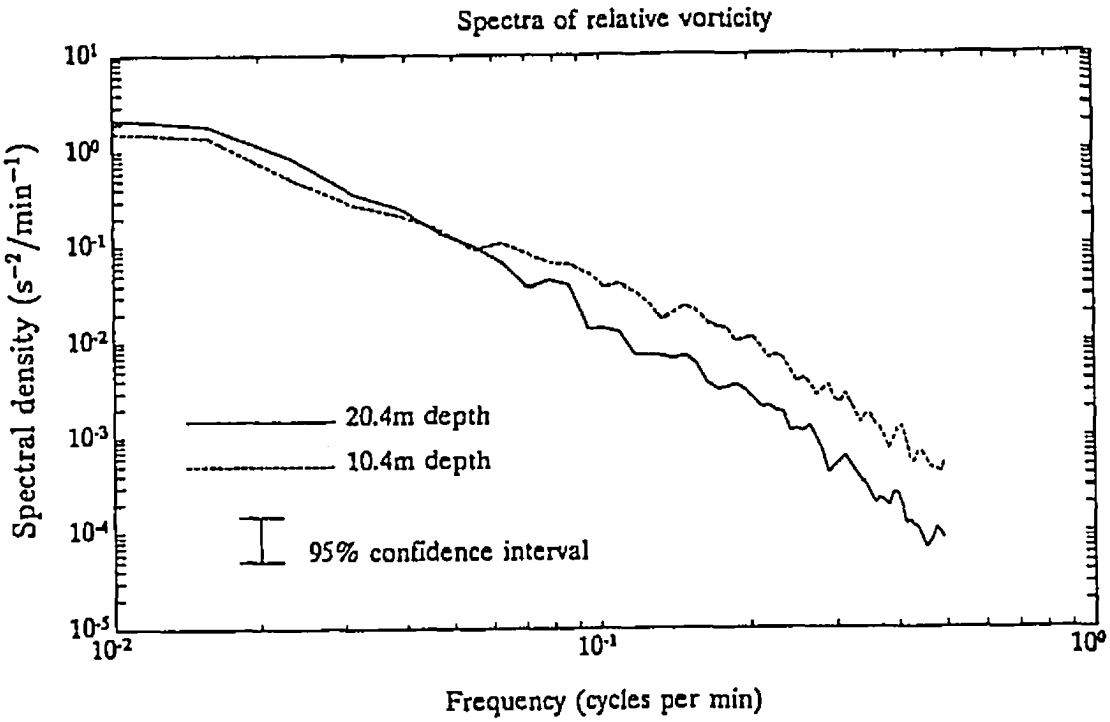

Figure 8.9: Spectra of relative vorticity at the 10.4 and 20.4-m depths for the time-series of Fig. 8.6d

April 9 event, we have shown that ice tilt and horizontal velocity measurements near the surface are in good agreement with a first-order analysis that neglects Doppler shift and nonlinear terms in (8.5).

We have also discussed the passage of a wave packet on April 18, that is more than two orders of magnitude more energetic than the event of April 9. For the April 18 event, we find that the first order analysis is not adequate for relating horizontal velocity near the surface with ice tilt. The horizontal velocity at the surface determined by numerical integration over time of surface tilt, is approximately in phase with horizontal velocity measured directly by the acoustic array at a depth of 8 m, but is two-thirds of its amplitude (Fig. 8.4). We attribute the discrepancy to the Doppler shift introduced by a steady ice camp drift of 7.5 cm/s and to nonlinear terms in (8.5), which we have neglected in the first-order analysis presented here. Each of these factors accounts for an error of roughly 15%

in the tilt measurement. This analysis points out some of the limitations of tilt measurements for detecting internal waves. First, ice drift relative to seawater can introduce an error which is proportional to the ratio of ice-relative seawater velocity and the internal-wave phase speed. Second, for energetic internal waves, nonlinear effects may attenuate surface displacements and ice tilt measurements will underestimate the kinetic energy of the waves.

Chapter 9

Summary and Concluding Remarks

We have measured horizontal currents in the ice-water boundary layer using two path-averaging acoustical methods: scintillation drift and reciprocal transmission. The two methods provide orthogonal components of velocity for each set of acoustic paths. A limitation of our signal recording scheme restricts the accuracy of the scintillation measurements; the length of the guard sequences used was limited by real-time decoding requirements, and either the direct or the reflected path arrivals were recorded for each transmission because of limited recording bandwidth. However, the present measurements demonstrate that the use of the full signal and appropriate analysis would allow excellent scintillation flow measurements.

Reciprocal transmission measurements are contaminated by relative motion of the acoustic elements during each reciprocal transmission for frequencies in the neighborhood of the mooring's mechanical resonance. At frequencies away from this resonance, the noise floor results from interference of the ice-reflected acoustic path with line-of-sight propagation which, as pointed out above, could have been overcome with full signal recording or the use of longer guard sequences for decoding. Nevertheless, the rms noise level for the actual horizontal velocity measurements using reciprocal transmission is less than 0.1 mm/s averaged over 1 min.

The unprecedented sensitivity of the acoustical current meter allows the detec-

tion of events that cannot be detected by other current meters deployed at the ice camp. For example, we were able to detect horizontal velocity caused by flexural gravity waves originating in the open ocean which is several hundred kilometers away from the ice camp.

Comparison of path-averaged velocity with point measurements shows marked differences which we attribute to local anomalies of the flow field caused by the rough ice topography. The acoustic system provides integral measurements which average over several turbulent eddies; therefore, the measured horizontal velocity is particularly sensitive to the passage of low amplitude internal waves under the ice camp. A comparison of horizontal velocity at two depths in the boundary layer shows good coherence at internal wave frequencies and some attenuation as the ice is approached.

Relative vorticity averaged over the span of the acoustic array was measured to an accuracy of 0.01 f for a filtered sampling rate of 1 min. Vorticity at internal wave length scales is dominated by horizontal shear caused by interaction with ice topography and not by planetary vorticity as we initially expected.

In theory, scintillation drift around the triangular array can be used to obtain horizontal divergence. We were unable to obtain meaningful measurements of horizontal divergence during the experiment because of insufficient signal to noise ratio. As previously explained, this was due to a processing and recording design limitation rather than any inherent limitation of the scintillation approach.

The sensitivity of the instrument also allows detection of kinetic energy at frequencies associated with the advection and evolution of turbulent velocity fine structure. We have shown that line-averaged velocity measurements over paths of several hundred meters can be used to probe the statistical behaviour of turbulent velocity fine structure. Measuring baselines several times longer than the scales of interest have been considered and analytic expressions for the transfer function between true and line-averaged one-dimensional spectra have been derived both for isotropic and for axially symmetric turbulence. The measurements are most

sensitive to velocity fluctuations when the mean velocity vector is transverse to the measuring baseline; for this situation, the error incurred by assuming isotropy instead of axial symmetry is unlikely to exceed 16%. A dimensional argument has been used to show that for homogeneous turbulence and long measuring baselines, the spectral attenuation due to line-averaging is inversely proportional to the non-dimensional wavenumber $k_1\ell$. At sufficiently high wavenumbers, line-averaged measurements provide a representative areal average of the kinetic energy spectrum in the plane formed by the mean velocity vector and the measuring baseline.

Criteria have been obtained for applying Taylor's frozen field hypothesis to long measuring baselines, and correction formulas have been derived for the effects of variable advection velocity and mean horizontal shear. Neither of these two phenomena are likely to cause errors exceeding 10%, as long as the mean velocity vector is within 30° of being perpendicular to the measuring baseline. Some practical limitations of this measuring technique have been discussed and it is concluded that the theory is only applicable to scales of the order of the first Fresnel zone or larger. To probe smaller scales, the problem must be treated as a volume average, which has not been done in this paper; alternatively the acoustic frequency can be increased or the pathlength decreased.

The theory appears to fit observations of high-frequency horizontal velocity fluctuations obtained in the boundary layer beneath ice during the arctic experiment. The predicted spectral attenuation has been compared with the actual attenuation between point and line-averaged measurements. The predicted dependence of this attenuation on the angle between the mean flow and the measuring baseline has been compared to the ratio of the velocity spectra for each of the three acoustic paths of the triangular array.

We conclude that reciprocal acoustical transmission applied over hundreds of meters is a promising remote sensing technique for obtaining line-averaged statistical information about the velocity fine structure of a turbulent fluid. By simultaneously transmitting acoustic pulses in opposite directions between two points, one

can separate the effects of velocity fine structure on acoustic propagation from the effects of sound speed structure; in conjunction with an analysis of forward scatter acoustical scintillations, reciprocal travel time measurements provide information about both the velocity and the sound speed structure of the intervening fluid. For measurements inside a Kolmogorov inertial subrange, it is possible to obtain an areal average of energy dissipation rate which is insensitive to local inhomogeneities of the flow.

9.1 Recommendations for Future Studies

In concluding, a number of suggestions for future studies and applications of the measurement techniques discussed in this thesis come to mind. The accuracy of the present set of measurements was constrained by the instrumentation and not by any inherent physical limitations such as ambient noise, non-reciprocity of acoustic paths due to shear, high-frequency vibrations of the moorings, scattering and diffraction effects, or the advection and evolution of turbulent fine structure during reciprocal transmission. It would be desirable to obtain measurements that make the full spectrum available for analysis.

Improving the sensitivity of the measurements might require some refinements in the theory in order to account for effects that were negligible in the analysis of the arctic data set. For example, one might consider volume averaging caused by diffraction effects for scales smaller than the first Fresnel zone, or the nonreciprocity at small scales due to turbulent shear. Corrections for the advection and evolution of turbulent fine structure during a reciprocal transmission, and for nonreciprocity of the sonic paths due to mean shear may be derived.

The measurement of energy dissipation rate is of practical importance to many oceanographic studies. Amplitude and reciprocal travel-time scintillation analysis could be carried out in a turbulent tidal channel where temperature and velocity fine structure are equally important in producing forward scatter. It would be interesting to compare the relative importance of the two scattering processes through

several tidal cycles and to interpret the observations in terms of the oceanography of the channel.

Measuring energy dissipation rate in the open ocean close to the surface using reciprocal travel time scintillation analysis would present special difficulties due to the presence of bubbles and their strong scattering cross section. Nevertheless, provided reciprocal transmission is established, multipaths are resolved, and the data is corrected for mooring motion, sensitive path-averaged velocity measurements should be possible.

Reciprocal travel time measurements could also replace moorings that measure turbulence due to the breaking of internal waves hundreds of meters below the surface. The mixing events are intermittent (log-normal distributed) both in space and time, and long averaging periods are required. Path-averaged measurements sample a larger volume of water than point measurements during any given time period, and thus provide better spectral estimates of turbulence. The acoustic measurements also have the advantage of being a remote sensing technique which does not disturb the flow that is measured.

There is some interest in the measurement of potential vorticity at internal wave length scales, and the measurement of relative vorticity and horizontal divergence have been attempted using triangular arrays of current meter. The sampling errors inherent in these discrete measurements could be eliminated by replacing the current meters with pairs of transducers that measure scintillation drift and reciprocal travel time, hence resolving normal and along-path integrated velocities. These integrated velocities can then be used to estimate horizontal divergence and relative vorticity.

Bibliography

[1] *Coordinated Eastern Arctic Experiment Operations Plan.* Office of Naval Research, Washington, 1988. Compiled and Edited by the Science Discipline Coordinators, Prospective Principal Investigators, and CEAREX Project Staff.

[2] Marcelo Alonso and Edward J. Finn. *Fundamental University Physics.* Volume I Mechanics of *Addison-Wesley Series in Physics*, Addison-Wesley Publishing Company, Don Mills, Ontario, 1967.

[3] G. K. Batchelor. The theory of axisymmetric turbulence. *Proceedings of the Royal Society of London*, A 186:480–502, 1946.

[4] G. K. Batchelor. *The Theory of Homogeneous Turbulence. Cambridge Monographs on Mechanics and Applied Mathematics*, Cambridge University Press, New York, 1956.

[5] Julius S. Bendat and Allan G. Piersol. *Random Data: Analysis and Measurement Procedures. A Wiley-Interscience Publication*, John Wiley& Sons, Toronto, second edition, 1986.

[6] Leonid Brekhovskikh and Yury Lysanov. *Fundamentals of Ocean Acoustics. Springer Series in Electrophysics 8*, Springer-Verlag, New York, 1982.

[7] Robert A. Brown. Meteorology. In Jr. Walker O. Smith, editor, *Polar Oceanography, Part A: Physical Sciences*, chapter 1, pages 1–46, Academic Press, Inc., Toronto, 1990.

[8] A. Bruce Carlson. *Communication Systems: an Introduction to Signals and Noise in Electrical Communications. McGraw Hill Series in Electrical Engineering. Communications and Signal Processing*, McGraw-Hill Book Company, Toronto, third edition, 1986.

[9] S. F. Clifford. Temporal-frequency spectra for a spherical wave propagating through atmospheric turbulence. *Journal of the Optical Society of America*, 61(10):1285–1292, October 1971.

[10] Steven F. Clifford and David M. Farmer. Ocean flow measurements using acoustic scintillation. *Journal of the Acoustical Society of America*, 74(6):1826–1832, December 1983.

[11] Roger Colony. *Measurement of Bottom Topography of the Ice at the CEAREX Oceanography Camp.* Technical Report, Applied Physics Laboratory, 1013 NE 40th Street, Seattle, Washington 98105-6698, 1989.

[12] G. B. Crawford, R. J. Lataitis, and S. F. Clifford. Remote sensing of ocean flows by spatial filtering of acoustic scintillations: theory. *Journal of the Acoustical Society of America*, 88(1):442–454, July 1990.

[13] Peter V. Czipott, Murray D. Levine, Clayton A. Paulson, Dimitris Menemenlis, David M. Farmer, and Robin G. Williams. Ice flexure forced by internal wave packets in the Arctic Ocean. *Science*, 254(5033):832–835, 8 November 1991.

[14] Peter V. Czipott and Walter N. Podney. *Measurement of Fluctuations in Tilt of Arctic Ice at the CEAREX Oceanography Camp: Experiment Review, Data Catalog, and Preliminary Results.* Final Technical Report PD-LJ-89-369R, Physical Dynamics, Inc., 7855 Fay Avenue, Suite 300, La Jolla, CA 92037, March 1989.

[15] Richard K. Dewey and James N. Moum. Enhancement of fronts by vertical mixing. *Journal of Geophysical Research*, 95(C6):9433–9445, June 15, 1990.

[16] Robert C. Dixon. *Spread Spectrum Systems. A Wiley-Interscience Publication*, John Wiley & Sons, Toronto, second edition, 1984.

[17] Ira Dyer. The song of sea ice and other Arctic Ocean melodies. In Ira Dyer and C. Chryssostomidis, editors, *Arctic Policy and Technology Proceedings*, pages 11–37, Hemisphere Publishing Corp., 1984.

[18] M. Ewing, A. P. Crary, and A. M. Thorne, Jr. *Physics*, 5:165, 1934.

[19] D. M. Farmer and G. B. Crawford. Remote sensing of ocean flows by spatial filtering of acoustic scintillations: observations. *Journal of the Acoustical Society of America*, 90(3):1582–1591, September 1991.

[20] David M. Farmer and Steven F. Clifford. Space-time acoustic scintillation analysis: a new technique for probing ocean flows. *IEEE Journal of Oceanic Engineering*, OE-11(1):42–50, January 1986.

[21] David M. Farmer, Steven F. Clifford, and Jane A. Verrall. Scintillation structure of a turbulent tidal flow. *Journal of Geophysical Research*, 92(C5):5369–5382, May 15, 1987.

[22] M. J. Fisher and P. O. A. L. Davies. Correlation measurements in a non-frozen pattern of turbulence. *Journal of Fluid Mechanics*, 18(1):97–116, January 1964.

[23] Stanley M. Flatté. Wave propagation through random media: contributions from ocean acoustics. *Proceedings of the IEEE*, 71(11):1267–1294, November 1983.

[24] A. E. Gargett, T. R. Osborn, and P. W. Nasmyth. Local isotropy and the decay of turbulence in a stratified fluid. *Journal of Fluid Mechanics*, 144:231–280, 1984.

[25] Christopher Garrett and Walter Munk. Space-time scales of internal waves. *Geophysical Fluid Dynamics*, 2:225–264, 1972.

[26] Christopher Garrett and Walter Munk. Space-time scales of internal waves: a progress report. *Journal of Geophysical Research*, 80(3):291–297, January 20, 1975.

[27] H. L. Grant, R. W. Stewart, and A. Moilliet. Turbulence spectra from a tidal channel. *Journal of Fluid Mechanics*, 12:241–263, 1962.

[28] P. S. Guest and K. L. Davidson. *CEAREX/"O" and "A" Camp Meteorology Atlas.* Data Report NPS-63-89-007, Naval Postgraduate School, Monterey, CA 93943-5000, September 1989.

[29] J. R. Herring. Approach of axisymmetric turbulence to isotropy. *The Physics of Fluids*, 17(5):859–872, May 1974.

[30] J. O. Hinze. *Turbulence. McGraw-Hill Series in Mechanical Engineering*, McGraw-Hill Book Company, Toronto, second edition, 1975.

[31] J. C. Kaimal, J. C. Wyngaard, and D. A. Haugen. Deriving power spectra from a three-component sonic anemometer. *Journal of Applied Meteorology*, 7:827–837, October 1968.

[32] D. S. Ko, H. A. DeFerrari, and P. Malanotte-Rizzoli. Acoustic tomography in the Florida strait: temperature, current, and vorticity measurements. *Journal of Geophysical Research*, 94(C5):6197–6211, May 15, 1989.

[33] Pijush K. Kundu. *Fluid Mechanics.* Academic Press, Inc., Toronto, 1990.

[34] M. P. Langleben. Water drag coefficient of first-year ice. *Journal of Geophysical Research*, 87(C1):573–578, January 20, 1982.

[35] Paul H. LeBlond and Lawrence A. Mysak. *Waves in the Ocean. Elsevier Oceanography Series 20*, Elsevier Scientific Publishing Company, New York, 1978.

[36] Robert W. Lee and Jeffrey C. Harp. Weak scattering in random media, with applications to remote probing. *Proceedings of the IEEE*, 57(4):375–406, April 1969.

[37] Murray D. Levine. Internal waves under the arctic pack ice during the arctic internal wave experiment: the coherence structure. *Journal of Geophysical Research*, 95(C5):7347–7357, May 15, 1990.

[38] Murray D. Levine, Clayton A. Paulson, and James H. Morison. Observations of internal gravity waves under the arctic pack ice. *Journal of Geophysical Research*, 92(C1):779–782, January 15, 1987.

[39] C. C. Lin. On Taylor's hypothesis and the acceleration terms in the Navier-Stokes equations. *Quarterly of Applied Mathematics*, X(4):295–306, January 1953.

[40] Michael Longuet-Higgins. On triangular tomography. *Dynamics of Atmospheres and Oceans*, 7:33–46, 1982.

[41] J. L. Lumley. Interpretation of time spectra measured in high-intensity shear flows. *The Physics of Fluids*, 8(6):1056–1062, June 1965.

[42] John L. Lumley and Hans A. Panofsky. *The Structure of Atmospheric Turbulence.* Volume XII of *Interscience Monographs and Texts in Physics and Astronomy*, John Wiley & Sons, New York, 1964.

[43] Miles G. McPhee. A rigid, cable-lowered instrument frame for measuring turbulence and internal waves in the Arctic. *IEEE Journal of Oceanic Engineering*, 14(2):203–207, April 1989.

[44] Miles G. McPhee. Small-scale processes. In Jr. Walker O. Smith, editor, *Polar Oceanography, Part A: Physical Sciences*, chapter 6, pages 287–334, Academic Press, Inc., Toronto, 1990.

[45] Miles G. McPhee. Turbulent heat flux in the upper ocean under sea ice. *Journal of Geophysical Research*, 97(C4):5365–5379, April 15, 1992.

[46] Miles G. McPhee. The upper ocean. In Norbert Untersteiner, editor, *The Geophysics of Sea Ice*, chapter 4, pages 339–394, Plenum Press, New York, 1986.

[47] H. Medwin. Sound phase and amplitude fluctuations due to temperature microstructure in the upper ocean. *Journal of the Acoustical Society of America*, 56(4):1105–1110, October 1974.

[48] Robert H. Mellen. The thermal-noise limit in the detection of underwater acoustic signals. *Journal of the Acoustical Society of America*, 24(5):478–480, September 1952.

[49] Patrice Mestayer. Local isotropy and anisotropy in a high-Reynolds-number turbulent boundary layer. *Journal of Fluid Mechanics*, 125:475–503, 1982.

[50] John F. B. Mitchell. The "greenhouse" effect and climate change. *Reviews of Geophysics*, 27(1):115–139, February 1989.

[51] James H. Morison. Physical oceanography instrumentation for the polar regions: a review. *IEEE Journal of Oceanic Engineering*, 14(2):173–185, April 1989.

[52] Peter Müller, Greg Holloway, Frank Henyey, and Neil Pomphrey. Nonlinear interactions among internal gravity waves. *Reviews of Geophysics*, 24(3):493–536, August 1986.

[53] Peter Müller, Ren-Chieh, and Robin Williams. Estimates of potential vorticity at small scales in the ocean. *Journal of Physical Oceanography*, 18:401–416, March 1988.

[54] W. Munk, P. Worcester, and F. Zachariasen. Scattering of sound by internal wave currents: the relation to vertical momentum flux. *Journal of Physical Oceanography*, 11:442–456, April 1981.

[55] Walter Munk and Carl Wunsch. Ocean acoustic tomography: a scheme for large scale monitoring. *Deep-Sea Research*, 26A:123–161, 1979.

[56] Walter Munk and Carl Wunsch. Up-down resolution in ocean acoustic tomography. *Deep-Sea Research*, 29(12A):1415–1436, 1982.

[57] Fridtjof Nansen. *Farthest North*. Volume 1 and 2, Archibald Constable and Company, 2 Whitehall Gardens, Westminster, 1897.

[58] N. S. Oakey and J. A. Elliott. Dissipation within the surface mixed layer. *Journal of Physical Oceanography*, 12:171–185, February 1982.

[59] L. A. Ostrovsky and Yu. A. Stepanyants. Do internal solitons exist in the ocean? *Reviews of Geophysics*, 27(3):293–310, August 1989.

[60] Laurie Padman and Thomas A. Dillon. *Microstructure Profiles During CEAREX*. Data Report 150, College of Oceanography, Oregon State University, Corvallis, Oregon 97331, April 1990.

[61] Laurie Padman and Thomas M. Dillon. Turbulent mixing near the Yermak Plateau during the coordinated eastern Arctic experiment. *Journal of Geophysical Research*, 96(C3):4769–4782, March 15 1991.

[62] Laurie Padman, Albert J. Plueddemann, Robin D. Muench, and Robert Pinkel. Diurnal tides near the Yermak Plateau. *Journal of Geophysical Research*, 97(C8):12639–12652, August 15 1992.

[63] Hans A. Panofsky and John A. Dutton. *Atmospheric Turbulence. A Wiley-Interscience Publication*, John Wiley & Sons, Toronto, 1984.

[64] Stephen Pond and George L. Pickard. *Introductory Dynamical Oceanography.* Pergamon Press, Toronto, second edition, 1983.

[65] William H. Press, Saul A. Teukolsky, William T. Vetterling, and Brian P. Flannery. *Numerical Recipes in FORTRAN: The Art of Scientific Computing.* Cambridge University Press, New York, second edition, 1992.

[66] Jo Roberts. *Internal Gravity Waves.* Volume 2 of *Marine Science*, Marcel Dekker, New York, 1975.

[67] T. Rossby. An oceanic vorticity meter. *Journal of Marine Research*, 33(2):213–222, 1975.

[68] U. Schumann and J. R. Herring. Axisymmetric homogeneous turbulence: a comparison of direct spectral simulations with the direct-interaction approximation. *Journal of Fluid Mechanics*, 76:755–782, 1976.

[69] Kunio Shirasawa. Water stress and ocean current measurements under first-year sea ice in the Canadian Arctic. *Journal of Geophysical Research*, 91(C12):14305–14316, December 15, 1986.

[70] Michael W. Stacey, Stephen Pond, and Paul H. LeBlond. A wind-forced ekman spiral as a good statistical fit to low-frequency currents in a coastal strait. *Science*, 233:470–472, 25 July 1986.

[71] R. W. Stewart. *The Atmospheric Boundary Layer.* Third IMO Lecture 523, World Meteorological Organisation, 1979.

[72] R. W. Stewart. Turbulence and waves in a stratified atmosphere. *Radio Science*, 4(12):1269–1278, December 1969.

[73] V. I. Tatarskii. *The Effects of the Turbulent Atmosphere on Wave Propagation.* Israel Program for Scientific Translations, Jerusalem, 1971. Translated from Russian.

[74] G. I. Taylor. The spectrum of turbulence. *Proceedings of the Royal Society of London*, A 164(919):476–490, 18 February 1938.

[75] Norbert Untersteiner, editor. *The Geophysics of Sea Ice.* Plenum Press, New York, 1986.

[76] Peter Wadhams. The seasonal ice zone. In Norbert Untersteiner, editor, *The Geophysics of Sea Ice*, chapter 14, pages 825–991, Plenum Press, New York, 1986.

[77] Ting-i Wang, G. R. Ochs, and R. S. Lawrence. Wind measurements by the temporal cross-correlation of the optical scintillations. *Applied Optics*, 20(23):4073–4081, December 1981.

[78] Robert C. Weast, editor. *CRC Handbook of Chemistry and Physics.* CRC Press, Inc., Boca Raton, Florida, 62 edition, 1981-1982.

[79] A. W. Wernik, C. H. Liu, and K. C. Yeh. Modeling of spaced-receiver scintillation measurements. *Radio Science*, 18(5):743–764, September-October 1983.

[80] Hemantha Wijesekera, Laurie Padman, Tom Dillon, Murray Levine, and Clayton Paulson. The application of internal-wave dissipation models to a region of strong mixing. *Journal of Physical Oceanography*, 23:269–286, February 1993.

[81] R. G. Williams, N. R. Davis, and S. C. Moore. The coordinated eastern Arctic experiment: SPRI sea-ice studies. *Polar Record*, 26(158):203–210, 1990.

[82] Kraig B. Winters and Daniel Rouseff. A filtered backprojection method for the tomographic reconstruction of fluid vorticity. *Inverse Problems*, 6:L33–L38, 1990.

[83] Peter F. Worcester. Reciprocal acoustic transmission in a midocean environment. *Journal of the Acoustical Society of America*, 62(4):895–905, October 1977.

[84] Peter F. Worcester, Robert C. Spindel, and Bruce M. Howe. Reciprocal acoustic transmissions: instrumentation for mesoscale monitoring of ocean currents. *IEEE Journal of Oceanic Engineering*, OE-10(2):123–136, April 1985.

[85] Hidekatsu Yamazaki, Rolf G. Lueck, and Thomas Osborn. A comparison of turbulence data from a submarine and a vertical profiler. *Journal of Physical Oceanography*, 20:1778–1786, November 1990.

Appendix A

Correlation Peak Interpolation

In this appendix, two methods for interpolating the location t_0 and amplitude A of correlation peaks are presented. In the first method, a theoretical expression for the shape of the peak is derived and a nonlinear curve fitting algorithm is applied. The second method is less accurate but also easier to implement; a linear least squares algorithm is used to fit the data to a quadratic.

For the first method, equations 3.6, 3.7 and 3.8 are used to obtain an expression for the shape of the peak. Since convolution in the time domain becomes multiplication in the frequency domain, equation 3.6 can be written

$$\mathcal{R}_{xy}(f) = \mathcal{H}(f)\mathcal{R}_x(f), \tag{A.1}$$

where $\mathcal{R}(f)$ and $\mathcal{H}(f)$ are the Fourier transforms of $R(\tau)$ and $h(\tau)$ respectively. The transform of equation 3.8 is

$$\mathcal{R}_x(f) = \frac{A\sin^2(\pi f \tau_p)}{\tau_p(\pi f)^2}. \tag{A.2}$$

Equations 3.7, A.1 and A.2 yield the cross-correlation as a function of frequency:

$$\mathcal{R}_{xy}(f) = \begin{cases} \mathcal{R}_x(f) & \text{if } -\tau_p^{-1} \le f \le \tau_p^{-1} \\ 0 & \text{otherwise} \end{cases}. \tag{A.3}$$

The definition of the inverse Fourier transform,

$$\mathcal{R}_{xy}(\tau) = \int_{-\infty}^{\infty} \mathcal{R}_{xy}(f)\exp(i2\pi f\tau)\,df, \tag{A.4}$$

n	a_n
0	0.9028233336
1	−2.0000000000
2	1.8599120891
3	−0.9877523383
4	0.3428553005
5	−0.0841722149
6	0.0154094590
7	−0.0021857624
8	0.0002473421
9	−0.0000228505

Table A.1: Coefficients of the polynomial which describes the shape of the correlation peak.

standard integral tables, and trigonometric identities are used to solve for $\mathcal{R}_{xy}(\tau)$ explicitly:

$$\mathcal{R}_{xy}(\tau) = \frac{A}{\pi} \sum_{n=0}^{\infty} \frac{(-1)^n (2\pi)^{2n+1}}{(2n+1)^2 (2n)!} \left[\left(\frac{\tau}{\tau_p} + 1 \right)^{2n+2} + \left(\frac{\tau}{\tau_p} - 1 \right)^{2n+2} - 2 \left(\frac{\tau}{\tau_p} \right)^{2n+2} \right]. \tag{A.5}$$

The binomial theorem is applied to convert this expression into a polynomial in even powers of τ/τ_p,

$$\mathcal{R}_{xy}(\tau) = A \sum_{n=0}^{\infty} a_n \left(\frac{\tau}{\tau_p} \right)^{2n}, \tag{A.6}$$

with coefficients

$$a_n = \frac{2}{\pi} \sum_{m=n}^{\infty} \frac{(-1)^m (2\pi)^{2m+1} (2m+2)}{(2m+1)(2n)!(2m+2-2n)!}. \tag{A.7}$$

Table A.1 gives numerical values for the first ten coefficients. The series in equation A.6 converges rapidly for $\tau/\tau_p \leq 1$, because successive terms have alternating signs; the maximum error, when n terms are used, is bounded by $A|a_n|(\tau/\tau_p)^{2n}$.

Given data points Y_i corresponding to times t_i, the maximum likelihood estimate of t_o and A is obtained by minimizing the merit function

$$\chi^2 = \sum_{i=1}^{N} [Y_i - \mathcal{R}_{xy}(t_i, t_o, A)]^2 , \tag{A.8}$$

where the correlation delay $\tau = t_i - t_o$. This χ^2 function is minimized using the *Broyden-Fletcher-Goldfarb-Shanno* algorithm to implement the *variable metric* method [65].

A second method for interpolating peak location and amplitude is to assume that the peak has a quadratic shape near the maximum and to fit the five recorded data points using linear least squares. For convenience, equation 3.10 is expressed in terms of a nondimensional time variable u,

$$\mathcal{R}_{xy}(u) = a + bu + cu^2, \tag{A.9}$$

where $u = (t - t_3)/\tau_s$, t_3 corresponds to the central data point, $\tau_s = \tau_p/4$ is the sampling period, and $u_i = i - 3$. The amplitude of the quadratic peak,

$$A_q = \frac{c - b^2}{4a}, \tag{A.10}$$

and its location

$$t_o = t_3 - \frac{b}{2a}\tau_s, \tag{A.11}$$

can be expressed in terms of the coefficients of equation A.9. The merit function that must be minimized is

$$\chi^2 = \sum_{i=1}^{5} \left[Y_i - (a + bu_i + cu_i^2)\right]^2 . \tag{A.12}$$

The solution is obtained by use of the *normal equations* [65]:

$$\begin{bmatrix} a \\ b \\ c \end{bmatrix} = (\mathbf{A}^T\mathbf{A})^{-1}\mathbf{A}^T \begin{bmatrix} Y_1 \\ Y_2 \\ Y_3 \\ Y_4 \\ Y_5 \end{bmatrix}, \qquad \mathbf{A} = \begin{bmatrix} 1 & -2 & 4 \\ 1 & -1 & 1 \\ 1 & 0 & 0 \\ 1 & 1 & 1 \\ 1 & 2 & 4 \end{bmatrix}, \tag{A.13}$$

where

$$(\mathbf{A}^T\mathbf{A})^{-1}\mathbf{A}^T = \begin{bmatrix} -0.0857 & 0.3429 & 0.4857 & 0.3429 & -0.0857 \\ -0.2000 & -0.1000 & 0.0000 & 0.1000 & 0.2000 \\ 0.1429 & -0.0714 & -0.1429 & -0.0714 & 0.1429 \end{bmatrix}. \tag{A.14}$$

Appendix B

Shear Effects on Sound Rays

In the presence of shear, the acoustic propagation paths of sound rays traveling in opposite directions between two points, do not overlap. This lack of reciprocity may result in an erroneous estimate of path-averaged velocity. In order to estimate the magnitude of this error, we consider changes in acoustic travel time and separation between sound rays traveling in opposite directions.

Consider vertical shear o such that the horizontal fluid velocity along an arbitrary x-axis is

$$u(z) = u_o + \sigma z. \tag{B.1}$$

Without loss of generality, we let $u_o = 0$, and position two acoustic elements at $x = 0$ and $x = \ell$, on the horizontal plane $z = 0$ (Fig. B). Acoustic rays, propagating from $x = 0$ to $x = \ell$, bend downward if $\sigma > 0$ and upward if $\sigma < 0$.

In a time-independent medium, the acoustic frequency, $\omega = 2\pi f$, remains constant along each ray:

$$\omega = k_o(c_o + u_o \cos\chi_o) = k[c(z) + u(z)\cos\chi] \tag{B.2}$$

where $k = 2\pi/\lambda$ is the wavenumber, $c(z)$ is the vertical sound speed profile, χ is the grazing angle that the ray forms with a horizontal plane, and $u(z)\cos\chi$ is the component of flow velocity parallel to the acoustic propagation path. By continuity, the horizontal component of the wavenumber vector must also remain

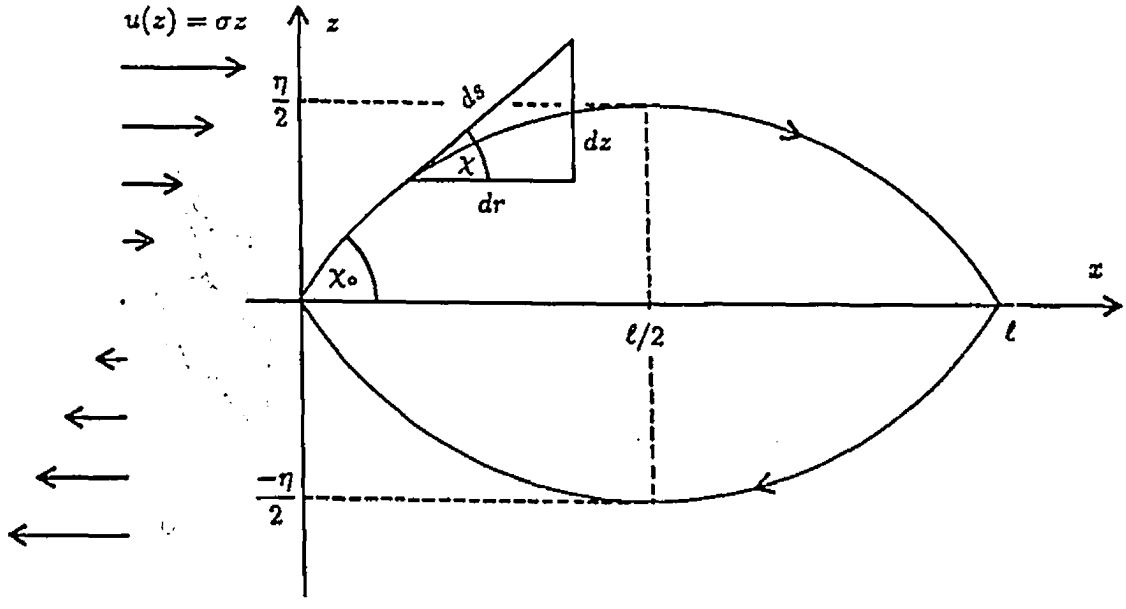

Figure B.1: Ray bending in shear flow. In the presence of shear, sound rays propagating in opposite directions between two points do not follow overlapping trajectories. This may introduce an error in current measurements that rely on reciprocal travel time difference. This figure defines the variables used to obtain approximate expressions for change in acoustic travel time and maximum separation between opposite sound rays.

constant:

$$k_0 \cos\chi_0 = k \cos\chi. \tag{B.3}$$

Eliminating k between (B.2) and (B.3), we obtain

$$\frac{\cos\chi}{\cos\chi_0} = \frac{c(z) + u(z)\cos\chi}{c_0 + u_0 \cos\chi_0}, \tag{B.4}$$

which is Snell's law of refraction, modified by the presence of shear.

If the sound speed profile is constant, $c(z) = c_0$, then the shear will affect the total travel time Σt, but not the travel time difference Δt of two acoustic signals propagating in opposite directions. The change in total travel time due to the presence of shear, and the maximum separation between opposite sound rays, are determined using (B.1) and (B.4).

In order for sound rays to intersect the x-axis at $x = \ell$, they must leave $x = 0$ with a grazing angle of χ_0. The turning depth, $\chi = 0$, occurs at the point of

maximum separation from the x-axis, $z = \eta/2$ and $x = \ell/2$. The horizontal distance to the turning depth is

$$\frac{\ell}{2} = \int_0^{\ell/2} dr = \int_0^{\eta/2} \frac{dz}{\tan\chi}. \tag{B.5}$$

We assume $\sigma\ell \ll 2c$, to solve for range,

$$\ell = \frac{2c_o}{\sigma} \ln(\sec\chi_o + \tan\chi_o) \approx \frac{2c_o\chi_o}{\sigma}, \tag{B.6}$$

and initial grazing angle,

$$\chi_o \approx \frac{\sigma\ell}{2c_o}. \tag{B.7}$$

Referring to Fig. B, we note that an element of length ds along the propagation path is equal to $dz/\sin\chi$. Therefore, the travel time to $z = \eta/2$ is

$$\frac{\Sigma t}{4} = \int_0^{\eta/2} \frac{dz}{[c_o + u(z)\cos\chi]\sin\chi}. \tag{B.8}$$

We solve for total travel time,

$$\Sigma t = \frac{2}{\sigma}\tan\chi_o + \frac{\ell}{c_o}\cos\chi_o \approx \frac{2\ell}{c_o} - \frac{\sigma^2\ell^3}{24c_o^3}. \tag{B.9}$$

and note that vertical shear σ decreases the total travel time by $\approx \sigma^2\ell^3/24c_o^3$. Finally, we obtain an expression for the maximum separation between sound rays propagating in opposite directions:

$$\eta = \frac{2c_o}{\sigma}(\sec\chi_o - 1) \approx \frac{\sigma\ell^2}{4c_o}. \tag{B.10}$$

Appendix C

Path-Integral Approximation for a Long Baseline

The left-hand-side of (5.29) can be written

$$A(k_1, k_3) = \int_{-\infty}^{\infty} \frac{\sin^2(\alpha k_2 + \beta)}{(\alpha k_2 + \beta)^2} \varphi_\theta(\mathrm{k})\, dk_2, \tag{C.1}$$

where

$$\alpha = \frac{\ell}{2} \sin\theta \tag{C.2}$$

and

$$\beta = \frac{\ell k_1}{2} \cos\theta. \tag{C.3}$$

We note that $\sin^2 x/x^2$ has a main lobe of width 2π, centered at $x = 0$, and enclosing 90% of the total area under the curve. For (C.1), the main lobe is centered at $k_2 = -k_1 \cot\theta$ and has width $4\pi/\ell \sin\theta$. If the width of this lobe is small compared with the wavenumber range of interest, that is $k_1 \ell \sin\theta \gg 4\pi$, then

$$\varphi_\theta(\mathrm{k}) \approx \varphi_\theta(\mathrm{k})|_{k_2 = -k_1 \cot\theta} = \varphi_\theta(k_1, -k_1 \cot\theta, k_3), \tag{C.4}$$

and

$$A(k_1,k_3) \approx \varphi_\theta(k_1,-k_1\cot\theta,k_3)\int_{-\infty}^{\infty}\frac{\sin^2(\alpha k_2+\beta)}{(\alpha k_2+\beta)^2}\,dk_2$$

$$= \frac{2\pi}{\ell\sin\theta}\varphi_\theta(k_1,-k_1\cot\theta,k_3). \qquad \text{(C.5)}$$